공학박사학위논문

Practical Microkinetic Modeling of Heterogeneous Catalytic Reactions through Parameter Estimation

파라미터 추정을 통한 불균일계 촉매 반응의 마이크로키네틱 모델링

2021 년 8 월

서울대학교 대학원

화학생물공학부

박 종 민

Practical Microkinetic Modeling of Heterogeneous Catalytic Reactions through Parameter Estimation

파라미터 추정을 통한 불균일계 촉매 반응의 마이크로키네틱 모델링

지도 교수 이 원 보

이 논문을 공학박사 학위논문으로 제출함
2021년 8월

서울대학교 대학원
화학생물공학부
박 종 민

박종민의 공학박사 학위논문을 인준함
2021년 8월

위 원 장 ______________________

부위원장 ______________________

위　　원 ______________________

위　　원 ______________________

위　　원 ______________________

Abstract

Practical Microkinetic Modeling of Heterogeneous Catalytic Reactions through Parameter Estimation

Jongmin Park
School of Chemical & Biological Engineering
Graduate School of Seoul National University

In recent years, as environmental issues continue to emerge, interest in carbon utilization where carbon dioxide is the primary species to be reduced is growing. Accordingly, many researchers and industries in various fields have tried to reduce carbon emissions into the atmosphere. In particular, chemical engineers have developed carbon utilizing reaction processes which produce a variety of useful chemicals by consuming the greenhouse gases. Although the commercial processes related to these reactions have already been developed, controversy over their reaction mechanisms is still ongoing. Along with advances in computational performance, researches on reaction mechanism exploration are becoming more active in a new phase. Computational chemistry, which requires high computational costs, is a great help for reaction mechanism analysis. Moreover, microkinetic study is a study that can analyze mechanisms from a kinetic perspective, creating synergies along with improvements in computational chemistry. While conventional kinetic models in chemical engineering have been mainly used in terms of process design, microkinetic models, in addition to these advantages, allow fundamental analysis. For these reasons, mechanism analysis through microkinetics is actively underway even for common reactions. In this thesis, practical microkinetic modeling strategies that could improve several previous drawbacks were proposed. For reactions related to methanol and dimethyl ether (DME) synthesis, density functional theory (DFT) calculations and microkinetic modeling using the DFT results were conducted, and the reaction mechanism analysis and the several case studies were suggested. By using parameter estimation techniques, pre-exponential factors were fitted to experimental data minimizing the differences between the predicted and the experimental values. This practical modeling approach to the microkinetics improved computational efficiency and reliability of the model.

In the first part, a lumped kinetic model for the direct synthesis of dimethyl ether from syngas over Cu/ZnO/Al_2O_3/ferrierite (CZA/FER) catalyst was presented to highlight the difference from a microkinetic model. Kinetic parameters were estimated by fitting experimental data for the hybrid catalyst, and these were compared with the reported values of conventional catalysts, which were the respective CZA and FER catalysts. High activation energies for the hybrid catalyst showed that the methanol synthesis step may have more control over the rate than the methanol dehydration step. Using the developed kinetic model, a temperature between 200 and 220 °C was determined for thermal energy efficiency, and a further analysis provided the optimal range of the total pressure and space velocity.

A practical strategy to develop a microkinetic model for methanol synthesis from syngas over a Cu-based catalyst is described in the second part. The comprehensive model consists of forward and backward reactions of 28 possible elementary-step reactions for CO and CO_2 hydrogenation and the water–gas shift reaction. A combination of ab-initio DFT and semi-empirical unity bond index-quadratic exponential (UBI-QEP) methods was used to determine the heat of adsorption and activation energies. DFT calculations confirmed that formate (HCOO**) adsorbs in a bidentate fashion and provided the enthalpies and adsorption energies of gas and surface intermediates for subsequent UBI-QEP calculations. The pre-exponential factors were estimated from the order-of-magnitude of the transition state theory as the initial values and by fitting the experimental data, thus reducing the computational load by not calculating the vibrational frequencies and partition functions for translational, rotational, and vibrational motions. For the reactor model, partial equilibrium ratios were used to reduce the stiffness of the microkinetic model. The most plausible reaction pathways were suggested by considering relatively fast step-reactions, while the surface reaction of H_3CO^* and H^* was found to be the rate-determining step by the degree of rate control. The developed model was also used to evaluate the effects of the temperature, pressure, and H_2 fraction in the feed on the methanol synthesis rate to elucidate the suitable operating conditions.

In the third part, the reaction pathways of DME synthesis by methanol dehydration over a H-zeolite catalyst were analyzed through both computational chemistry and microkinetic modeling methods. The reaction mechanisms consisted of nine elementary-step reactions for both associative and dissociative pathways. Based on the second-order Møller–Plesset perturbation theory (MP2), to determine the effects of dispersion forces that were important in this reaction system, the structures of all related reaction species were optimized, and the transition states of the associative and dissociative pathways were elucidated. Also, the energies and activation barriers of the optimized structures and transition states were calculated. Then, a microkinetic model was developed using the energies and activation barriers obtained from the MP2 calculations. Meanwhile, the pre-exponential factors of the kinetic parameters were not calculated theoretically but estimated by fitting the experimental data, which enhanced the reliability of the microkinetic model. By comparing the relative elementary-step reaction rates calculated using the developed model, the dissociative pathway was suggested as a dominant pathway of DME synthesis, while the DME formation reaction of the dissociative pathway (CH_3OH-CH_3-Z $\rightarrow$ CH_3OCH_3-H-Z) was found to be the rate-determining step. The developed model was also used to evaluate the effects of temperature on the site fractions over the catalyst.

Finally, machine learning-based surrogate models of the microkinetic model for the water-gas shift reaction were developed. The surrogate model can play a role in a bridge between the microkinetics and the higher-scale reaction engineering modules such as computational fluid dynamics or process simulations. The ExtraTrees algorithm and the artificial neural network (ANN) were used for regressing the datasets acquired from the developed microkinetic model. Among interpolative machine learning techniques, an ANN is well known for its high performance in regression, and the feature importance can be calculated with the ExtraTrees algorithm. As a result, the ANN showed the great performance with an average error of 0.01 %. ExtraTrees could measure the feature importance, so that the important elementary reactions and surface intermediates to the overall reaction of the water-gas shift reaction were figured out.

Keywords: Microkinetic modeling; Computational chemistry; Parameter estimation; Reaction mechanism; C1 chemistry; Machine learning

Student Number: 2015-22831

Contents

Abstract i

List of Figures x

List of Tables xiv

Chapter 1 Introduction 16

1.1 Research Motivation 16

1.2 Outline of the Thesis 18

1.3 Associated Publications 18

Chapter 2 Background Theory 19

2.1 Microkinetics 19

2.2 Kinetic Parameter 22

2.2.1 Computational Chemistry 24

2.2.2 Transition State Theory 25

2.2.3 UBI-QEP 28

Chapter 3 Lumped kinetic modeling for direct synthesis of DME from syngas 30

3.1 Background 30

3.2 Methods 34

3.2.1 Experimentals 34

3.2.2 Kinetic Model 37

3.3 Application Results and Discussion 42

Chapter 4 Microkietic modeling of methanol synthesis from syngas

53

4.1 Background 53

4.2 Reaction Mechanism 59

4.3 Methods 63

4.3.1 Activation Energy 63

4.3.2 Microkinetic Model 67

4.4 Application Results and Discussion 74

4.4.1 DFT Calculations 74

4.4.2 Microkinetic Model 78

4.4.3 Rate-Determining Step 88

4.4.4 Effects of Operating Conditions 89

Chapter 5 Microkinetic modeling of DME synthesis from methanol over H-zeolite catalyst 92

5.1 Background 92

5.2 Reaction mechanism 97

5.3 Methods 102

5.3.1 Computational Chemistry 102

5.3.2 Microkinetic Model 106

5.4 Application results and discussion 109

5.4.1 MP2 Calculations 109

5.4.2 Microkinetic Model 126

Chapter 6 Machine Learning-based Surrogate Model of Microkinetics for the Water-Gas Shift Reaction 136

6.1 Background 136

6.2 Reaction Mechanism 138

6.3 Methods 140

6.3.1 Microkinetic Model 140

6.3.2 Surrogate Model 143

6.4 Application Results and Discussion 148

6.4.1 Microkinetic Model 148

6.4.2 Surrogate Model 151

Chapter 7 Concluding Remarks 157

7.1 Summary of Contributions 157

7.2 Future Work 160

Appendix 162

Supporting Information 162

Bibliography 165

Abstract in Korean (국문초록) 177

List of Figures

Figure 1 Multiscale modeling in a microkinetic model. 21

Figure 2 Comparisons of CO_2 conversions between experimental data and calculation results (experimental conditions for each case are referred to Table 2)... 43

Figure 3 Parity plot of the experimental data versus the calculation results of the CO (blue rectangle) and CO_2 (orange rectangle) conversions, and MeOH (gray circle) and DME (yellow circle) selectivities. The dotted lines represent the ±20% errors. 44

Figure 4 Semi-log plot for a comparison of the estimated kinetic parameters for the hybrid catalyst with those reported in the literature. The units of the frequency factors for each parameter are given in Tables 4 and 5. The red arrows indicate the estimated parameters in the present work. 48

Figure 5 Effects of operating conditions on the conversions (left column) and selectivities (right column); the first, second, and third rows show the effects of temperature, total pressure, and GHSV, respectively. The fixed conditions were: P_{total} = 50 bar, GHSV = 2,000 L/(kg_{cat}·h), and $CO/CO_2/H_2/N_2$ = 21/9/66/4% for varying temperature; T = 200 °C, GHSV = 2,000 L/(kg_{cat}·h), and $CO/CO_2/H_2/N_2$ = 21/9/66/4% for varying total pressure; and T = 200 °C, P_{total} = 50 bar, and $CO/CO_2/H_2/N_2$ = 21/9/66/4% for varying GHSV. 51

Figure 6 Scheme of the stepwise multiscale modeling procedure. 58

Figure 7 Cu (111) slab model. 65

Figure 8 Most stable state of HCOO** calculated by the DFT method (bidentate form). 77

Figure 9 Partial equilibrium ratios for the surface reactions at three different temperatures 79

Figure 10 Experimental and calculated CH_3OH/H_2O synthesis rates (● CH_3OH, □ H_2O). 81

Figure 11 Most plausible reaction pathways for (a) CO and (b) CO_2 hydrogenation. 85

Figure 12 Plots of surface coverage as a function of the total pressure at H_2 fractions of (a) 0.9 and (b) 0.5 87

Figure 13 Effects of (a) pressure (stoichiometric ratio of H_2 = 2) and (b) stoichiometric ratio of H_2 (pressure = 50 bar) on the methanol synthesis rate at temperatures of 460, 480, and 500. 91

Figure 14 Dissociative (left) and associative (right) pathways for methanol dehydration. 99

Figure 15 Framwork of the 4T cluster model used in this work. 104

Figure 16 Optimized structures of the (a) 4T cluster of H-zeolite (H-Z) and (b) the cluster with methanol adsorbed (CH_3OH-H-Z), which are included in both the associative and dissociative pathways. 112

Figure 17 Reaction procedure of R2 and R3: (a) initial state (CH_3OH-H-Z), (b) transition state, and (c) final state (H_2O (g) and CH_3-Z)........116

Figure 18 Methanol adsorption to CH_3-Z..118

Figure 19 Reaction procedure of R5 and R6: (a) initial state (CH_3OH-CH_3-Z), (b) transition state, and (c) final state (CH_3OCH_3 and H-Z)....... 120

Figure 20 Optimized structure of H-Z when two methanol molecules were adsorbed. 122

Figure 21 Evolutionary change of the structure: (a) initial state (CH_3OH-CH_3OH-H-Z), (b) transition state, and (c) final state (CH_3OCH_3-H_2O-H-Z)... 123

Figure 22 Energy levels of two reaction pathways for DME synthesis: Black line represents common steps in the associative and dissociative pathways, while blue and red lines represent distinctive steps for the associative and dissociative pathways, respectively. ... 125

Figure 23 Experimental and calculated CH_3OCH_3/CH_3OH molar flow rates at the reactor outlet (□ CH_3OCH_3, ● CH_3OH)........................ 127

Figure 24 Relative forward reaction rates for the dissociative pathway (R1–R6) on a log scale at $T = 450$, 475, and 500 K........................ 132

Figure 25 Effects of temperature on the site fractions on a log scale for the intermediates whose values were (a) > 10^{-6} and (b) < 10^{-6}.............. 135

Figure 26 The implemented ANN structure... 147

Figure 27 Parity plot of the experimental and the calculated turnover rates. 149

Figure 28 Changes of errors as increasing the number of decision trees in ensemble for the test (upper; blue line) and the training sets (lower; red line). 152

Figure 29 Relative importances of (a) the elementary reaction rates and (b) the surface intermetiates to the TOR. 154

Figure 30 Performance of regression by the ANN; (a) Mean squared error between the predictions by the ANN and the microkinetic model; (b) The error distribution. 156

List of Tables

Table 1 Equations for calculation of the activation energies by the UBI-QEP[†] 29

Table 2 Experimental conditions 36

Table 3 Reaction rate equations and estimated kinetic parameters 38

Table 4 Estimated kinetic parameters for MeOH synthesis from syngas of the present and previous studies (numbers in the parentheses represent 95% confidence intervals) 45

Table 5 Estimated kinetic parameters for DME synthesis from MeOH of the present and previous studies (numbers in the parentheses represent 95% confidence intervals) 46

Table 6 Elementary step reactions for CO and CO_2 hydrogenations and the WGS reaction (both redox and carboxyl mechanisms [50]) considered in this work[†] 61

Table 7 Most stable adsorption sites and adsorption energies of all the surface intermediates 75

Table 8 Estimated parameters for adsorption/desorption reactions and surface reactions 82

Table 9 Elementary steps and corresponding rate equations for DME synthesis by methanol dehydration 101

Table 10 Reaction and activation energies for the forward and backward reactions calculated by MP2 (ZPE corrected) 110

Table 11 Bond angle and length within the 4T cluster of H-Z 113

Table 12 Comparison of bond lengths when the methanol was adsorbed to the H-zeolite (adsorbed) and not (isolated) 114

Table 13 Estimated values of pre-exponential factors.............................. 128

Table 14 Desorption rates of DME for R6 and R9 at the reactor outlet at $T = 450$, 475, and 500 K 130

Table 15 The elementary steps for WGS reaction and their activation energies from Gokhale et al.'s work [50]† 139

Table 16 Varied range of operating conditions for making the pre-computed datasets 142

Table 17 Estimated values of the pre-exponential factors for WGS reaction 150

Chapter 1 Introduction

1.1 Research Motivation

As global warming is getting more serious and fossil fuels are depleted, utilization of carbon dioxide, which is one of the main components of greenhouse gases, has gained huge interests by many researchers. Recently, many countries have pledged to achieve carbon neutrality by 2050, and acting to reduce carbon emissions. C1 chemistry, which utilizes one-carbon resources such as methane (CH_4), carbon monoxide (CO) and carbon dioxide (CO_2), is one of sustainable technologies to substitute petroleum. Therefore, C1 chemistry is expected to play an important role in carbon neutrality by utilizing and reducing the greenhouse gases. There have been lots of researches on C1 gas conversion taking place over biological or chemical catalysts. While searching for efficient C1 catalysts is important, mechanism analysis and kinetic modeling for C1 reactions also have significant importance, because there are still many reactions that don't have an established explanation for the mechanism even though C1 reactions are well-known and long-studied.

In order to analyze the reaction kinetics and to predict the behavior of a system, kinetic modeling is needed. The reaction kinetics can be modeled for each purpose, from the simplest power-law model to the complex microkinetic model. In general, a kinetic model predicts the results of reactor outputs such as conversions, selectivities, and production rates by varying operating conditions. In particular, microkinetic analysis has played an important role in understanding fundamentals of elementary steps of surface reactions in catalytic reaction systems [1], and is known to be a useful tool for elucidating reaction mechanisms. A microkinetic model differs from a lumped kinetic model in that it doesn't assume a rate-determining step (RDS) and equilibrated steps, while a lumped kinetic model assumes a RDS and develops the expression based on the RDS.

According to the recent trends where clean production is necessary, kinetic studies in C1 chemistry are required for more efficient C1 gas refinery technologies. The synthesis of methanol and dimethyl ether from syngas (mixture of CO, CO_2 and H_2) is one of important C1 technologies since they can be used as fuel, solvent, and a precursor to various organic compounds. Additionally, biogas, which is composed of methane and CO_2 produced by anaerobic digestion of organic matter, is used for the synthesis of methanol and DME [2]. Recently, Jiang et al. stated the importance of CO_2 conversion to methanol in preparation for the promising approaches to reduce CO_2 emissions [3].

The objective of this thesis is to propose practical microkinetic and lumped kinetic modeling approach and offer fundamental results on the several C1 gas conversion reactions, especially, the methanol and DME synthesis from syngas. Through the combination of first-principles calculations and kinetic parameter estimation by fitting the experimental data, the microkinetic models were developed practically and reliably. The developed models could give valuable contribution to elucidating the reaction mechanisms and optimization of the operating conditions. Moreover, for the purpose of developing the microkinetics applicable to the higher-scale CFD or process simulations, surrogate models based on machine learning methods were presented.

1.2 Outline of the Thesis

The outline of this thesis is as follows: Chapter 1 introduces the thesis by explaining the necessity of the research, and gives the outline with the associated publications. Chapter 2 gives a detailed description of background theories for microkinetic modeling. A lumped kinetic model for the direct synthesis of DME over a hybrid catalyst is developed in Chapter 3, which emphasizes how different a microkinetic model is from a lumped kinetic model. Two microkinetic models for the methanol and DME synthesis are proposed in Chapter 4 and Chapter 5, respectively. In Chapter 6, surrogate models of a microkinetic model for the water-gas shift reaction were developed through machine learning methods for the future combination with the higher-scale simulations.

1.3 Associated Publications

Part of Chapter 2 was written on the basis of [4] which presented trends and outlook of computational chemistry and microkinetic modeling for catalyltic synthesis of methanol and DME. The work presented in Chapter 3 was based on [5]. The work presented in Chapter 4 was based on [6]. The work presented in Chapter 5 was based on [7]. The content of Chapter 6 has not been published yet, but it is being prepared for submission.

Chapter 2 Background Theory

2.1 Microkinetics

The use of a microkinetic analysis on catalytic reaction systems originated from Bush and Dyer's work [8] in 1976, where they conducted an experimental and computational analysis of complicated kinetics for industrial high-temperature chlorocarbon rearrangement and hydrocarbon cracking by evaluating the surface reaction mechanisms to predict the performance of the industrial reactors. Since then, several researchers have considered the detailed catalytic reaction mechanisms in their kinetic modeling [9, 10], and eventually, Dumesic et al. set up the framework of the microkinetics of heterogeneous catalysis [11]. Microkinetics can be the key to understand the reaction mechanism. Because a microkinetic model includes all possible elementary steps, a rigorous investigation of the detailed reaction pathways is possible. In addition, the dominant pathway among the competitive pathways is able to be elucidated through a microkinetic model, which could be, in turn, helpful in designing catalysts and improving the catalytic process by deepening our understanding of the fundamentals of reaction mechanisms.

Although closed-form empirical kinetic models, such as the power-law and Langmuir-Hinshelwood-Hougen-Watson (LHHW) models, have been used widely [12, 13] due to their relatively simple structure and appropriate fitness to experimental data, their limitations in describing changes in the rate-limiting steps under varying operating conditions, as well as the irrelevance of kinetic parameters to the physical meaning, have aroused the necessity of the microkinetic modeling approach. To develop a microkinetic model, the overall reactions are divided into elementary steps which consist of several competitive pathways. With the possible candidates of elementary steps, a microkinetic model is developed, and, by using the microkinetic model, the role of each step is evaluated and the dominant pathway is elucidated.

Microkinetic modeling can be categorized as multiscale modeling of catalytic reactions as shown in Figure 1. Calculations for various length and time scales are performed to obtain electronic structures, reaction rates and reactor outputs. Kinetic parameters for all elementary reactions should be delivered to a kinetic model for calculating the reaction rates which are the essential values for reactor modeling. There are several methods to derive each value: Kinetic parameters are related to the electronic structure of reactants and products, and those can be calculated by computational chemistry or the semi-empirical methods such as the unity bond index-quadratic exponential potential (UBI-QEP) method and the Brønsted-Evans-Polanyi (BEP) relation; At the mesoscopic scale, the mean-field kinetic model including the lumped kinetic or microkinetic model that assumes the averaged environments of surface types and surface intermediates, and the kinetic Monte Carlo method are most frequently employed to compute reaction rates and derived results of the reactions like the conversion, product distribution, and so on; The kinetic model is implanted in the reactor model consisting of balance equations with the rate expressions. The reactor model can be a simple continuous stirred-tank reactor (CSTR), plug flow reactor (PFR) or combination of them. When the effect of the flow pattern on reactions is important, computational fluid dynamics (CFD) is used.

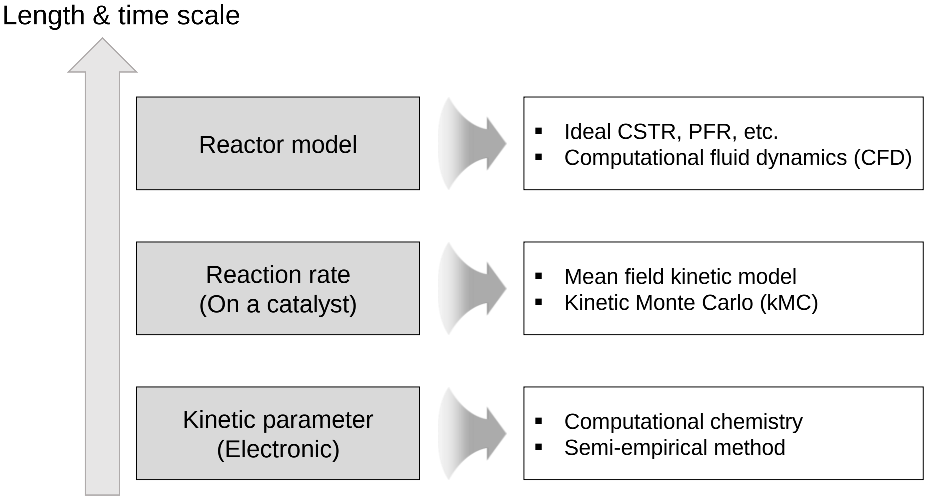

Figure 1 Multiscale modeling in a microkinetic model.

A microkinetic model is defined as a system of ordinary differential equations (ODEs) for the site balances:

$$\frac{d\theta_\mathrm{j}}{dt} = \sum_\mathrm{i} S_\mathrm{ij} r_\mathrm{i} \qquad (2.1)$$

where θ_j is the site fraction of the surface intermediate j, S_ij the stoichiometric coefficient, and r_i the rate of the reaction i. For all surface intermediates, Equation (2.1) is calculated simultaneously, and, by calculating the equations, the site fractions and the reaction rates are obtained. The consumption and production rates of gaseous species can be calculated through the adsorption and desorption equations with a reactor model. Furthermore, in addition to the dominanty pathway, the most abundant surface intermediate and rate-limiting steps can be elucidated as a result of the calculations. However, the kinetic parameter and reaction rate of each elementary step have various orders of magnitude, making the ODE system so stiff that it may become difficult to solve the ODEs. For reducing the stiffness, several solutions, such as scaling and the quasi-equilibrium assumption, have been proposed and adopted.

2.2 Kinetic Parameter

The kinetic parameters for each elementary step reaction should be determined to calculate the reaction rate. For each surface reaction, reaction rates are formulated by the following:

$$r_{\mathrm{i}} = k_{\mathrm{i}} \prod_{\mathrm{j}} \theta_{\mathrm{j}} = A_{\mathrm{i}} \exp\left(-\frac{E_{\mathrm{a}}}{RT}\right) \prod_{\mathrm{j}} \theta_{\mathrm{j}} \tag{2.2}$$

where k, A, and E_a are the kinetic parameters of the reaction i, the pre-exponential factor, and the activation energy, respectively. θ_j represents the portion of the surface intermediate j in the total catalytic active site over a catalytic surface. In the equation, the subscript j represents the reactants involved in the i-th reaction to comprise the terms of the driving forces, while the kinetic parameters were assumed to follow the Arrhenius type equation. The rate of the i-th elementary step (r_i) is expressed by the multiplication of the kinetic parameter and driving forces. Calculating A and E_a for each elementary step is one of the main problems in microkinetic modeling, and there are several different ways to obtain the parameters. When the computational chemistry is limited by poor computing power, the parameters are estimated by fitting experimental data. Due to its enhancement in computing capacity, computational chemistry is widely used, although it is still burdensome to calculate the parameters for a large amount of elementary steps. Accordingly, the BEP relations (also known as the linear free energy relations) [14, 15] and the unity bond index-quadratic exponential potential (UBI-QEP) method (also known as the bond-order conservation method) [16] are often used for more practical approaches. In 2011, Maestri and Reuter [17] proposed the refined UBI-QEP method, which could derive activation energies that have values similar to those derived from the DFT.

2.2.1 Computational Chemistry

First-principle modeling for catalytic reaction systems is a combination of solid state physics and surface chemistry [18]. It can be used to find the electronic structure of a catalyst, which relates to its reactivity on the surface, where the bonds of reactant molecules break to form new bonds. Using a computational catalyst is a paradigm shift approach in contrast to the trial and error method that has been used for decades [19], as it can rapidly replace conventional experimental tools, including infrared (IR), X-ray diffraction (XRD), and Raman spectra. Previously, detailed reaction mechanisms were hard to completely understand because the reaction networks are very complex and little was known about their physicochemical exactness [20]. However, the first-principle approach makes it possible to analyze a specific elementary reaction of a reaction system, thereby shedding light on the reaction mechanisms of many catalytic systems.

In order to solve the many-body Shrödinger equation easily, there have been many quantum chemical approaches. Representatively, Density functional theory (DFT) rests on two fundamental theorems which were proved by Hohenberg and Kohn: *Theorem 1. The total energy from Shrödinger equation is a unique functional of the electron density*, which means there is a one-to-one mapping between the ground-state wave function and the ground-state electron density; *Theorem 2. The electron density that minimizes the total energy is the true ground-state density*. The Kohn-Sham equation based on the Hohenberg-Kohn theorems is different from Shrödinger equation in that it is described in terms of the single-electron wave functions. The equation is as follows:

$$\left[-\frac{\hbar^2}{2m}\nabla^2 + V_{\mathrm{ext}}(\vec{x}) + V_{\mathrm{H}}(\vec{x}) + V_{\mathrm{XC}}(\vec{x})\right]\psi(\vec{x}) = E\psi(\vec{x}) \tag{2.3}$$

where m is the electron mass, V_{ext} the potential defining the interaction between an electron and the collection of atomic nuclei, V_{H} the Hartree potential, V_{XC} the potential defining exchange and correlation contributions, ψ the single-electron wave function, and E the ground-state energy.

Furthermore, the methods using localized and spatially extended functions, wave-function-based methods, Hartree-Fock method, and post-Hartree-Fock methods such as configuration interaction, coupled cluster, Møller-Plesset perturbation theory, and the quadratic configuration interaction approach have also been used. With the various quantum chemical approaches, exploration of the properties and energies of molecules is possible, and kinetic parameters of reactions can be derived.

2.2.2 Transition State Theory

Transition state theory (TST) assumes quasi-equilibrium between the reactants and an activated complex ($A + B \leftrightarrow AB^{\ddagger} \rightarrow P$). Unlike collision theory, TST incorporates information about molecular structure. The kinetic parameter of the forward reaction is derived in terms of the equilibrium constant for the activated complex formation.

$$k = \frac{k_{\mathrm{B}}T}{h}K^{\ddagger} = \frac{k_{\mathrm{B}}T}{h}\exp\left(\frac{\Delta S^{0\ddagger}}{k_{\mathrm{B}}}\right)\exp\left(\frac{-\Delta H^{0\ddagger}}{k_{\mathrm{B}}T}\right) \tag{2.4}$$

where k_{B} is the Boltzmann constant, h the Planck constant, $\Delta S^{0\ddagger}$ the entropy change and $\Delta H^{0\ddagger}$ the enthalpy change for the activated complex formation. In the Equation (2.4), $\frac{k_{\mathrm{B}}T}{h}\exp\left(\frac{\Delta S^{0\ddagger}}{k_{\mathrm{B}}}\right)$ and $\exp\left(\frac{-\Delta H^{0\ddagger}}{k_{\mathrm{B}}T}\right)$ terms are related to the A and $\exp\left(-\frac{E_a}{RT}\right)$ of the Equation (2.2), respectively. The microscopic formulation of TST is described with regard to molecular partition functions which are a product of contributions from translational, rotational, and vibrational degrees of freedom for reactants and activated complex.

$$q = q_{\mathrm{trans}}q_{\mathrm{vib}}q_{\mathrm{rot}} \tag{2.5}$$

For a 3-dimensional molecule, the respective expressions are as follows:

$$q_{\mathrm{trans}} = \left(\frac{\sqrt{2\pi m_{\mathrm{i}}k_{\mathrm{B}}T}}{h}\right)^3 \tag{2.6}$$

$$q_{\mathrm{vib}} = \prod_{\mathrm{j}}^{\#\ of\ modes}\frac{1}{1-\exp\left(-\frac{h\nu_{\mathrm{ij}}}{k_{\mathrm{B}}T}\right)} \tag{2.7}$$

$$q_{\mathrm{rot,lin}} = \frac{8\pi^2 I_{\mathrm{lin}}k_{\mathrm{B}}T}{\sigma_{\mathrm{r}}h^3} \tag{2.8}$$

$$q_{\mathrm{rot,nonlin}} = \frac{8\pi^2\sqrt{8\pi^3 I_1 I_2 I_3 (k_\mathrm{B}T)^2}}{\sigma_\mathrm{r} h^3} \tag{2.9}$$

where m_i the mass of the molecule i, v_ij the molecule i's vibrational frequency in the j-th mode, I_lin the moment of inertia about the molecular axis of the linear molecule, I_1, I_2, and I_3 the moments of inertia about the three principal axes of the nonlinear molecule, and σ_r the rotational symmetry number.

With regard to the reaction, $\mathrm{A} + \mathrm{B} \leftrightarrow \mathrm{AB}^\ddagger \rightarrow \mathrm{P}$, the kinetic parameter k can be expressed in terms of the partition functions as follows:

$$k = \frac{k_\mathrm{B}T}{h}\frac{q_{\mathrm{AB}^\ddagger}}{q_\mathrm{A}q_\mathrm{B}}\exp\left(\frac{-\Delta H^{0\ddagger}}{k_\mathrm{B}T}\right) \tag{2.10}$$

Therefore, the corresponding pre-exponential factor A is equal to $\frac{k_\mathrm{B}T}{h}\frac{q_{\mathrm{AB}^\ddagger}}{q_\mathrm{A}q_\mathrm{B}}$.

In particular, the quantum chemistry introduced above is able to calculate vibrational frequency and enthalpy change. For example, the climbing image nudged elastic band method (CI-NEB) [21-23] is most widely used for finding transition states, therefore, activation energies or diffusion barriers. The actual applications were shown in the following chapters.

2.2.3 UBI-QEP

The UBI-QEP method is a semi-empirical method to simply calculate adsorption energies and activation energies [16]. Two-body interactions in a many-body system are assumed to be described by the quadratic potential of the exponential function of the two-center bond distance, i.e., the bond index, and the sum of all the bond indices is conserved as unity. Based on this method, once the enthalpies of the gas-phase species and adsorption energies of the surface intermediates are known, the activation energies can be calculated with a very low computational load. Although the activation energies can also be obtained using the CI-NEB, it may be an inefficient method in the case of microkinetic modeling with many elementary-step reactions in terms of its computational burden. Table 1 provides the equations to calculate the activation energies.

Table 1 Equations for calculation of the activation energies by the UBI-QEP[†]

Reaction type	Reaction formula	Activation energy
Dissociative adsorption	AB + 2* → A* + B*	$E_{\mathrm{f}} = \phi\left(\Delta H_{\mathrm{rxn}} - Q_{\mathrm{AB}} + \frac{Q_{\mathrm{A}}Q_{\mathrm{B}}}{Q_{\mathrm{A}} + Q_{\mathrm{B}}}\right)$
Dissociation reaction	AB* + * → A* + B*	$E_f = \phi\left(\Delta H_{\mathrm{rxn}} + \frac{Q_{\mathrm{A}}Q_{\mathrm{B}}}{Q_{\mathrm{A}} + Q_{\mathrm{B}}}\right)$
Disproportionation reaction	A* + B* → C* + D*	$E_f = \phi\left(\Delta H_{\mathrm{rxn}} + \frac{Q_{\mathrm{C}}Q_{\mathrm{D}}}{Q_{\mathrm{C}} + Q_{\mathrm{D}}}\right)$

[†] E_{f}: activation energy of the forward reaction, ϕ: bond index ($0 < \phi < 1$), Q: adsorption energy.

Chapter 3 Lumped kinetic modeling for direct synthesis of DME from syngas

3.1 Background

Dimethyl ether (DME), the simplest ether, is a promising and economically alternative fuel for future applications. In recent years, the interest in DME as an additive or a blend-diesel fuel has increased considerably. It is an environmentally friendly compound because it has low global warming potentials due to its high cetane number, high oxygen content, and lack of C-C bonds, along with good combustion properties; low NO_x, particulate matter (PM), SO_x, and emissions compared to those of traditional diesel fuels. For these characteristics, DME fuel can fully or partially replace conventional diesel fuel [24].

DME is usually synthesized in two steps; methanol (MeOH) synthesis from syngas (CO and H_2) by CO and CO_2 hydrogenation and water-gas shift reaction (the overall reactions are listed below), followed by MeOH dehydration. In the conventional two-step DME synthesis, the commercial catalyst $Cu/ZnO/Al_2O_3$ (CZA) is frequently used to synthesize MeOH, and acid catalysts such as zeolites are used to dehydrate MeOH. Recently, the direct synthesis of DME from syngas has been suggested by introducing two functionally independent catalysts, composed of one component for the formation of MeOH and the other for dehydration. In this work, a hybrid catalyst consisting of CZA and ferrierite (FER) with a core-shell structure was used. The co-production of MeOH and DME by the hybrid catalysts obviates the use of additional reactors and separation units, and alleviates the equilibrium limitation of the MeOH synthesis, resulting in a significant increase in MeOH productivity [25, 26].

$\mathrm{CO} + 2\mathrm{H_2} \rightleftarrows \mathrm{CH_3OH}$	CO hydrogenation
$\mathrm{CO_2} + \mathrm{H_2} \rightleftarrows \mathrm{CO} + \mathrm{H_2O}$	Water-gas shift reaction
$\mathrm{CO_2} + 3\mathrm{H_2} \rightleftarrows \mathrm{CH_3OH} + \mathrm{H_2O}$	CO_2 hydrogenation
$2\mathrm{CH_3OH} \rightleftarrows \mathrm{CH_3OCH_3} + \mathrm{H_2O}$	MeOH dehydration

There have been many studies on the kinetics of the conversion of syngas to MeOH using copper-based catalysts. Klier et al. suggested a kinetic model based on two types of reactions; MeOH synthesis by the hydrogenation of CO and the redox equilibrium between CO and CO_2 [27]. Coteron and Hayhurst developed a kinetic model that neglects the contribution of CO to MeOH production and converts it to CO_2 by water-gas shift reactions [28]. Chinchen et al. suggested, by referring to Coteron and Hayhurst's study, that CO_2 is the main source of carbon for MeOH synthesis when both CO and CO_2 are used as the feed gas [29]. Bussche and Froment developed a kinetic model to describe the dissociative adsorption of H_2 and CO_2 on copper surfaces under the assumption of negligible CO hydrogenation [30], which was further evaluated by Peter et al. [31] Meanwhile, Graaf et al. assumed that both CO and CO_2 contribute to MeOH production, and suggested a kinetic model on the basis of the competitive adsorption of CO and CO_2 on copper surfaces and competitive adsorption of H_2 and H_2O to zinc sites [32]. Park et al. suggested a three-site adsorption model by considering different adsorption sites for CO and CO_2 [33]. In addition, several studies have incorporated microkinetic modeling to investigate reaction kinetics and mechanisms for MeOH synthesis over a copper-based catalyst [6, 34].

Several papers have been reported on DME synthesis by MeOH dehydration. Bercic and Levec developed a kinetic model that assumes that the surface reaction is a rate-controlling step, and MeOH is adsorbed on the γ-Al_2O_3 surface in a dissociative manner [35]. Ng et al. further used this model to investigate the combined kinetics of MeOH synthesis by CO2 hydrogenation and MeOH dehydration [25]. Hadipour and Soharabi studied the conditions under which both MeOH synthesis by CO hydrogenation and MeOH dehydration occurs [36]. A microkinetic model was presented for DME synthesis from MeOH [7]. Although there are some studies on the kinetic modeling of the direct synthesis of DME from syngas [36-39], most involved the use of γ-Al_2O_3 as the acid catalyst for MeOH dehydration.

In this chapter, kinetic modeling was conducted for the direct synthesis of DME from syngas over a hybrid CZA/FER catalyst, and the developed kinetics were compared with those reported for MeOH synthesis over a CZA catalyst and MeOH dehydration over a zeolite catalyst. In addition, the developed kinetic model could be used to investigate the effects of operating conditions on catalytic performances.

3.2 Methods

3.2.1 Experimentals

The hybrid CZA/FER catalyst was synthesized by a coprecipitation method using a lab-made seed-derived FER. The seed-derived FER was synthesized using the previously synthesized FER seed (Si/Al molar ratio of 12) through a hydrothermal synthesis. For the FER seed, the precursor solution was prepared with fumed silica (SiO_2), sodium aluminate ($NaAlO_2$), piperidine ($C_5H_{11}N$, an organic structure directing agent (OSDA)), sodium hydroxide (NaOH), and deionized water (DIW) with a molar ratio of SiO_2/$NaAlO_2$/piperidine/NaOH/DIW = 1/0.096/0.9/0.14/40. The solution was vigorously stirred for 12 h, before it was hydrothermally synthesized for 7 days at 160 °C under the stirring condition. After the hydrothermal synthesis, the prepared zeolite gel was washed several times with sufficient DIW and then dried in an oven at 80 °C overnight. The dried powder was successively calcined at 550 °C at a ramping rate of 1 °C/min for 6 h to synthesize the Na-form seed-derived FER. The seed-derived FER was synthesized using a similar procedure as the previous Na-form FER seed (24 wt%), but without OSDA (SiO_2/$NaAlO_2$/NaOH/DIW = 1/0.096/0.14/40) in the slurry-phase. After stirring for 12 h, the synthesized white gel was washed several times and ion-exchanged to form H-form FER. The sample was dried at 80 °C and calcined at 550 °C for 3 h.

To prepare the CZA/FER hybrid catalyst, 1 g of the seed-derived FER was dispersed in 200 mL of DIW. The solution was kept at 70 °C under a fixed pH 7 and continuously stirred. A metal precursor solution containing Cu, ZnO, and

Al nitrate precursors (molar ratio of $Cu/ZnO/Al_2O_3 = 7/3/1$), and an ammonium carbonate solution, which was dissolved in DIW to control the pH during coprecipitation, were slowly and separately added to the FER-containing slurry. After the coprecipitation step, the solution was filtered by DIW, dried in an oven at 80 °C, and calcined at 350 °C for 3 h at a ramping rate of 1 °C/min.

The experimental conditions are described in Table 2; for runs 1–4, 5–7, 8–10, and 11–12 the temperature, total pressure, GHSV, and stoichiometric ratio ($H_2/(2CO + 3CO_2)$) were varied, respectively. A fixed-bed tubular reactor was used, which had a reactor length and inner diameter of 45.3 and 0.7 cm, respectively. For the kinetic experiments, 0.4 g of the seed-derived FER (1.2 cm packing depth) was loaded and pretreated at 400 °C for 6 h under a N_2 flow.

Table 2 Experimental conditions

Run	T [°C]	P_{total} [bar]	GHSV [L/(kg$_{cat}$·h)]	CO/CO$_2$/H$_2$/N$_2$ [vol%]	H$_2$/(2CO + 3CO$_2$)
1	180	50	2,000	21/9/66/4	0.96
2	200	50	2,000	21/9/66/4	0.96
3	220	50	2,000	21/9/66/4	0.96
4	250	50	2,000	21/9/66/4	0.96
5	250	20	2,000	21/9/66/4	0.96
6	250	30	2,000	21/9/66/4	0.96
7	250	40	2,000	21/9/66/4	0.96
8	250	50	4,000	21/9/66/4	0.96
9	250	50	6,000	21/9/66/4	0.96
10	250	50	8,000	21/9/66/4	0.96
11	250	50	2000	15/6.4/73.9/4.7	1.5
12	250	50	2,000	11.5/4.9/79.4/4.2	2.1

3.2.2 Kinetic Model

The DME synthesis reaction simultaneously occurs in two parts of the hybrid catalyst: (1) MeOH synthesis over a CZA surface and (2) dehydration of MeOH over a FER surface. The other reactions forming byproducts such as formaldehyde, formic acid, methane, ethylene, and so on were neglected based on the experimental results in which the selectivities of byproducts were below 1 carbon-mole%. The reactants CO, H_2, and CO_2 were assumed to adsorb on different sites of CZA during MeOH synthesis under the assumption of three site adsorption [27, 40]. The reaction rate equations were adopted from the literature [25, 33]. The rate expressions are listed in Table 3, and their derivations can be found in the literature [25, 33].

Table 3 Reaction rate equations and estimated kinetic parameters

Reaction	Rate equation	Unit
CO hydrogenation	$R_1 = \frac{k_1 K_{\mathrm{CO}}\left[f_{\mathrm{CO}} f_{\mathrm{H_2}}^{1.5} - f_{\mathrm{MeOH}}/\left(K_{\mathrm{p,1}} f_{\mathrm{H_2}}^{0.5}\right)\right]}{\left(1 + K_{\mathrm{CO}} f_{\mathrm{CO}}\right)\left(1 + K_{\mathrm{H_2}}^{0.5} f_{\mathrm{H_2}}^{0.5} + K_{\mathrm{H_2O}} f_{\mathrm{H_2O}}\right)}$	mol/(kg$_{\mathrm{cat}}$·s)
Water-gas shift reaction	$R_2 = -\frac{k_2 K_{\mathrm{CO_2}}\left[f_{\mathrm{CO_2}} f_{\mathrm{H_2}} - f_{\mathrm{CO}} f_{\mathrm{H_2O}}/K_{\mathrm{p,2}}\right]}{\left(1 + K_{\mathrm{CO_2}} f_{\mathrm{CO_2}}\right)\left(1 + K_{\mathrm{H_2}}^{0.5} f_{\mathrm{H_2}}^{0.5} + K_{\mathrm{H_2O}} f_{\mathrm{H_2O}}\right)}$	
CO$_2$ hydrogenation	$R_3 = \frac{k_3 K_{\mathrm{CO_2}}\left[f_{\mathrm{CO}} f_{\mathrm{H_2}}^{1.5} - f_{\mathrm{H_2O}} f_{\mathrm{MeOH}}/\left(K_{\mathrm{p,3}} f_{\mathrm{H_2}}^{1.5}\right)\right]}{\left(1 + K_{\mathrm{CO_2}} f_{\mathrm{CO_2}}\right)\left(1 + K_{\mathrm{H_2}}^{0.5} f_{\mathrm{H_2}}^{0.5} + K_{\mathrm{H_2O}} f_{\mathrm{H_2O}}\right)}$	
MeOH dehydration	$R_4 = \frac{k_4 K_{\mathrm{MeOH}}^2\left[C_{\mathrm{MeOH}}^2 - \left(C_{\mathrm{H_2O}} C_{\mathrm{DME}}\right)/K_{\mathrm{p,4}}\right]}{\left(1 + 2\sqrt{K_{\mathrm{MeOH}} C_{\mathrm{MeOH}}} + K_{\mathrm{H_2O,DME}} C_{\mathrm{H_2O}}\right)^4}$	

† Other kinetic parameters are available in the literature [32, 33, 41] and were used without modification.

‡ The units of the fugacity (f_i) and concentration (C_i) are bar and mol/m^3, respectively. k, K_i, and $K_{P,j}$ are the reaction rate constant, adsorption equilibrium constant of species i, and equilibrium constant of reaction j, respectively. R is the gas constant (8.314 J/(mol·K)).

Although different terms were used for the driving forces; fugacities and concentrations for MeOH and DME synthesis, respectively, the reported rate equations were used without modification to facilitate the comparison between the kinetic parameters of the present chapter and the reported ones. For the calculation of the fugacity, the assumption of an ideal solution was made to calculate the fugacities of pure components, and the virial equations were used with the reduced temperature and pressure [42]. The kinetic parameters can be expressed in the form of Arrhenius equations, as follows:

$$k_{\mathrm{i}} = A \exp\left(-\frac{E_{\mathrm{a,i}}}{RT}\right) \tag{3.1}$$

$$K_{\mathrm{i}} = A \exp\left(-\frac{\Delta H_{\mathrm{i}}}{RT}\right) \tag{3.2}$$

where k, K, A, E_a, and ΔH denote the reaction rate constant, equilibrium constant, frequency factor, activation energy, and reaction enthalpy, respectively.

Among the kinetic parameters of the rate equations, six parameters including k_1, k_2, k_3, k_4, K_{MeOH}, and $K_{\mathrm{H_2O,DME}}$, which play significant roles in determining the rates, were estimated by fitting the experimental data. All other parameters were obtained from previous studies [32, 33, 41] and used without modification to reduce the number of parameters to be estimated. It is worth noting that the parameters involving the adsorption were assumed to be the same since adsorption sites for syngas and MeOH were separately located in hybrid catalysts due to the core-shell structure and thus, the adsorption behaviors between conventional and hybrid catalysts are similar. Besides, the parameters involving the adsorption behaviors little changed while the iterative calculations being conducted in the estimation, and it was also observed that the different values of initial estimates for those parameters little influenced on the rate, indicating the insensitiveness of the parameters to the reaction rate.

The external mass transfer and internal pore diffusion limitations were assumed to be negligible because powder catalysts were used. To validate the effectiveness of the assumption, the dimensionless Mears parameters were calculated under all experimental conditions of the present chapter and the values were less than 2.17×10^{-6} (much lower than the threshold value of 0.15), confirming a negligible external mass diffusion [43]. The presence of any internal pore diffusion limitation was evaluated using the dimensionless Weisz-Prater number (C_{WP}), which is defined as the ratio of the dispersion and convection transport rates (the reciprocal of the dimensionless Péclet number) [43]. This parameter was calculated using the correlation of the effective diffusivity (D_{e}) [44], and the calculated value of C_{WP} was 1.57×10^{-5}, which is less than the threshold value of 1.0, indicating that there was no internal diffusion limitation. Based on the above assumptions, a pseudo-homogeneous one-dimensional reactor model with the following balance equations was considered.

Mass balance: $-u_{\mathrm{s}}\frac{dC_{\mathrm{i}}}{dz} + \rho_{\mathrm{B}}\sum_{\mathrm{j=i}}^{NR} R_{\mathrm{i,j}} = 0$

Energy balance: $\rho_g u_s C_p \frac{dT}{dz} = \rho_B \sum_{j=1}^{NR} (-\Delta H)_j R_j + \frac{4U}{D_t} (T_w - T)$

Boundary conditions: $C_i = C_{i,in}$, $T = T_{in}$ at $z = 0$

The kinetic parameters were estimated by minimizing the objective function (F_{obj}), which is the sum of the residuals of the square errors of the objective elements as follows:

$$F_{obj} = \sum_{n}^{NE} \left[\sum_{i} w_i \left(\frac{y_{i,calc} - y_{i,exp}}{y_{i,exp}} \right)^2 \right]_n \tag{3.3}$$

where, NE and w_i denote the number of experimental conditions and weighting factor, respectively. The subscript 'calc' and 'exp' represent the calculated values and experimental data, respectively, and the elements of the objective function considered in the present chapter were the conversions of CO and CO_2, and selectivities of MeOH and DME.

The estimation was performed using the "lsqcurvefit" subroutine in MATLAB (MathWorks, Inc.), and the Levenberg-Marquardt method was applied. It is worthing noting that, since the number of elements in the objective function was 4 (2 conversions and 2 selectivities), a total of 48 data were used in the estimation to guarantee the reliability of the estimated parameters.

3.3 Application Results and Discussion

Figure 2 shows a comparison of the conversions and selectivities of the experimental data and simulated results with the estimated kinetic parameters (Tables 4 and 5); the model effectively demonstrated the experimental behaviors. The values of the mean of the absolute relative residual (MARR) for the conversions of CO and CO_2 and selectivities of MeOH and DME, were 14.73, 37.67, 34.62, and 2.15%, respectively, while the corresponding values of the relative standard deviation of individual error (RSDE) were 11.93, 43.97, 37.77, and 1.47%, respectively. When it comes to the CO_2 conversion, there were large deviations for some conditions. This is partly attributed to that there was a limit to better describe the CO_2 conversion in the current model, indicating that a more sophisticated kinetic model might be needed for reducing the error in the future. Another plausible reason for the large deviation might be measurement errors. As shown in Figure 2, some of the experimental data of CO_2 conversion significantly deviated from the trend of simulation results.

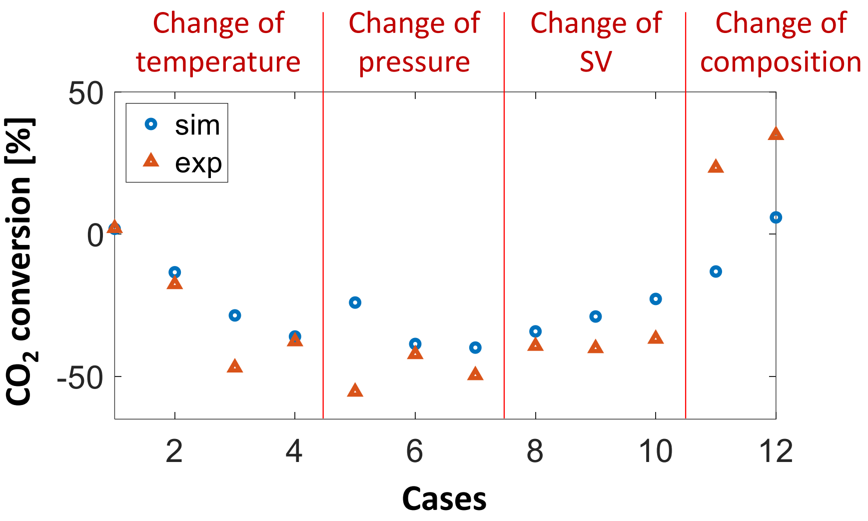

Figure 2 Comparisons of CO_2 conversions between experimental data and calculation results (experimental conditions for each case are referred to Table 2)

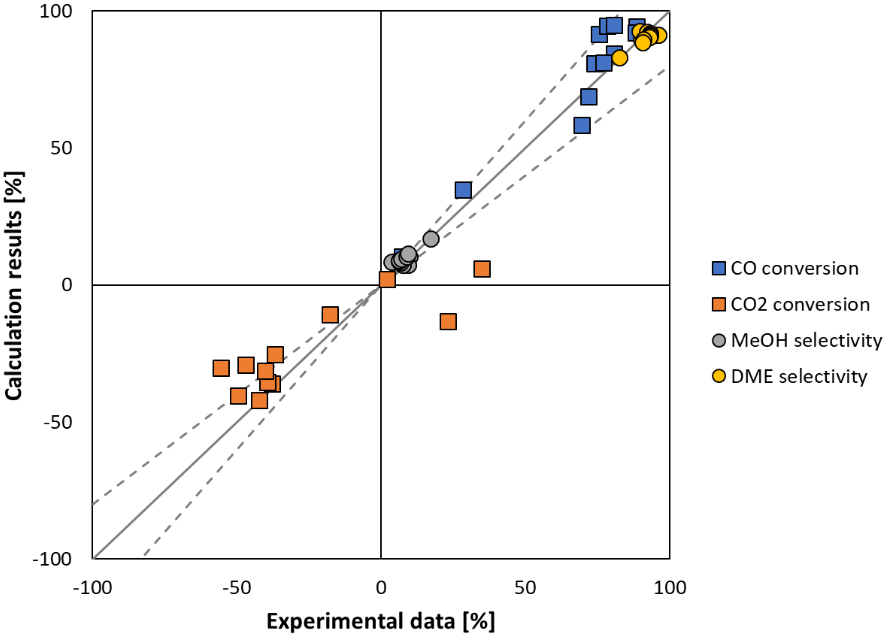

Figure 3 Parity plot of the experimental data versus the calculation results of the CO (blue rectangle) and CO_2 (orange rectangle) conversions, and MeOH (gray circle) and DME (yellow circle) selectivities. The dotted lines represent the ±20% errors.

Table 4 Estimated kinetic parameters for MeOH synthesis from syngas of the present and previous studies (numbers in the parentheses represent 95% confidence intervals)

Parameter		This work	Park et al. [33]	Graaf et al. [32]	Klier et al. [27]	Coteron and Hayhurst [28]	Skrzypek et al. [45]	Seidel et al. [46]	Units
k_1	A	1.50E+09 (±4.60E+07)	1.88E+08	2.69E+07	4.36E+05	1.99E+02	-	2.02E+09	$\mathrm{mol/(kg_{cat} \cdot s \cdot bar^{1.5})}$
	E_a	125,757 (±16,240)	113,711	109,900	69,160	65,100		113,905	J/mol
k_2	A	6.08E+09 (±1.08E+10)	1.16E+10	7.31E+08	-	-	6.94E+08	1.34E+08	$\mathrm{mol/(kg_{cat} \cdot s \cdot bar)}$
	E_a	116,370 (±66,950)	126,573	123,400			104,700	102,101	J/mol
k_3	A	7.04E+05 (±9.07E+04)	7.08E+04	4.36E+02	4.51E+00	3.16E+00	8.33E+08	2.68E-01	$\mathrm{mol/(kg_{cat} \cdot s \cdot bar^{1.5})}$
	E_a	88,777 (±3,557)	68,252	65,200	47,190	47,000	104,700	14,992	J/mol
Catalyst		CZA/FER	CZA	CZA	CZ	CZ	CZA	CZA	

Table 5 Estimated kinetic parameters for DME synthesis from MeOH of the present and previous studies (numbers in the parentheses represent 95% confidence intervals)

Parameter		This work	Ng et al. [25]	Bercic and Levec [35]	Unit of *k* or *K*
k_4	A	8.28E+11 (±1.25E+13)	3.70E+10	5.35E+13	$\mathrm{mol/(kg_{cat} \cdot s)}$
	E_a	122,427 (±71,240)	105,000	143,666	J/mol
K_{MeOH}	A	7.80E-03 (±1.22E-01)	7.90E-04	5.39E-04	$\mathrm{m^3/kmol}$
	ΔH	-54,489 (±442,600)	-70,500	-70,560	J/mol
$K_{\mathrm{H_2O,DME}}$	A	1.49E-02 (±2.14E+00)	8.40E-02	8.47E-02	$\mathrm{m^3/kmol}$
	ΔH	-21,489 (±575,100)	-41,100	-42,152	J/mol
Catalyst		CZA/FER	CZA/γ-alumina	γ-alumina	

As shown in Table 4, the kinetic parameters, including the frequency factor (A) and activation energy (E_a), obtained in this work and those of Park et al. [33] differed, and this may possibly be attributed to the hybridization of CZA with FER. By hybridizing CZA, both activation energies and frequency factors of the CO and CO_2 hydrogenations increased, while those of the water-gas shift reaction decreased.

The differences in the k_4, K_{MeOH}, and $K_{\mathrm{H_2O,DME}}$ parameters obtained in this work and those of Ng et al. [25] given in Table 5, are attributed to their use of γ-Al_2O_3 for the MeOH dehydration. Both the activation energy and frequency factor of MeOH dehydration (k_4) were greater than those of the Ng et al. study [25]. For the adsorption equilibrium constants, K_{MeOH} and $K_{\mathrm{H_2O,DME}}$, the heats of adsorption (ΔH) were greater than previously reported values, while the estimations of the frequency factors for K_{MeOH} and $K_{\mathrm{H_2O,DME}}$ were greater and less than those of the conventional catalyst, respectively.

The semi-log plot of Figure 4 was used to further analyze the effects of the hybridization of the catalysts. As shown in Figure 4, the frequency factors of the parameters vary greatly, while the activation energies have similar orders-of-magnitude. The activation energies of the CO and CO_2 hydrogenations and water-gas shift reactions over the CZA/FER catalyst were determined to be relatively high compared to those over CZA: the CO hydrogenation provided the highest value of all of the $E_{a,1}$ parameters, and the estimated values of $E_{a,2}$ and $E_{a,3}$ were high, indicating that the MeOH synthesis step over the hybrid catalyst may have more control over the rate than the MeOH dehydration step.

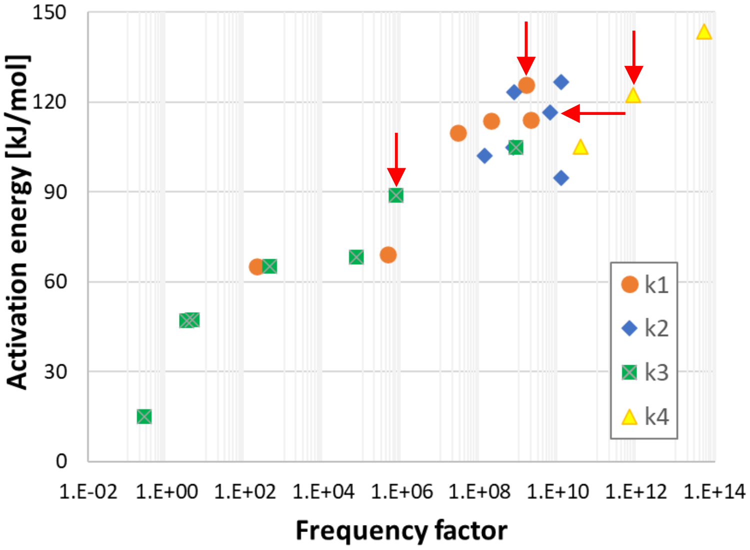

Figure 4 Semi-log plot for a comparison of the estimated kinetic parameters for the hybrid catalyst with those reported in the literature. The units of the frequency factors for each parameter are given in Tables 4 and 5. The red arrows indicate the estimated parameters in the present work.

Previous chapter considered a combination of density functional theory (DFT) and the semi-empirical unity bond index-quadratic exponential potential (UBI-QEP) method [6]. This chapter also supports the above discussion by showing that the activation energy of the rate determining step (RDS), overlapped by both CO and CO_2 hydrogenations, was 105,169 J/mol, which is lower than the activation energies over the hybrid catalyst. In the case of MeOH dehydration (k_4), the activation energy of the hybrid CZA/FER catalyst was reduced compared to Chapter 5's result of 257,519 J/mol for the DME formation reaction via the dissociative pathway, obtained by computational chemistry based on the zeolite catalyst only. Therefore, owing to the hybridization of the two different functional catalysts, the activation barrier of the MeOH synthesis was greater than that of the conventional catalyst, while that of DME synthesis was less, plausibly indicating that MeOH synthesis could become a RDS over DME synthesis. This feature may be attributed to the core-shell structure of the catalyst where CZA occupied the inside of the catalyst, resulting in diffusion resistance.

The developed model was used to evaluate the effects of operating conditions on the catalytic performances. As shown in Figure 5 (a), as the temperature increased from 180 to 230 °C, the CO conversion increased. After it reached the maximum, a slight decrease with temperature was shown, while the CO_2 conversion decreased. Further increases in temperature resulted in negative values, which meant that CO_2 was produced rather than consumed. At high temperatures greater than 220 °C, the CO_2 conversion also showed saturated behavior. The selectivity of MeOH decreased with increasing temperature, while that of the DME increased, reaching a plateau at 220 °C

(Figure 5 (b)). The reactions occurring below 220 °C are in the kinetically controlled regime, whereas reactions occurring above this temperature fall under the thermodynamically controlled regime. Therefore, the recommended optimal reaction temperature range is 200 to 220 °C for increasing the thermal energy efficiency. Besides, the kinetic model confirmed CO conversion showed the positive effects of temperature even at high temperature, which implies that the reaction still stays in the kinetic regime rather than the thermodynamically-controlled region. In other words, the thermodynamic equilibrium limitation of CO conversion could be overcome by hybridizing the two catalysts.

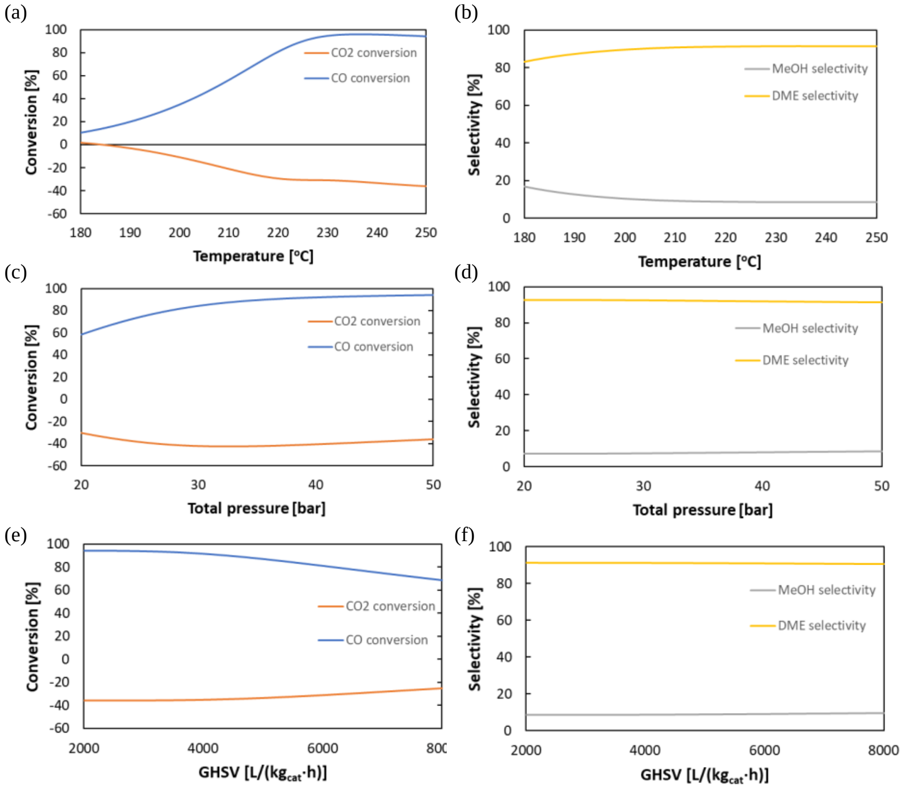

Figure 5 Effects of operating conditions on the conversions (left column) and selectivities (right column); the first, second, and third rows show the effects of temperature, total pressure, and GHSV, respectively. The fixed conditions were: P_{total} = 50 bar, GHSV = 2,000 L/(kg$_{cat}$·h), and $CO/CO_2/H_2/N_2$ = 21/9/66/4% for varying temperature; T = 200 °C, GHSV = 2,000 L/(kg$_{cat}$·h), and $CO/CO_2/H_2/N_2$ = 21/9/66/4% for varying total pressure; and T = 200 °C, P_{total} = 50 bar, and $CO/CO_2/H_2/N_2$ = 21/9/66/4% for varying GHSV.

Positive effects of the total pressure on the CO conversion were observed for the entire range, while CO_2 conversion was inversely influenced by the pressure (Figure 5 (c)). As negligible effects of the pressure on the selectivities were observed (Figure 5 (d)), the optimal pressure may range between 30 and 40 bar, which coincides with the usual operating pressure in commercial processes.

As shown in Figure 5 (e), the lower the GHSV, the higher the CO conversion, as a low GHSV corresponds to a high residence time. However, the selectivities were not significantly influenced by the GHSV. Considering the degree of the increase in the CO conversion for a low GHSV, the optimal reactor size can be determined so that the corresponding GHSV is 4000 $L/(kg_{cat}\cdot h)$.

It is worth noting that, one of the advantages of the process with a hybrid catalyst, that is, with both MeOH and DME syntheses taking place simultaneously, is that the equilibrium CO conversion is close to 100%, implying that the conversion is not limited by thermodynamic limitations. Meanwhile, in the case of two-step processes, the conversion for the MeOH reactor with the same feed composition is limited by the equilibrium conversion of lower than 100%, indicating that either the production of DME in the downstream is reduced or the additional separation process is required for the recycle of unreacted syngas.

Chapter 4 Microkietic modeling of methanol synthesis from syngas

4.1 Background

Methanol is one of the key materials produced from syngas, which contains carbon monoxide (CO), carbon dioxide (CO_2), and hydrogen (H_2), and can not only be used as a fuel or solvent by itself, but also can be converted into other useful derivatives, such as dimethyl ether (DME), methyl acetate (MA), ethanol, and acetic acid.

Kinetic studies on methanol synthesis can be divided into two main categories: lumped kinetics and microkinetics. The former usually employs a simple kinetic model representing the overall reactions and assuming a rate-determining step (RDS), while the latter considers all possible reaction pathways without assuming a particular RDS. Although most previous studies have been conducted by lumped kinetics, microkinetic studies are necessary in order to gain a fundamental understanding of the reactions and increase the system efficiency.

Studies on the production of methanol from syngas have mainly been based on catalytic reactions under gas-phase conditions, comprising CO hydrogenation, CO_2 hydrogenation, and the water–gas shift (WGS) reaction as the basic mechanisms.

Villa et al. proposed lumped kinetics for the low-pressure synthesis of methanol by CO hydrogenation and the WGS reaction over a commercial

$Cu/ZnO/Al_2O_3$ catalyst in a Berty CSTR [47]. Graaf et al. described the lumped kinetics of methanol synthesis in a low-pressure spinning basket reactor over a commercial Cu-Zn-Al catalyst at 15–50 bar and 483.15–518.15 K [32] to show that both CO and CO_2 hydrogenations are involved in the synthesis of methanol under these experimental conditions. In another of their works, the chemical equilibria of the WGS reaction were analyzed in a fixed-bed catalytic reactor in the range of 10–80 bar and 473.15–543.15 K [41], using the Soave–Redlich–Kwong equation of state, where commercial-size catalyst particles were found to exhibit limited intra-particle diffusion during methanol synthesis [48]. They also conducted experiments with two different catalyst particle sizes at 10–50 bar and 483.15–548.15 K in a spinning basket reactor and a fixed-bed catalytic reactor.

Baetzold and Somorjai calculated the pre-exponential factors for catalytic surface reactions and determined the RDS based on the calculated results [49], from which they suggested guidelines for typical pseudo first-order pre-exponential factors for various rate-limiting steps: 10^2–10^4, 10^7–10^{11}, 10–10^{13}, and 10^{13}–10^{16} s^{-1} for adsorption, diffusion, surface reaction, and desorption, respectively.

Gokhale et al. analyzed the thermochemistry and activation energy barrier of the WGS reaction mechanism on Cu (111) by DFT-generalized gradient approximation (GGA) calculations [50], and proposed that a carboxyl-mediated route replaces the redox mechanism, which is the commonly accepted mechanism. Lim et al. presented a kinetic model with different adsorption sites for CO and CO_2 for methanol synthesis over a $Cu/ZnO/Al_2O_3/ZrO_2$ catalyst to determine the appropriate RDS out of 48 combinations [40]. Grabow and Mavrikakis proposed a microkinetic model consisting of 49 elementary-step reactions [34], where the initial kinetic parameters were obtained by DFT calculations, and found that 2/3 of methanol is generated by CO_2 hydrogenation under typical industrial conditions. Ovesen et al. presented a microkinetic model for the WGS reaction based on elementary-step reactions at the atomic level, and calculated the activation energies and reaction orders [51]. Skrzypek et al. studied the low-pressure synthesis of methanol over Polish commercial catalyst CuO (60–65 wt%)–ZnO (25–35 wt%)–Al_2O_3 (remaining percentage) and described that CO_2 hydrogenation and WGS are the main reactions rather than CO hydrogenation [45]. A gas-phase thermodynamics model-based kinetic study by Askgaard et al. showed that H_2COO^* hydrogenation to methoxide over Cu (100) is the RDS, where the methanol synthesis rate obtained from the model was extrapolated to validate the industrial working conditions [52]. Bussche et al. reported a steady-state kinetic model for methanol synthesis and the WGS reaction over a Cu/ZnO/Al_2O_3 catalyst and fitted the parameters to bench-scale experimental data at 453.15–553.15 K and pressures of up to 51 bar so as to predict the conversion data and evaluate the effects of the inlet temperature, pressure, and partial pressures of CO and CO_2 [30]. Park et al. studied a kinetic model based on three-site adsorption and performed the parameter estimation using 118 experimental data under various conditions [33]. They confirmed the occurrence of both CO and CO_2 hydrogenations, whose conversion was mainly influenced by the CO and H_2 fractions. In addition, the effects of limited internal diffusion on the catalytic performance were evaluated by changing the catalyst particle size to model a pilot-scale methanol synthesis process [53]. Portha et al. investigated the kinetics of methanol synthesis by CO_2 hydrogenation on two noncommercial catalysts, a copper-zinc oxide catalyst on alumina (CuZA) and a copper-zinc oxide catalyst on zirconia (CuZZ), using Graaf's kinetic model based on the LHHW mechanism [54]. An isothermal pseudo-homogeneous PFR at 473.15–503.15 K, 50–80 bar, and 7800–23400 h^{-1} was considered in the absence of CO in the feed, in accordance with recent industrial applications.

In this chapter, a practical microkinetic modeling approach that avoids the use of computationally intensive transition state theory (TST) is presented and applied to methanol synthesis over a Cu-based catalyst. On the basis of 28 possible elementary-step reactions for CO hydrogenation, CO_2 hydrogenation, and the WGS reaction, the values of the activation energies were obtained by a combination of DFT and the UBI-QEP methods, while pre-exponential factors were estimated by fitting the experimental data [32] without theoretical calculations to reduce the computational load and increase the reliability of the model. Although theoretical computation is based on electronic structure of catalyst and interactions between electrons, ab-initio calculations is insufficient to simulate the actual experimental behaviors, probably due to the limitation on the computational burden and inappropriate assumptions. Therefore, the method suggested in the present chapter determined heat of adsorption and activation energies by the theoretical calculations under the assumption of simple structure, while pre-exponential factors were determined by fitting experimental data to ensure the reliability of the model, in such a way that the development was conducted in relatively cost-effective manner. In the reactor modeling step, the partial equilibrium ratio (PER) was calculated to reduce the stiffness of the ODEs, and a quasi-equilibrium assumption was applied to the elementary-step reactions with PER values close to 0.5. A scheme of the modeling procedure in this chapter is shown in Figure 6. Finally, the most plausible reaction pathways for CO and CO_2 hydrogenation and the rate-controlling steps were found using the developed parameter-fitted microkinetic model. In addition, several case studies were evaluated to analyze the effects of the operating conditions on the synthesis of methanol.

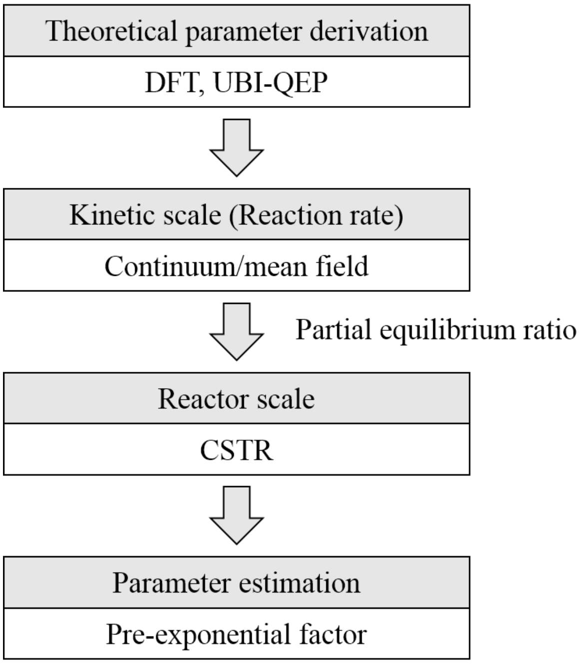

Figure 6 Scheme of the stepwise multiscale modeling procedure.

4.2 Reaction Mechanism

The reaction mechanism for methanol synthesis from syngas is basically composed of the following three overall reactions:

CO hydrogenation: $CO + 2H_2 \leftrightarrow CH_3OH$

CO_2 hydrogenation: $CO_2 + 3H_2 \leftrightarrow CH_3OH + H_2O$

WGS reaction: $H_2O + CO \leftrightarrow H_2 + CO_2$

Methanol is the only product from CO hydrogenation, while water is also produced during CO_2 hydrogenation. For the microkinetic model, elementary-step reactions for CO and CO_2 hydrogenations were defined by considering all possible reactions and surface intermediates on the basis of previously reported works [30, 52, 55-58], whose details are described in Table 6. The elementary steps included the adsorption and desorption reactions of gas-phase species, which were mostly the reactants and the products of the three overall reactions, and the surface reactions of the intermediates on the catalytic surface. Dissociation and disproportionation reactions of the small intermediates, such as CO*, CO_2*, H*, OH* and O*, were also included, and the reactions of building blocks with each other were considered to form larger intermediates such as H_2O*, HCO*, HCOO**, CH_2O*, CH_3O*, CH_3OH*, and so on. A total of 14 surface intermediates (CO*, CO_2*, H*, H_2O*, CH_2O*, CH_3OH*, O*, OH*, COOH*, HCOO**, H_2CO_2*, CH_3O*, CH_3O_2*, and HCO*) were considered to constitute the catalyst surface sites. As a result, total number of elementary steps was 28 by neglecting undetected gas phase species (CH_2O, HCOOH and $HCOOCH_3$) and the corresponding surface intermediates, while 49 steps were considered in the literature [34].

Table 6 Elementary step reactions for CO and CO_2 hydrogenations and the WGS reaction (both redox and carboxyl mechanisms [50]) considered in this work[†]

Rxn no.	Reaction	r_f	r_b
R1	CO + * ↔ CO*	$k_{\mathrm{f1}}P_{\mathrm{CO}}\theta_{Cu}$	$k_{\mathrm{b1}}\theta_{\mathrm{CO}}$
R2	CO_2 + * ↔ CO_2*	$k_{\mathrm{f2}}P_{\mathrm{CO_2}}\theta_{\mathrm{Cu}}$	$k_{\mathrm{b2}}\theta_{\mathrm{CO_2}}$
R3	H_2 + 2* ↔ 2H*	$k_{\mathrm{f3}}P_{\mathrm{H_2}}\theta_{\mathrm{Cu}}^2$	$k_{\mathrm{b3}}\theta_{\mathrm{H}}^2$
R4	H_2O + * ↔ H_2O*	$k_{\mathrm{f4}}P_{\mathrm{H_2O}}\theta_{\mathrm{Cu}}$	$k_{\mathrm{b4}}\theta_{\mathrm{H_2O}}$
R5	CH_2O + * ↔ CH_2O*	$k_{\mathrm{f5}}P_{\mathrm{CH_2O}}\theta_{\mathrm{Cu}}$	$k_{\mathrm{b5}}\theta_{\mathrm{CH_2O}}$
R6	CH_3OH + * ↔ CH_3OH*	$k_{\mathrm{f6}}P_{\mathrm{CH_3OH}}\theta_{\mathrm{Cu}}$	$k_{\mathrm{b6}}\theta_{\mathrm{CH_3OH}}$
R7	CO* + O* ↔ CO_2* + *	$k_{\mathrm{f7}}\theta_{\mathrm{CO}}\theta_{\mathrm{O}}$	$k_{\mathrm{b7}}\theta_{\mathrm{CO_2}}\theta_{\mathrm{Cu}}$
R8	CO* + OH* ↔ COOH* + *	$k_{\mathrm{f8}}\theta_{\mathrm{CO}}\theta_{\mathrm{OH}}$	$k_{\mathrm{b8}}\theta_{\mathrm{COOH}}\theta_{\mathrm{Cu}}$
R9	CO_2* + H* ↔ COOH* + *	$k_{\mathrm{f9}}\theta_{\mathrm{CO_2}}\theta_{\mathrm{H}}$	$k_{\mathrm{b9}}\theta_{\mathrm{COOH}}\theta_{\mathrm{Cu}}$
R10	CO_2* + H_2O* ↔ COOH* + OH*	$k_{\mathrm{f10}}\theta_{\mathrm{CO_2}}\theta_{\mathrm{H_2O}}$	$k_{\mathrm{b10}}\theta_{\mathrm{COOH}}\theta_{\mathrm{OH}}$
R11	H_2O* + * ↔ OH* + H*	$k_{\mathrm{f11}}\theta_{\mathrm{H_2O}}\theta_{\mathrm{Cu}}$	$k_{\mathrm{b11}}\theta_{\mathrm{OH}}\theta_{\mathrm{H}}$
R12	OH* + * ↔ O* + H*	$k_{\mathrm{f12}}\theta_{\mathrm{OH}}\theta_{\mathrm{Cu}}$	$k_{\mathrm{b12}}\theta_{\mathrm{O}}\theta_{\mathrm{H}}$
R13	2OH* + * ↔ H_2O* + H*	$k_{\mathrm{f13}}\theta_{\mathrm{OH}}^2$	$k_{\mathrm{b13}}\theta_{\mathrm{H_2O}}\theta_{\mathrm{H}}$
R14	CO_2* + H* ↔ HCOO**	$k_{\mathrm{f14}}\theta_{\mathrm{CO_2}}\theta_{\mathrm{H}}$	$k_{\mathrm{b14}}\theta_{\mathrm{HCOO}}$
R15	HCOO** + H* ↔ H_2CO_2* + 2*	$k_{\mathrm{f15}}\theta_{\mathrm{HCOO}}\theta_{\mathrm{H}}$	$k_{\mathrm{b15}}\theta_{\mathrm{H_2CO_2}}\theta_{\mathrm{Cu}}^2$
R16	H_2CO_2* + H* ↔ CH_3O_2* + *	$k_{\mathrm{f16}}\theta_{\mathrm{H_2CO_2}}\theta_{\mathrm{H}}$	$k_{\mathrm{b16}}\theta_{\mathrm{CH_3O_2}}\theta_{\mathrm{Cu}}$
R17	H_2CO_2* + * ↔ CH_2O* + O*	$k_{\mathrm{f17}}\theta_{\mathrm{H_2CO_2}}\theta_{\mathrm{Cu}}$	$k_{\mathrm{b17}}\theta_{\mathrm{CH_2O}}\theta_{\mathrm{O}}$
R18	CH_3O_2* + * ↔ CH_2O* + OH*	$k_{\mathrm{f18}}\theta_{\mathrm{H_2CO_2}}\theta_{\mathrm{Cu}}$	$k_{b18}\theta_{CH_2O}\theta_{O}$
R19	CH_2O* + H* ↔ CH_3O* + *	$k_{\mathrm{f19}}\theta_{\mathrm{CH_2O}}\theta_{\mathrm{H}}$	$k_{\mathrm{b19}}\theta_{\mathrm{CH_3O}}\theta_{\mathrm{Cu}}$

R20	$CH_3O^* + H^* \leftrightarrow CH_3OH^* + {}^*$	$k_{\mathrm{f20}}\theta_{\mathrm{CH_3O}}\theta_{\mathrm{H}}$	$k_{\mathrm{b20}}\theta_{\mathrm{CH_3OH}}\theta_{\mathrm{Cu}}$
R21	$CO^* + H^* \leftrightarrow HCO + {}^*$	$k_{\mathrm{f21}}\theta_{\mathrm{CO}}\theta_{\mathrm{H}}$	$k_{\mathrm{b21}}\theta_{\mathrm{HCO}}\theta_{\mathrm{Cu}}$
R22	$HCOO^{**} \leftrightarrow HCO^* + O^*$	$k_{\mathrm{f22}}\theta_{\mathrm{HCOO}}$	$k_{\mathrm{b22}}\theta_{\mathrm{HCO}}\theta_{\mathrm{O}}$
R23	$HCO^* + H^* \leftrightarrow CH_2O^* + {}^*$	$k_{\mathrm{f23}}\theta_{\mathrm{HCO}}\theta_{\mathrm{H}}$	$k_{\mathrm{b23}}\theta_{\mathrm{CH_2O}}\theta_{\mathrm{Cu}}$
R24	$CO^* + OH^* \leftrightarrow HCO^* + O^*$	$k_{\mathrm{f24}}\theta_{\mathrm{CO}}\theta_{\mathrm{OH}}$	$k_{\mathrm{b24}}\theta_{\mathrm{HCO}}\theta_{\mathrm{O}}$
R25	$CO^* + H_2O^* \leftrightarrow HCO^* + OH^*$	$k_{\mathrm{f25}}\theta_{\mathrm{CO}}\theta_{\mathrm{H_2O}}$	$k_{\mathrm{b25}}\theta_{\mathrm{HCO}}\theta_{\mathrm{OH}}$
R26	$CH_3O^* + CO^* \leftrightarrow CH_2O^* + HCO^*$	$k_{\mathrm{f26}}\theta_{\mathrm{CH_3O}}\theta_{\mathrm{CO}}$	$k_{\mathrm{b26}}\theta_{\mathrm{CH_2O}}\theta_{\mathrm{HCO}}$
R27	$CH_3O^* + HCO^* \leftrightarrow CH_3OH^* + CO^*$	$k_{\mathrm{f27}}\theta_{\mathrm{CH_3O}}\theta_{\mathrm{HCO}}$	$k_{\mathrm{b27}}\theta_{\mathrm{CH_3OH}}\theta_{\mathrm{CO}}$
R28	$CH_3O_2^* + H^* \leftrightarrow CH_2O^* + H_2O^*$	$k_{\mathrm{f28}}\theta_{\mathrm{CH_3O_2}}\theta_{\mathrm{H}}$	$k_{\mathrm{b28}}\theta_{\mathrm{CH_2O}}\theta_{\mathrm{H_2O}}$

[†] Symbol * represents vacant sites and HCOO** refers to bidentate species, while r_{f} and r_{b} denote the forward and backward reaction rates, respectively.

4.3 Methods

For kinetic modeling of all 28 elementary-step reactions, all the kinetic parameters for the forward and backward reactions were calculated using the Arrhenius equation. The initial value of the pre-exponential factor was derived from the order-of-magnitude based on TST, under the assumption that the values of the pre-exponential factor for immobile transition states, molecular adsorption, and dissociative adsorption are of the order of 10^1 Pa^{-1} s^{-1}, while those for the molecular desorption and associative desorption are of the order of 10^{13} s^{-1}. The Langmuir–Hinshelwood surface reaction has an order of 10^{13} s^{-1} in the absence of rotation [11].

4.3.1 Activation Energy

In order to calculate the activation energies, the enthalpies and adsorption energies of gas and surface intermediates were calculated by the first-principles DFT method and then, those values were applied to the UBI-QEP [16]. The software Vienna Ab-Initio Simulation Package (VASP) was used for DFT calculations in the present chapter [22, 59, 60].

For gas-phase species, DFT calculations were carried out in an isolated system not affected by periodic boundary conditions. Spin-polarized calculations were performed for atom species such as H and O, while non-spin-polarized calculations were used for the remaining species [61].

Copper nanoparticles exist in several forms on the surface of $Cu/ZnO/Al_2O_3$ catalyst, including metallic surfaces such as Cu (111), Cu (100) and Cu (200), partially oxidized Cu surfaces such as Cu_2O and CuO, and defective sites. Cu can also interact with ZnO support affecting the reaction activities [62]. In addition, the stepped and defective sites on Cu surface affect the adsorption of intermediates and reaction activities in methanol synthesis. For example, CO_2 dissociation takes place preferentially on the stepped and defective sites, resulting in the high selectivity for methanol synthesis [63]. Strong adsorption of the intermediates on the stepped sites, which are stabilized by defects like stacking faults, and lower activation barriers also cause high activity [64]. However, since it was reported that the oxide support has no significant effects on the activity of Cu in methanol synthesis due to highly reduced conditions [65], the pure metallic Cu surface was used in DFT calculations. Since Cu (111) and Cu (100) surfaces are one of the most frequently observed surfaces at low pressures [66] and polycrystalline Cu exposes primarily a Cu (111) surface [67], DFT calculations were performed on Cu (111) surface. Having cubic structure and space group of *Fm-3m*, unit cell optimization was performed to create a Cu (111) surface slab model, as shown in Figure 7, with a lattice constant of 3.66 Å (cf., the experimental value is 3.62 Å) [23]. The slab model consisted of three layers of Cu (111) surfaces under the assumption of negligible surface relaxation effects and vacuum of 10.6 Å to minimize the effects of periodic boundary conditions [50, 68, 69]. It is worth noting that, although there are many possible oxidation states Cu in contact with ZnO such as Cu^0, Cu^+ and Cu^{2+} [70, 71], this feature was not considered in the present work due to the assumption of pure metallic Cu on the catalyst surface.

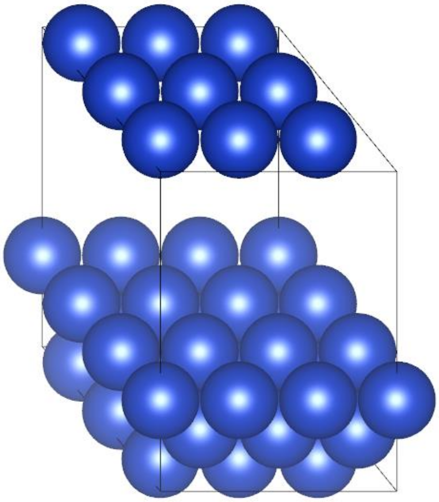

Figure 7 Cu (111) slab model.

Using a primitive (3 × 3) model, all the materials had a coverage of 1/9 of the monolayer. The total energies of the adsorbed materials were calculated on a 5 × 5 × 1 k-point monkhorst-packed grid, and the Perdew–Wang 91 GGA (GGA-PW91) was used as the functional. The calculations were performed under a non-spin-polarized environment, and the plane-wave cut-off was set to 530 eV to prevent Pulay stresses [72].

The adsorption energies (Q_{ads}) were calculated using the following equation:

$$Q_{\mathrm{ads}} = |E_{\mathrm{ads}}| = |E_{\mathrm{total}} - E_{\mathrm{clean}} - E_{\mathrm{gas}}| \tag{4.1}$$

where E_{total}, E_{clean}, and E_{gas} represent the total energy of the surface with surface intermediates, the bare surface, and the adsorbed species in gas-phase, respectively. A negative value of E_{ads} corresponds to an exothermic adsorption reaction, while a positive value denotes endothermic adsorption. The enthalpy of the reaction (ΔH_{rxn}) is defined as follows:

For dissociative adsorption:

$$\Delta H_{\mathrm{rxn}} = D_{\mathrm{AB}} - Q_{\mathrm{A}} - Q_{\mathrm{B}} \text{ with } D_{\mathrm{AB}} = H_{\mathrm{A}} + H_{\mathrm{B}} - H_{\mathrm{AB}} \tag{4.2}$$

For the dissociation reaction:

$$\Delta H_{\mathrm{rxn}} = D_{\mathrm{AB}} + Q_{\mathrm{AB}} - Q_{\mathrm{A}} - Q_{\mathrm{B}} \text{ with } D_{\mathrm{AB}} = H_{\mathrm{A}} + H_{\mathrm{B}} - H_{\mathrm{AB}} \tag{4.3}$$

For the disproportionation reaction:

$$\Delta H_{\mathrm{rxn}} = D_{\mathrm{AB}} + Q_{\mathrm{A}} + Q_{\mathrm{B}} - Q_{\mathrm{C}} - Q_{\mathrm{D}} \text{ with } D_{\mathrm{AB}} = H_{\mathrm{C}} + H_{\mathrm{D}} - H_{\mathrm{A}} - H_{\mathrm{B}} \quad (4.4)$$

where the gas-phase dissociation energy D and gas-phase enthalpy H were calculated by the DFT method.

Only E_{f} was calculated by the UBI-QEP method, while E_{b} was calculated by the following equation:

$$E_{\mathrm{b}} = E_{\mathrm{f}} - \Delta H_{\mathrm{rxn}} \quad (4.5)$$

If either E_{f} or E_{b} became negative during the calculation process, it was set to zero and the other energy replaced with the absolute value of the enthalpy of reaction.

4.3.2 Microkinetic Model

As mentioned earlier, a microkinetic model is difficult to solve with a general ODE solver because many reactions are included in the model and they are strongly correlated. In order to solve this problem, model reduction was conducted in such a way that the elementary-step reactions, which are close to the quasi-equilibrium, were assumed to have little influence on the reaction kinetics and the corresponding mechanisms were excluded [1].

First, steady-state solutions were obtained at three different temperatures of 483.5, 499.3, and 516.7 K, and a partial equilibrium analysis was performed to exclude the reactions that barely influence the reaction kinetics. The partial equilibrium ratio (φ) was defined by the following equation:

$$\varphi = \frac{r_\mathrm{f}}{r_\mathrm{f}+r_\mathrm{b}} \tag{4.6}$$

An elementary surface reaction can be assumed to be quasi-equilibrated if φ is close to 0.5 (i.e., the rates of the forward and backward reactions are similar). The kinetic parameters of the remaining elementary-step reactions were fitted to the experimental values of the H_2O and CH_3OH outlet compositions at the three temperatures. Meanwhile, the adsorption and desorption reactions of gaseous species (CO (g), CO_2 (g), H_2 (g), H_2O (g), and CH_3OH (g)) were assumed to be in quasi-equilibrium, with the exception of CH_2O (g) desorption that was assumed to be negligible because it is not a product experimentally observed.

For gas-phase species, the following equations were developed by applying the equilibrium relations of adsorption and desorption reactions:

$$K_\mathrm{CO} = \frac{k_\mathrm{ads,CO}}{k_\mathrm{des,CO}} = a(\mathrm{CO})\exp\left(\frac{b(\mathrm{CO})}{RT}\right) = \frac{\theta_\mathrm{CO}}{P_\mathrm{CO}\theta_\mathrm{Cu}} \tag{4.7}$$

$$K_\mathrm{CO_2} = \frac{k_\mathrm{ads,CO_2}}{k_\mathrm{des,CO_2}} = a(\mathrm{CO_2})\exp\left(\frac{b(\mathrm{CO_2})}{RT}\right) = \frac{\theta_\mathrm{CO_2}}{P_\mathrm{CO_2}\theta_\mathrm{Cu}} \tag{4.8}$$

$$K_\mathrm{H_2} = \frac{k_\mathrm{ads,H_2}}{k_\mathrm{des,H_2}} = a(\mathrm{H_2})\exp\left(\frac{b(\mathrm{H_2})}{RT}\right) = \frac{\theta_\mathrm{H}^2}{P_\mathrm{H_2}\theta_\mathrm{Cu}^2} \tag{4.9}$$

$$K_{\mathrm{H_2O}} = \frac{k_{\mathrm{ads,H_2O}}}{k_{\mathrm{des,H_2O}}} = a(\mathrm{H_2O})\exp\left(\frac{b(\mathrm{H_2O})}{RT}\right) = \frac{\theta_{\mathrm{H_2O}}}{P_{\mathrm{H_2O}}\theta_{\mathrm{Cu}}} \tag{4.10}$$

$$K_{\mathrm{CH_3OH}} = a(\mathrm{CH_3OH})\exp\left(\frac{b(\mathrm{CH_3OH})}{RT}\right) = \frac{k_{\mathrm{ads,CH_3OH}}}{k_{\mathrm{des,CH_3OH}}} = \frac{\theta_{\mathrm{CH_3OH}}}{P_{\mathrm{CH_3OH}}\theta_{\mathrm{Cu}}} \tag{4.11}$$

where K_{i}, $k_{\mathrm{ads,i}}$, $k_{\mathrm{des,i}}$, and P_{i} represent the adsorption equilibrium constant, adsorption rate constant, desorption rate constant, and partial pressure, respectively, for gas-phase species i, while θ_{j} denotes the coverage (site fraction) of surface intermediate j (cf., θ_{Cu} is the fraction of vacant sites). Symbols $a(i)$ and $b(i)$ are derived from the Arrhenius equations for the adsorption and desorption rate constants. The coverages of the adsorbed components of the feed (CO*, CO_2*, and H*) were determined as follows:

$$\theta_{\mathrm{CO}} = K_{\mathrm{CO}}P_{\mathrm{CO}}\theta_{\mathrm{Cu}} \tag{4.12}$$

$$\theta_{\mathrm{CO_2}} = K_{\mathrm{CO_2}}P_{\mathrm{CO_2}}\theta_{\mathrm{Cu}} \tag{4.13}$$

$$\theta_{\mathrm{H}} = \left(\sqrt{K_{\mathrm{H_2}}P_{\mathrm{H_2}}}\right)\theta_{\mathrm{Cu}} \tag{4.14}$$

The partial pressures of the main products (H_2O and CH_3OH) were derived by calculating the coverage of H_2O* and CH_3OH*, as follows:

$$P_{\mathrm{H_2O}} = \frac{\theta_{\mathrm{H_2O}}}{K_{\mathrm{H_2O}}\theta_{\mathrm{Cu}}} \tag{4.15}$$

$$P_{\mathrm{CH_3OH}} = \frac{\theta_{\mathrm{CH_3OH}}}{K_{\mathrm{CH_3OH}}\theta_{\mathrm{Cu}}} \tag{4.16}$$

Since a previous study showed that the most abundant surface intermediates on Cu (111) were free sites and hydrogen (H*) as a result of the calculation [52], those species were considered in the site balance equation, while H_2O and CH_3OH were assumed to desorb rapidly. The coverage of vacant sites was derived by considering the species significantly related to the production of CH_3OH [32, 33] and applying Equations (4.12)–(4.14), as follows:

$$1 = \theta_{\mathrm{Cu}} + \theta_{\mathrm{CO}} + \theta_{\mathrm{CO_2}} + \theta_{\mathrm{H}} \tag{4.17}$$

$$1 = \theta_{\mathrm{Cu}} + K_{\mathrm{CO}}P_{\mathrm{CO}}\theta_{\mathrm{Cu}} + K_{\mathrm{CO_2}}P_{\mathrm{CO_2}}\theta_{\mathrm{Cu}} + \left(\sqrt{K_{\mathrm{H_2}}P_{\mathrm{H_2}}}\right)\theta_{\mathrm{Cu}} \tag{4.18}$$

$$\theta_{\mathrm{Cu}} = \frac{1}{1+K_{\mathrm{CO}}P_{\mathrm{CO}}+K_{\mathrm{CO_2}}P_{\mathrm{CO_2}}+\sqrt{K_{\mathrm{H_2}}P_{\mathrm{H_2}}}} \tag{4.19}$$

The remaining reaction kinetic equations were solved by a stiff ODE solver (ode15s) in MATLAB (MathWorks, Inc.), where the backward differentiation formula (BDF) algorithm was used to solve the following ODEs efficiently. The coverages of surface intermediates except CO*, CO_2*, and H*, which were already included in the reaction rates, were determined by solving the balance equations until steady states were reached. Detailed differential equations for the balances of surface intermediates can be referred to the Supporting Information in Appendix (Equations (S1)–(S11)).

Experimental data for a spinning basket reactor reported by Graaf et al. [32, 73] were used to conduct kinetic parameter estimations, and a CSTR was used as the reactor model in this work. A spinning basket reactor has several advantages: Ease of construction and maintenance, perfect mixing of the bulk gas, and great heat and mass transfer between the bulk gas and the external surface of the catalyst [74]. In the experiments, kinetic data were obtained over a commercial $Cu/ZnO/Al_2O_3$ catalyst (Haldor Topsoe Mk 101) at 15–50 bar and 483–518 K by varying feed flow rates and compositions of CO, CO_2 and H_2. The catalyst particles were kept in four baskets attached on a common stirrer shaft of the reactor. The compositions of gas species except for hydrogen at the outlet were measured by a gas-liquid chromatography, while the composition of hydrogen was determined from material balances. On the basis of experimental observation that the methanol synthesis rates did not change with the variation of the stirrer speed from 8.3 to 33 s^{-1} and reported calculations, the experimental conditions were assumed to be under the reaction kinetics regime, with no mass transfer limitation. However, some experimental data were ignored in this work because intra-particle diffusion limitations were observed at temperatures above 518 K, as noted by Askgaard et al. [52].

The exit gas consisted of reactants (CO, CO_2, and H_2), products (H_2O and CH_3OH), and byproducts (CH_3OCH_3 (DME), CH_4, C_2H_6, and C_3H_8), as per the report by Graaf et al. However, since the sum of compositions for the byproducts was below 0.0001 in the experimental data, the corresponding elementary steps were ignored. In addition, the data presenting relative errors above 40% in the material balance according to Askgaard et al.'s criterion were considered to be obtained at non-steady-state and were thus excluded. The site density of the copper catalyst was specified to be 300 μmol g^{-1} [75].

The parameter estimation was conducted for 41 parameters, including five adsorption and desorption equilibrium constants and 36 pre-exponential factors (18 for each forward and backward reaction), with all activation energies fixed. For the adsorption and desorption equilibrium constants, $b(i)$ were fixed with the values obtained from the DFT calculations, and only $a(i)$ were estimated with initial values specified at 10^{-12} Pa^{-1} s^{-1} from the order-of-magnitude of TST. In the case of surface reactions, the pre-exponential factors have been reported to vary from 10^1 to 10^{22} s^{-1} [49, 56], and thus, those values were specified as the lower and upper bounds for the parameters.

The genetic algorithm (GA), which is a useful optimization technique to search for optimal points by randomly scattering population seeds when the search space is large, was used to estimate the parameters globally. The following objective function, based on the relative error sum of squares (ESS) between the experimental and calculated values of the CH_3OH and H_2O production rates, was used to fit the experimental data. From the perspective of overall mass balance, the consumption rates of H_2, CO and CO_2 are reflected in the production rate of methanol and water. Therefore, because of highly correlated characteristics of the species, the production rates of methanol and water were only included in the objective function.

$$F_{\mathrm{obj}} = \sum_i^N \left[\left(\frac{r_{\mathrm{CH_3OH,exp}} - r_{\mathrm{CH_3OH,calc}}}{r_{\mathrm{CH_3OH,exp}}} \right)^2 + WF \left(\frac{r_{\mathrm{H_2O,exp}} - r_{\mathrm{H_2O,calc}}}{r_{\mathrm{H_2O,exp}}} \right)^2 \right]_i \quad (4.20)$$

where N denotes the number of experimental conditions considered, and WF is a weighting factor. When WF was set to 0, parameter fitting was performed only for CH_3OH, while an infinite value of WF corresponded to the estimation only for H_2O. Likewise, at $WF = 1$, CH_3OH and H_2O were considered equally. In this work, equal weight was given to both quantities.

4.4 Application Results and Discussion

4.4.1 DFT Calculations

The adsorption energies and most stable adsorption states of all the surface intermediates under 1/9 monolayer conditions involved in the elementary-step reactions were determined, as summarized in Table 7. These results are in good agreement with the findings of previous research works [34]. It is worth noting that the adsorption energy of CO (-0.71 eV) is much lower than that of H* (-2.40 eV). This feature is attributable that, since CO is more stable than H* in gas-phase, less adsorption energy is released when CO is adsorbed on Cu surface. Meanwhile, highly unstable state of H* in gas-phase leads to much higher adsorption energy of H (-2.40 eV) than that of CO (-0.71 eV).

Table 7 Most stable adsorption sites and adsorption energies of all the surface intermediates

Surface intermediate	Adsorption site	Adsorption energy [eV]
CO^*	fcc	-0.71
CO_2^*	physisorbed	-0.04
H^*	fcc	-2.40
H_2O^*	top	-0.18
CH_3OH^*	O-top	-0.19
O^*	fcc	-4.89
OH^*	fcc	-3.13
HCO^*	bridge	-1.23
$HCOO^{**}$	top-top	-2.75
$H_2CO_2^*$	bridge-bridge	-3.81
$COOH^*$	top	-1.56
CH_2O^*	C-top/O-bridge	-0.06
CH_3O^*	fcc	-2.26
$CH_3O_2^*$	O-bridge/O-top	-2.20

Since formate (HCOO**), which can be generated in the WGS reaction, has been reported to play an important role in methanol synthesis [76-81] and its coverage is known to be proportional to the turnover frequency of methanol in the Zn/Cu (111) catalyst model [82], the adsorption state of the molecule was assumed to significantly affect the overall reaction rates. It has been reported in previous studies [34, 83-85] that formate adsorbs in a bidentate fashion on the Cu (111) surface, as observed in the DFT calculations (Figure 8). This behavior is in fact reflected in the equations of the microkinetic model, while most reported works have considered a first-order dependence of the vacant sites (θ_{Cu}).

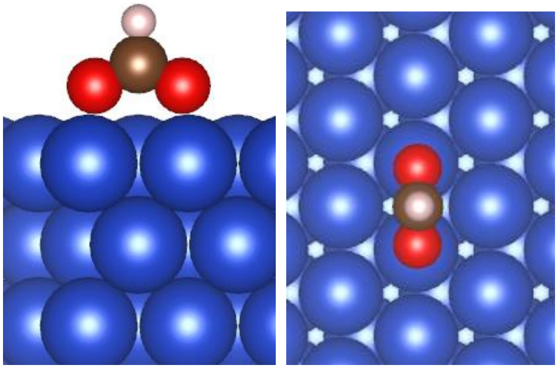

Figure 8 Most stable state of HCOO** calculated by the DFT method (bidentate form).

4.4.2 Microkinetic Model

In this work, microkinetic model was developed under the experimental operating conditions: pressure of 15, 30, and 50 bar; temperature of 483.5, 499.3, and 516.7 K; gas flow rates per catalyst weight of 0.001–0.006 $m^3\ s^{-1}\ kg^{-1}$ at the standard temperature and pressure. The catalyst weight was 4.24 g and the feed compositions were 0.053/0.047/0.900, 0.120/0.021/0.859, 0.179/0.067/0.754 for $CO/CO_2/H_2$. The partial equilibrium ratios were calculated for each elementary-step reaction to alleviate the stiffness of the ODEs, and the results are shown in Figure 9 on the basis of steady-state solutions under three different temperature conditions.

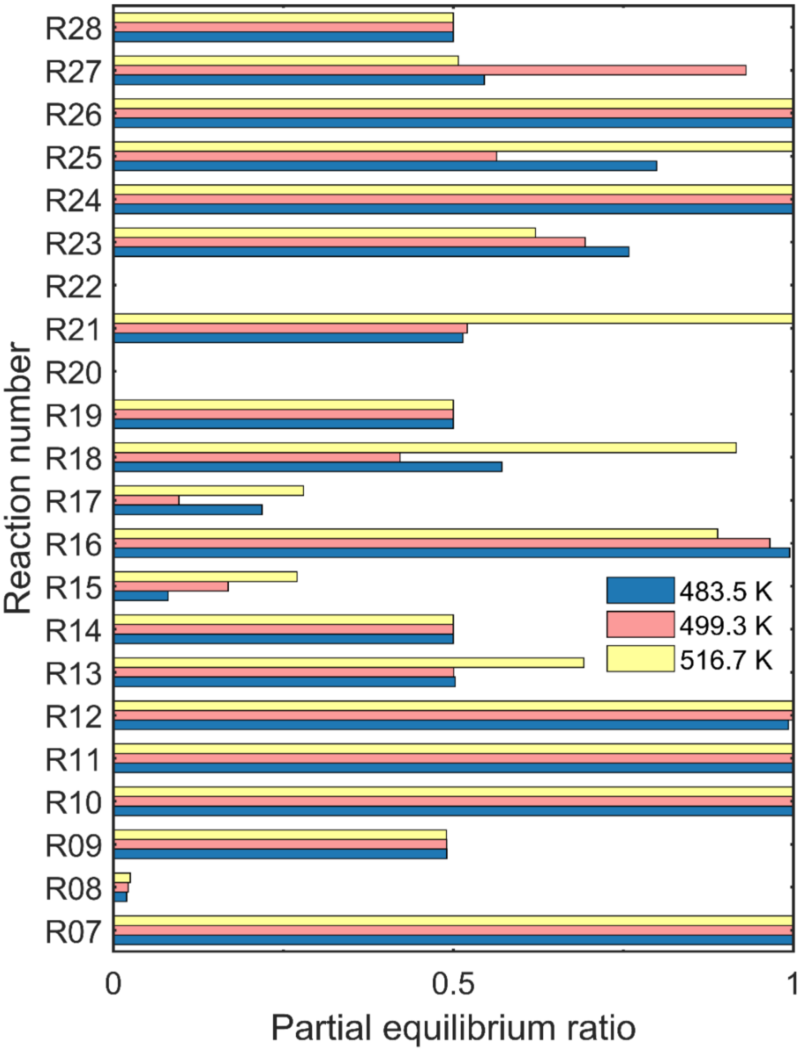

Figure 9 Partial equilibrium ratios for the surface reactions at three different temperatures.

Since the partial equilibrium ratios of R9, R14, R19, and R28 are close to 0.5, those four reactions can be assumed to be quasi-equilibrated and were thus excluded from the set of reaction rates.

The estimated data are shown in the parity plot (Figure 10), where a log–log scale was applied to consider different orders of experimental data. The experimental data were well reproduced with R^2 values of 0.90 and 0.99 for the CH_3OH and H_2O synthesis rates, respectively ($R^2 = 0.94$ overall).

The estimated parameters are shown in Table 8 with the reaction enthalpies and activation energies obtained from DFT and UBI-QEP calculations, respectively. After assuming the quasi-equilibrium on the several elementary steps and performing parameter estimation, the ODE solving failure caused by stiffness did not occur when conducting analysis on the reaction mechanisms and case studies.

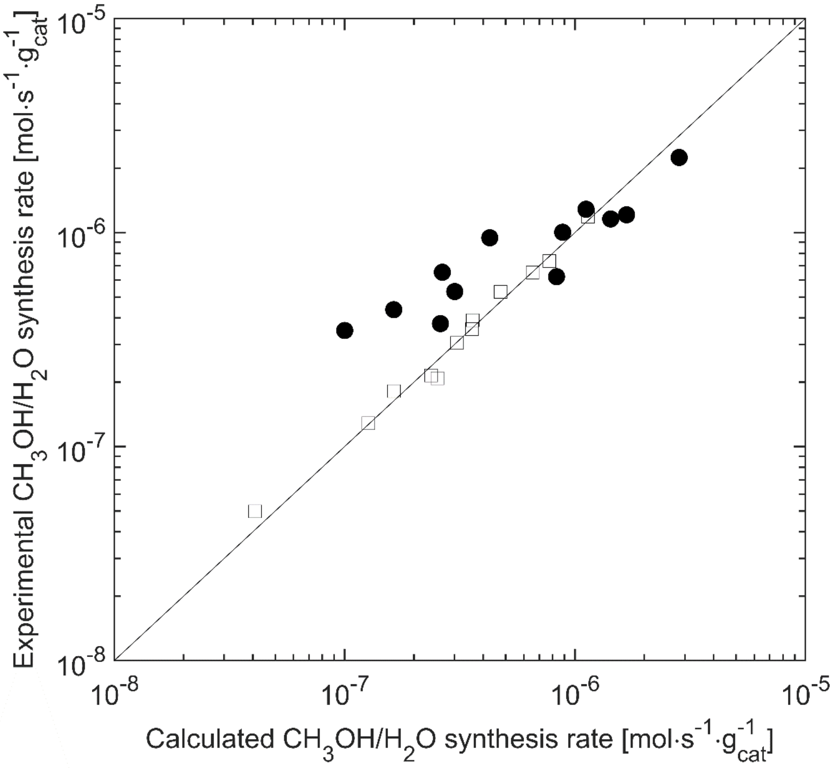

Figure 10 Experimental and calculated CH_3OH/H_2O synthesis rates (● CH_3OH, □ H_2O).

Table 8 Estimated parameters for adsorption/desorption reactions and surface reactions

Reaction	$a(i)$ [Pa^{-1} s^{-1}]	ΔH [eV]	Bond index	E_f [eV]
R1	2.55E-20	-0.71	-	-
R2	1.75E-18	-0.04	-	-
R3	1.73E-09	-0.27	-	-
R4	1.31E-17	-0.18	-	-
R5	-	-0.06	-	-
R6	5.51E-21	-0.19	-	-

	A_f [s^{-1}]	A_b [s^{-1}]	ΔH [eV]	Bond index	E_f [eV]
R7	3.83E+16	6.98E+17	-1.08	0.95	0.53
R8	1.00E+20	1.28E+06	0.16	0.5	0.37
R10	1.00E+18	1.65E+06	0.78	0.5	0.78
R11	6.07E+11	2.83E+14	0.26	0.5	0.81
R12	8.78E+17	1.42E+07	0.72	0.5	1.17
R13	1.57E+11	2.66E+14	0.47	0.95	0.61
R15	3.17E+18	4.32E+16	0.89	0.5	1.09
R16	1.94E+17	8.40E+19	-0.61	0.6	0.64
R17	1.18E+17	1.47E+13	0.76	0.5	0.76
R18	7.67E+12	1.38E+14	0.65	0.5	0.65
R20	1.94E+11	1.01E+05	-0.23	0.95	1.09
R21	5.16E+07	1.28E+09	0.72	0.5	0.72

R22	1.97E+14	9.31E+17	2.08	0.5	2.08
R23	4.31E+13	1.72E+11	-0.43	0.5	0.19
R24	8.15E+12	1.78E+19	1.45	0.5	1.45
R25	2.08E+19	1.01E+13	0.98	0.5	0.98
R26	1.00E+22	1.00E+14	1.70	0.5	1.70
R27	1.31E+02	8.20E+20	-0.96	0.5	0

The relative reaction rates of each elementary-step reactions were compared using the parameter-fitted microkinetic model developed in this chapter to show that the most plausible path for CO hydrogenation is CO (g) → CO* → HCO* → CH_2O* → CH_3O* → CH_3OH* → CH_3OH (g), while CO_2 is most likely hydrogenated via CO_2 (g) → CO_2* → HCOO** → H_2CO_2* → CH_3O_2* → CH_2O* → CH_3O* → CH_3OH* → CH_3OH (g). These reactions were approximately 2–3 orders of magnitude faster than the other competitive reactions. In the case of CO hydrogenation, CO (g) in the gas-phase is adsorbed on the catalyst surface (CO*) and sequentially reacts with H* to form CH_3OH*, followed by its desorption. In the case of CO_2 hydrogenation, CO_2* reacts sequentially with H* to form CH_3O_2*. Then, CH_3O_2* reacts with H* and is decomposed into CH_2O* and H_2O* via a disproportionation reaction (R28). Finally, CH_2O* reacts in the same way as in CO hydrogenation to produce CH_3OH*. Figure 11 (a) and (b) shows the most plausible pathways for CO and CO_2 hydrogenation, respectively, along with the energy levels estimated by the DFT calculations and the adsorption images of the involved surface intermediates. It is worth noting that, although step reactions R14, R19, and R28 were found to be quasi-equilibrated and thus excluded from the kinetic analysis, they were included in the pathways to compensate for the missing steps and were assumed to rapidly reach the quasi-equilibrium.

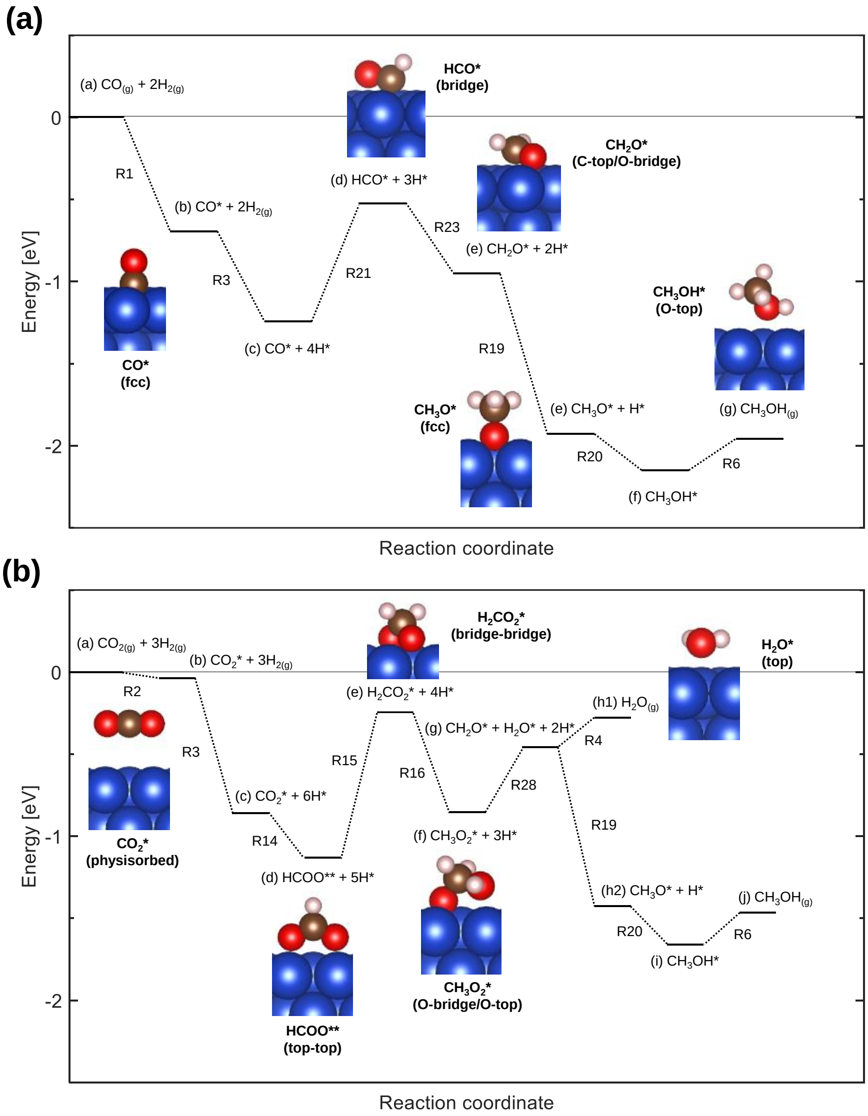

Figure 11 Most plausible reaction pathways for **(a)** CO and **(b)** CO_2 hydrogenation.

Figure 12 shows the surface coverage of the most abundant surface intermediates as a function of the pressure from 1 to 100 bar at the fixed temperature of 510 K, where those with a coverage below 10^{-5} were excluded from the figure. The catalyst surface was mainly covered by H* and vacant sites under the operating conditions, which is consistent with reported results[52]. As seen in Figure 12 (a) and (b), at a constant feed ratio, the coverage of H* increased with an increase in pressure, while that of the vacant sites decreased.

Comparison of Figure 12 (a) and (b) revealed the effects of the fraction of H_2 (g) on the surface coverage of H*; the smaller the fraction of H_2 (g), the smaller the coverage of H* at the same pressure. Meanwhile, the CO* and CO_2* coverages were found to be little influenced by the fractions of CO (g) and CO_2 (g).

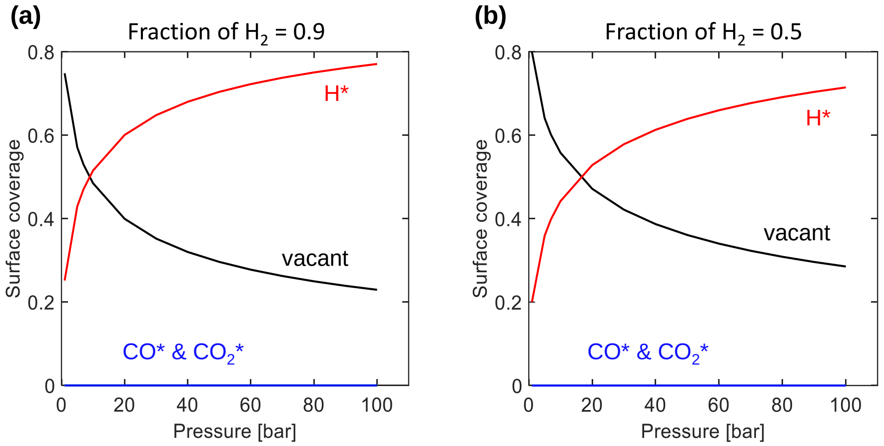

Figure 12 Plots of surface coverage as a function of the total pressure at H_2 fractions of **(a)** 0.9 and **(b)** 0.5**.**

4.4.3 Rate-Determining Step

The rate-controlling steps were identified using Campbell's degree of rate control [20, 86-88]. The sensitivity of each elementary-step reaction on the overall methanol synthesis rate was analyzed. The degree of rate control of the n-th elementary step, $X_{\mathrm{RC,n}}$, is given by:

$$X_{\mathrm{RC,n}} = \frac{k_{\mathrm{n}}}{r_{\mathrm{CH_3OH}}}\left(\frac{\partial r_{\mathrm{CH_3OH}}}{\partial k_{\mathrm{n}}}\right)_{K_{\mathrm{n,eq}},k_{\mathrm{m\neq n}}} \tag{4.21}$$

where $r_{\mathrm{CH_3OH}}$ is the reaction rate of methanol synthesis and k_{n} is the rate constant of the n-th step reaction to be varied, while the equilibrium constant of the n-th step reaction and the other reaction rate constants are held constant. The temperature and pressure were fixed at 500 K and 15 bar, respectively. The degree was calculated at three different feed compositions: (1) 5.3 mol% CO, 4.7 mol% CO_2, and 90 mol% H_2; (2) 12 mol% CO, 2.1 mol% CO_2, and 85.9 mol% H_2; and (3) 17.9 mol% CO, 6.7 mol% CO_2, and 75.4 mol% H_2.

Based on the degree of rate control, four steps were determined to be rate-controlling: R7 ($CO^* + O^* \leftrightarrow CO_2^* + *$), R20 ($CH_3O^* + H^* \leftrightarrow CH_3OH^* + *$), R24 ($CO^* + OH^* \leftrightarrow HCO^* + O^*$), and R26 ($CH_3O^* + CO^* \leftrightarrow CH_2O^* + HCO^*$), of which R20 is the only step included in the most plausible reaction pathways for CO and CO_2 hydrogenation (cf., Figure 11).

Graaf's group showed that R19 ($CH_2O^* + H^* \leftrightarrow CH_3O^* + {}^*$) and R16 ($H_2CO_2^* + H^* \leftrightarrow CH_3O_2^* + {}^*$) are the RDSs for CO and CO_2 hydrogenation, respectively [32], while the surface reaction of methoxy species H_3CO^* and H^* (R20) [40, 79] and the hydrogenation of formate intermediate HCOO** (R15) [40, 89] have been reported to determine the overall rate, respectively. In the microkinetic model, R20 was determined as the common RDS for CO and CO_2 hydrogenation, as discussed above. In addition, the activation energy calculations showed that R20 presents a higher activation energy (1.09 eV) than R16 (0.64 eV) and R19 (0.01 eV). Compared to the reported RDS [40, 89], the hydrogenation of formate intermediate HCOO** (R15) was not included in the RDS. Since the bidentate species of the formate intermediate (HCOO**) covered larger surface than a monodentate species and collided with hydrogen intermediate more easily, the hydrogenation of formate intermediate (R15) might be faster and this reaction step was not considered as a RDS.

4.4.4 Effects of Operating Conditions

The effects of the temperature, pressure, and relative amount of H_2 (g) on the methanol synthesis rate were evaluated. High pressures result in high rates due to the increased concentration of gaseous reactants, while high temperatures induce high rates by increasing the overall reaction rates (Figure 13 (a)) as the reaction remains in the kinetic regime.

The effects of the relative amount of H_2 (g) on the methanol synthesis rate are shown in Figure 13 (b). As the stoichiometric ratio of H_2, defined as

$H_2/(2CO + 3CO_2)$, was increased from 0.2 to approximately 1, the synthesis rate increased, and further increases of the ratio led to a decay of the methanol synthesis rate due to the lack of carbon sources. Consequently, this suggests that the optimum feed ratio should be maintained close to the stoichiometry to maximize the methanol synthesis rate. Since the optimum ratio is not exactly unity owing to the occurrence of the WGS reaction and is also dependent on the temperature, as shown in Figure 13 (b) (cf., the arrows denote the optimal ratio as a function of the temperature), an optimization procedure may be required at this stage of process development.

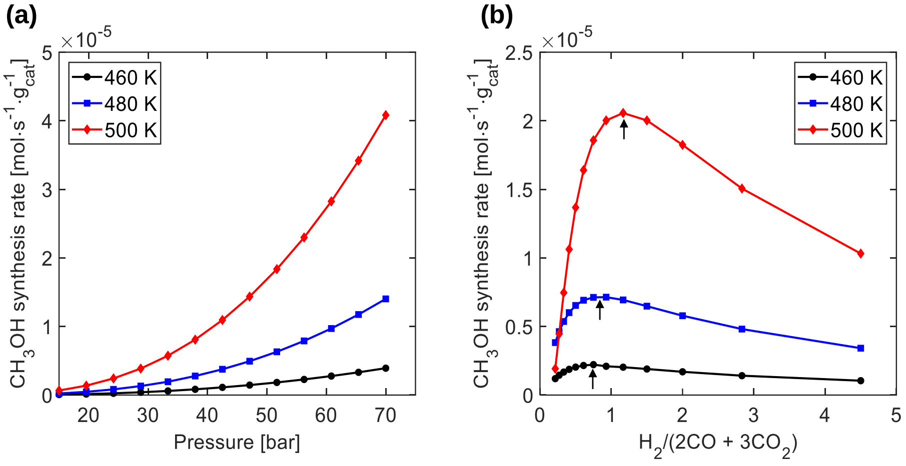

Figure 13 Effects of **(a)** pressure (stoichiometric ratio of H_2 = 2) and **(b)** stoichiometric ratio of H_2 (pressure = 50 bar) on the methanol synthesis rate at temperatures of 460, 480, and 500.

Chapter 5 Microkinetic modeling of DME synthesis from methanol over H-zeolite catalyst

5.1 Background

Due to its simple ether structure with no C–C bond, dimethyl ether (DME) contains approximately 35 % oxygen by weight, which means its combustion byproducts, such as carbon oxides and hydrocarbons, are less abundant than those of other gas-like energy resources [90]. In addition, DME produces no toxic nitrogenic or sulfonic gases during its combustion and is easily liquefied when pressurized above 0.5 MPa [91]. Therefore, it is a potential alternative to diesel as a transportation fuel due to growing concerns over its environmental impact [92-94]. DME can be also used as an intermediate in the production of olefins [95].

Among the several ways to synthesize DME, three are representative; one involve the dehydration of methanol [96, 97], and the other two involve conversion from syngas via methanol and directly to DME, respectively [94]. In addition, several recent studies for intrinsic kinetics of DME synthesis from CO_2 have been reported. Qin et al. studied the adsorption state of CO_2 on Cu (111), and established an intrinsic kinetic model for CO_2 hydrogenation to DME over a Cu-Fe-Zr/HZSM-5 catalyst [98]. It has been shown that plasma-activated CO_2 was hydrogenated to synthesize DME over a Cu-Fe-Ce/HZSM-5 catalyst, leading to the reduction of activation barrier [99]. For catalytic synthesis of DME from methanol, solid-acid catalysts are used; for example, alumina catalysts like γ-Al_2O_3 have been used in the vast majority of work due to their strong selectivity at temperatures of 200–300 °C [100, 101]. Meanwhile, as a byproduct, water deactivates the catalyst by blocking the active sites, resulting in a potential decrease in the overall catalytic reaction efficiency. Boon et al. observed the conversion of γ-Al_2O_3 into γ-AlO(OH) when the partial pressure of steam was 13–14 bar, resulting in the reduction of the catalytic activity. However, they mentioned that this conversion was reversible [102]. This problem has motivated the development of other acidic catalysts, and as a result, zeolites have been investigated as suitable substitutes for alumina catalysts. Reaction systems with these other catalysts have exhibited good conversion and selectivity with more stability in the presence of water than alumina catalysts [103]. Moreover, their catalytic properties, such as their specific surface area and crystal structure, which can affect the selectivity or acidity of the catalyst, could be suitably modified [104, 105]. Furthermore, Chiang et al. prepared a CuO-Al_2O_3 catalyst with $CuAl_2O_4$ spinel structure by a co-precipitation method in order to synthesize DME from methanol, and revealed that methanol decomposition, methanol/formic acid formations, and methanol dehydration occurred at CuO, Cu, and Al_2O_3/$CuAl_2O_4$, respectively [106]. Herrera et al. investigated methanol dehydration and plausible side reactions over Ta/Al_2O_3 and Ta/TiO_2 catalysts, and concluded that Ta/Al_2O_3 was more reactive and highly selective at temperature close to 200 ℃ [24]. Therefore, nowadays, much research on methanol conversion into DME has employed zeolites, which are also widely used industrial processes [107].

The specific characteristics of zeolites are attributed to their structural diversity. The crystal structures of zeolites vary, but most of them consist of ring-like structures, which allow microporous cage-like channels to capture molecules selectively. For such reasons, zeolites have different properties at different sizes and shapes, which makes them ideal for many catalytic chemical processes [108, 109].

There have been many works on simulating reactions over zeolites. Because it is important to understand the structural properties of zeolites at the atomic scale, DFT has been one of the most widely used methods in computational chemistry [110]. DFT calculations for zeolites have been conducted using either a periodic or a cluster model. Moses et al. reported the effect of water on the conversion of methanol to DME over the ZSM-22 zeolite using a periodic model [111], and Wang et al. simulated the conversion of methanol to olefin using a periodic model of HSAPO-34 [112]. However, because periodic models contain many atoms in a unit cell, the calculation costs are usually high. To reduce computational costs, the cluster model, which contains a finite number of atoms, has been introduced. Kachurovskaya et al. used a 3T cluster model of the FeZSM-5 catalyst for the reaction of benzene to phenol [113], and Ryder et al. used a cluster model of HZSM-5 to calculate the energy barrier of proton jumping in the presence of water [114]. Many other researchers have also used cluster models for the modeling of zeolites [115-118].

The reaction mechanisms of methanol dehydration to DME over an acidic catalyst have been studied by many researchers. In its early stages, because γ-Al_2O_3 was commonly used in methanol dehydration, Figueras et al. suggested that two methanol molecules adsorb to alumina catalysts [119], and Aguayo et al. suggested that there is a single-step synthesis mechanism over alumina bi-functional catalysts [37]. Kubelková et al. showed that methanol adsorbs to the active site of a zeolite when methanol hydration begins [120], while Blaszkowski and van Santen demonstrated a mechanism with two distinctive (associative and dissociative) pathways in the catalytic formation of DME from methanol by zeolitic protons [121]. Since then, they have proposed an additional pathway, making three pathways in total [115]. However, debates are still ongoing as to which pathway is the dominant one. Blaszkowski and van Santen compared the calculated activation barriers over an acidic zeolite on the basis of their DFT calculations and showed that DME is formed by an associative pathway, while Jones and Iglesia concluded that the dominant pathway depended on a number of conditions, such as temperature and pressure, suggesting that a dissociative pathway would be dominant at higher temperatures and lower pressures [122]. Moses and Nørskov's DFT calculations found the dissociative pathway to be dominant, and the relative reaction rates were calculated by identifying the slowest step of each pathway [111]. Recently, Gao et al. investigated three possible pathways of methanol dehydration to DME over hydrated γ-Al_2O_3 (110) by using the DFT in vacuum and liquid paraffin to suggest that $2CH_3OH(g) + 2^* \rightarrow 2CH_3OH^* \rightarrow 2CH_3O^* + 2H^* \rightarrow CH_3OCH_3^* + H_2O^*$ was the main reaction pathway while $2CH_3O^* \rightarrow CH_3OCH_3^* + O^*$ was the step having the highest activation barrier [123].

Several studies have been conducted on the kinetic modeling of DME synthesis by methanol dehydration. Aguayo et al. developed an experiment-based kinetic model for syngas conversion to DME over a CuO-ZnO-Al_2O_3/γ-Al_2O_3 bi-functional catalyst [37], where they divided their kinetic study into two parts: CO and CO_2 hydrogenations over CuO-ZnO-Al_2O_3 to synthesize methanol, followed by its dehydration to DME over an acid catalyst. They used a lumped kinetic model with four equilibrium reactions and considered the deactivation of an acid catalyst by degradation of alumina acidity. Tavan et al. also conducted lumped kinetic modeling of methanol dehydration to DME using experimental data [124], and Lu et al. suggested a new mechanism of methanol dehydration to DME on the HZSM-5 zeolite catalyst by considering both experimental and simulation results based on a lumped kinetic model [125]. Lu et al. developed a kinetic model based on only a dissociative pathway, and Mollavali et al. adopted the reaction pathway proposed by Lu et al. to develop their own kinetic model [126]. Also, Bercic and Levec found that a kinetic model based on a Langmuir–Hinshelwood mechanism with dissociative adsorption of methanol sufficiently correlated with the experimental results [103]. However, few studies have been conducted on the associative reaction pathway with lumped kinetic modeling.

As discussed above, the controversy between associative and dissociative pathways motivates analysis of the reaction mechanism, but no such analyses have been reported, especially using a detailed microkinetic model. Therefore, in this chapter, the reaction mechanisms of DME synthesis by methanol dehydration over H-zeolite were investigated using computational chemistry and microkinetic modeling, where detailed forward and backward elementary-step reactions were considered in the reaction mechanisms of both associative and dissociative pathways. In terms of computational chemistry, the second-order Møller–Plesset perturbation theory (MP2) was employed to determine the dispersion interactions that are important in the reaction system, and the computational burden of MP2 calculation was reduced by employing a 4T cluster model of H-zeolite. The structures and energies of the related reaction species were calculated, and the transition states included in the reaction pathways were determined by MP2 calculations. Using the calculated energy levels, a microkinetic model was developed with no assumptions of the rate-determining steps (RDSs); the pre-exponential factors were estimated to fit the experimental data [127] in order to increase the reliability of the microkinetic model validated in Chatper 4 [6]. Finally, the dominant pathway between the associative and dissociative pathways was discussed, and the RDSs were found using the parameter-estimated microkinetic model. In addition, the effects of temperature on the site fractions of the intermediates were analyzed.

5.2 Reaction mechanism

The overall reaction mechanism of DME synthesis by the methanol dehydration is as follows:

$$\text{Dehydration of methanol: } 2CH_3OH \leftrightarrow CH_3OCH_3 + H_2O$$

Two methanol molecules react with each other, which dehydrates them to a DME molecule through two competitive reaction pathways: one associative and one dissociative. A schematic of the two pathways is shown in Figure 14. In the associative pathway (also known as the direct pathway), two methanol molecules adsorb to the Brønsted acid site of a zeolite catalyst and then react to form DME and water simultaneously. On the other hand, in the dissociative pathway (also known as the sequential pathway), one adsorbed methanol molecule reacts to form water and a CH_3 group bound to the H-eliminated zeolite first, and then the second methanol molecule adsorbs to react with the CH_3 group to form DME, i.e., DME and water are synthesized sequentially.

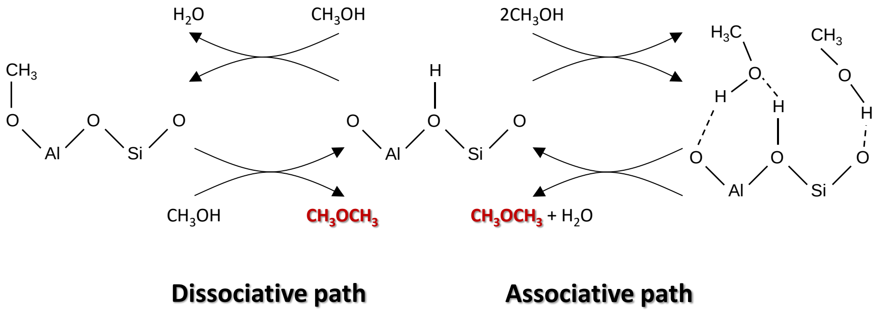

Figure 14 Dissociative (left) and associative (right) pathways for methanol dehydration.

For the computational chemistry analysis and microkinetic model, the elementary steps for methanol dehydration reaction were defined in reference to previously reported works [111, 115, 121, 122], whose details are given in Table 9. A total of 9 elementary steps and 11 reaction species, including the gaseous species, catalytic active site, and reaction intermediates, constituted the reaction system.

The elementary steps included both the associative and dissociative pathways. The reaction R1, where gaseous methanol is adsorbed (or desorbed) to the Brønsted acid site of a zeolite (H-Z), was the only elementary step contained in both pathways, while R2–R6 and R7–R9 were involved in the dissociative and associative pathways, respectively. The gas-phase species considered in this work were CH_3OH, CH_3OCH_3, and H_2O, and the reaction intermediates on the zeolite surface were CH_3OH-H-Z, H_2O-CH_3-Z, CH_3-Z, CH_3OH-CH_3-Z, CH_3OCH_3-H-Z, CH_3OH-CH_3OH-H-Z, and CH_3OCH_3-H_2O-H-Z. The elementary-step reaction rates listed in Table 9 were expressed with the site fractions of the reaction intermediates over the catalyst. Both forward and backward reactions were considered for most of the steps, while re-adsorption of H_2O was assumed to be negligible in R3 and R9.

Table 9 Elementary steps and corresponding rate equations for DME synthesis by methanol dehydration

Reaction number	Reaction mechanism	Forward reaction rate (r_f)	Backward reaction rate (r_b)
R1	$CH_3OH_{(g)}$ + H-Z ↔ CH_3OH-H-Z	$k_{\mathrm{f1}}P_{\mathrm{CH_3OH}}\theta_{\mathrm{H-Z}}$	$k_{\mathrm{b1}}\theta_{\mathrm{CH_3OH-H-Z}}$
R2	CH_3OH-H-Z ↔ H_2O-CH_3-Z	$k_{\mathrm{f2}}\theta_{\mathrm{CH_3OH-H-Z}}$	$k_{\mathrm{b2}}\theta_{\mathrm{H_2O-CH_3-Z}}$
R3	H_2O-CH_3-Z → CH_3-Z + $H_2O_{(g)}$	$k_{\mathrm{f3}}\theta_{\mathrm{H_2O-CH_3-Z}}$	–
R4	CH_3-Z + $CH_3OH_{(g)}$ ↔ CH_3OH-CH_3-Z	$k_{\mathrm{f4}}P_{\mathrm{CH_3OH}}\theta_{\mathrm{CH_3-Z}}$	$k_{\mathrm{b4}}\theta_{\mathrm{CH_3OH-CH_3-Z}}$
R5	CH_3OH-CH_3-Z ↔ CH_3OCH_3-H-Z	$k_{\mathrm{f5}}\theta_{\mathrm{CH_3OH-CH_3-Z}}$	$k_{\mathrm{b5}}\theta_{\mathrm{CH_3OCH_3-H-Z}}$
R6	CH_3OCH_3-H-Z ↔ $CH_3OCH_{3(g)}$ + H-Z	$k_{\mathrm{f6}}\theta_{\mathrm{CH_3OCH_3-H-Z}}$	$k_{\mathrm{b6}}P_{\mathrm{CH_3OCH_3}}\theta_{\mathrm{H-Z}}$
R7	CH_3OH-H-Z + $CH_3OH_{(g)}$ ↔ CH_3OH-CH_3OH-H-Z	$k_{\mathrm{f7}}P_{\mathrm{CH_3OH}}\theta_{\mathrm{CH_3OH-H-Z}}$	$k_{\mathrm{b7}}\theta_{\mathrm{CH_3OH-CH_3OH-H-Z}}$
R8	CH_3OH-CH_3OH-H-Z ↔ CH_3OCH_3-H_2O-H-Z	$k_{\mathrm{f8}}\theta_{\mathrm{CH_3OH-CH_3OH-H-Z}}$	$k_{\mathrm{b8}}\theta_{\mathrm{CH_3OCH_3-H_2O-H-Z}}$
R9	CH_3OCH_3-H_2O-H-Z → H-Z + $CH_3OCH_{3(g)}$ + $H_2O_{(g)}$	$k_{\mathrm{f9}}\theta_{\mathrm{CH_3OCH_3-H_2O-H-Z}}$	–

5.3 Methods

As similar to Chapter 4, the order of magnitude of A was used; for immobile transition states, the values of A for the molecular adsorption and desorption are of the order of 10^1 Pa^{-1} s^{-1} and 10^{13} s^{-1}, respectively, while the Langmuir–Hinshelwood surface reaction has an order of 10^{13} s^{-1} in the absence of rotation. In this work, these estimates were used as initial guesses for A when fitting experimental data, while the values of E_a were calculated by employing computational chemistry.

5.3.1 Computational Chemistry

Both bond rearrangements and van-der-Waals interactions (also called dispersion interactions) are important in systems that involve catalytic transformations of hydrocarbons over zeolites [128]. Although DFT is one of the most widely used methods in computational chemistry, the general functionals are unable to consider van-der-Waals interactions appropriately [129]. Because dispersion is the interaction between electrons and is a kind of electron correlation effect, MP2, which involves electron correlation effects, is known to describe dispersion interactions well [128] at the expense of computational cost. Therefore, to consider the dispersion interactions in an efficient manner, a 4T cluster model, which contains four tetrahedral sites (Si or Al), was used as a H-zeolite. The structure of the 4T cluster model consisting of $H_3Si–O–AlH_2–(OH)–SiH_2–O–SiH_3$ is shown in detail in Figure 15, where a Brønsted acidic OH group works as an active site of the DME synthesis reaction.

In the 4T cluster model, the replacement of only one Si atom with an Al atom has been widely used by many researches with both periodic or cluster models because the precise positions of the distributed Al atoms are difficult to determine when the structures are modeled with more than one Al atom [111, 115-118, 122, 128, 130-135]. It is worth noting that the O and Si atoms in Figure 15 are numbered in the order from left to right for convenience. In general, a cluster model of a zeolite should be neutralized by capping them with hydride (–H) or hydroxyl (–OH) bonds to prevent unphysical deformations [117, 136]. There have been the previous reports stating that differences of energies were small between H- and OH-capped cluster models, and the convergence of cluster models with the OH terminals was relatively poor when seeking transition state structures [137-140]. In this respect, the H terminals were applied to the cluster model in this study.

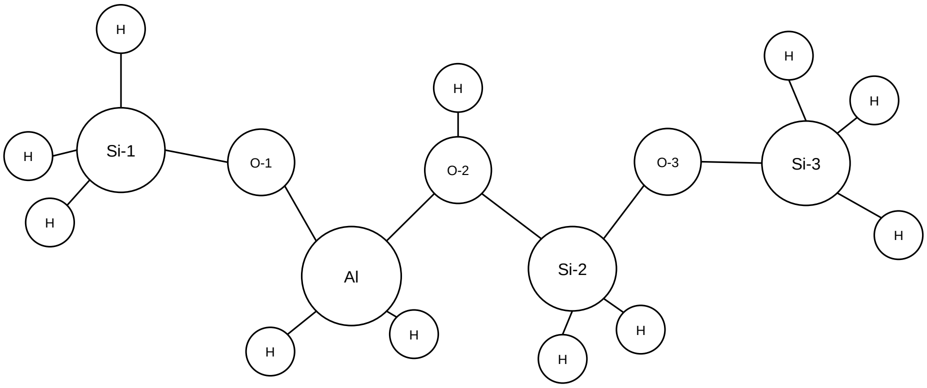

Figure 15 Framwork of the 4T cluster model used in this work.

All MP2 calculations for the reactant, reaction intermediates, products, and transition states were conducted using the Gaussian16 package [141] with the basis set of 6-311+G(2df,2p) [118, 142, 143], while transition states were determined using the optimized initial and final states. Each optimized structure in MP2 calculations was confirmed by not exhibiting any imaginary frequency, while the transition states were confirmed to have only one imaginary frequency. In addition, all energies were calculated by summing the energy obtained from an MP2 calculation (E_{MP2}) and zero-point energy (E_{ZPE}) as follows:

$$E = E_{\mathrm{MP2}} + E_{\mathrm{ZPE}} = E_{\mathrm{MP2}} + \sum_k \frac{h\nu_k}{2} \tag{5.1}$$

where E_{ZPE} was corrected using the vibrational frequencies, and h and ν_{k} represent Planck's constant and the normal mode vibrational frequencies, respectively.

The adsorption energies were calculated using the following equation:

$$\Delta E(ads) = E_{\mathrm{gas-adsorbent}} - E_{\mathrm{adsorbent}} - E_{\mathrm{gas}} \tag{5.2}$$

where $E_{\mathrm{gas\text{-}adsorbent}}$, $E_{\mathrm{adsorbent}}$, and E_{gas} represent the energies of the gas-adsorbent complexes, adsorbent species, and adsorbed species in gas-phase, respectively. A negative value of $\Delta E(ads)$ indicates an exothermic adsorption reaction, while a positive value indicates endothermic adsorption. The desorption energies were calculated by the negated version of Equation (5.2).

5.3.2 Microkinetic Model

Unlike in the lumped kinetic modeling approach, where assumptions are generally applied on the quasi-equilibriums and RDSs, microkinetic analysis determines a dominant pathway and RDSs to clearly elucidate the reaction mechanism.

To enhance the reliability of the microkinetic model in this work, pre-exponential factors were estimated by fitting experimental data from the literature [127]. Among the results for various commercial zeolites and modified H-ZSM-5 catalysts, those over the commercial H-MFI90 catalyst (Süd-Chemie, AG, Germany) were applied to the model because the others were based on Na-modified catalysts, which are outside the scope of this work. The acidity of the H-MFI90 catalyst was 0.421 mmol/$g_{\text{dry sample}}$, and 1 g of the catalyst was loaded in the reactor. The experiments were conducted at P = 17 bar, liquid hourly space velocity (LHSV) = 3.8 h^{-1}, and T = 240–330 °C. Although by-products, including methane, ethylene, and propylene, were produced under these conditions, their proportions were relatively low. Therefore, only the formation rates of DME and consumption rates of methanol for DME formation were used, while the formation mechanisms of by-products were neglected. In addition, because the experimental data were sampled under the stable conditions with no deactivation behaviors observed in time evolutionary profiles, deactivation of the catalyst was assumed to be negligible.

The site fractions of reaction intermediates were calculated by solving the system of ordinary differential equations (ODEs) obtained from the balance equations which can be referred to the Supporting Information in Appendix (Equations (S12)–(S18)), except H-Z was determined by Equation (5.3). To consider the stiffness of the ODE system, which may result from strong correlation between many reactions and reaction species, a stiff ODE solver (ode15s) was employed in MATLAB (MathWorks, Inc.) with the backward differentiation formula (BDF) algorithm.

$$\theta_{\mathrm{H-Z}} = 1 - (\theta_{\mathrm{CH_3OH-H-Z}} + \theta_{\mathrm{H_2O-CH_3-Z}} + \theta_{\mathrm{CH_3-Z}} + \theta_{\mathrm{CH_3OH-CH_3-Z}} + \theta_{\mathrm{CH_3OCH_3-H-Z}} + \theta_{\mathrm{CH_3OH-CH_3OH-H-Z}} + \theta_{\mathrm{CH_3OCH_3-H_2O-H-Z}}) \quad (5.3)$$

While activation energies were calculated using MP2, pre-exponential factors were estimated by fitting experimental data. The number of parameters to be estimated, including those for both forward and backward reactions, was 16 (see Table 9). Due to the limited number of experimental data, initial estimates of pre-exponential factors were reasonably determined by referring to the order of magnitude based on the TST and the previous literatures [49, 56], and the estimation was conducted with the lower and upper bounds of the pre-exponential factors specified to be 10^1 to 10^6 $\mathrm{Pa^{-1}s^{-1}}$ for the adsorption reactions, and 10^{13} to 10^{19} $\mathrm{s^{-1}}$ for the desorption and surface reactions. The experiments used to estimate the parameters were conducted only in change of temperature, so the estimated parameters of the microkinetic model consider the effects of temperature, while those of other operating conditions are insubstantially included in the model. Therefore, the model might be used in the limited range of pressure and site fractions.

The following objective function was minimized on the basis of the relative error sum of squares (ESS):

$$F_{\mathrm{obj}} = \sum_{\mathrm{i}}^{\mathrm{n}} \left[\left(\frac{N_{\mathrm{CH_3OCH_3,exp}} - N_{\mathrm{CH_3OCH_3,calc}}}{N_{\mathrm{CH_3OCH_3,exp}}} \right)^2 + WF \left(\frac{N_{\mathrm{CH_3OH,exp}} - N_{\mathrm{CH_3OH,calc}}}{N_{\mathrm{CH_3OH,exp}}} \right)^2 \right]_{\mathrm{i}} \tag{5.4}$$

where n denotes the number of experimental conditions, *WF* is a weighting factor, and *N* is molar flow rate. In this chapter, parameter estimation was carried out with n = 4 and *WF* = 1. The genetic algorithm (GA) was used in the optimization because it is useful when the search space is large. In addition, because it searches for the optimal points by randomly scattering population seeds and using bio-inspired operators, such as mutation, crossover, and selection [144], global and reliable minimization can be accomplished. All calculations were conducted on an Intel® Xeon® E5-2667 v4 CPU @ 3.20 GHz.

5.4 Application results and discussion

5.4.1 MP2 Calculations

The optimized structures, energy levels, and transition states of the reaction species were obtained by MP2 calculations, and the calculated energy levels were then used to calculate reaction energies (ΔE) and activation energies for the considered reactions (see Table 10).

Table 10 Reaction and activation energies for the forward and backward reactions calculated by MP2 (ZPE corrected)

Rxn no.	ΔE [eV]	E_f [eV]	E_b [eV]
R1	-0.751	0.000	0.751
R2	0.107	2.876	2.769
R3	0.374	0.374	–
R4	-0.467	0.000	0.467
R5	-0.244	2.669	2.914
R6	0.705	0.705	0.000
R7	-0.243	0.000	0.243
R8	-0.261	2.509	2.770
R9	0.978	0.978	–

The optimized structures of common species in the associative and dissociative pathways are shown in Figure 16. Figures 16 (a) and 16 (b) show a cluster of H-zeolite and its methanol-adsorbed form, respectively. The bond angles and lengths within the optimized H-zeolite were summarized in Table 11 (The atom numbering was referred to Figure 15). In the methanol adsorption, the O atom in the OH group of the methanol is bound to the Brønsted acid H atom in the zeolite, and the H atom in the OH group of the methanol also forms a weak bond with the O atom next to the Al atom (O-1) of the zeolite, as shown in Figure 16 (b). This structure has also been reported by many researchers [145-149]. The bond length of the O (methanol)–H (Brønsted acid site) was 1.519 Å, while that of the O1–H (methanol) was 1.818 Å. In addition, the methanol molecule in gas-phase had a C–O bond length of 1.420 Å, while the C–O bond length for the adsorbed one was 1.432 Å, indicating that the C–O bond of the adsorbed methanol could be more easily broken than that of the gaseous methanol. It was also seen that the O-2–H (Brønsted acid site) bond became weaker through the methanol adsorption compared to the case with no methanol adsorption. Detailed values of the bond lengths are listed to Table 12.

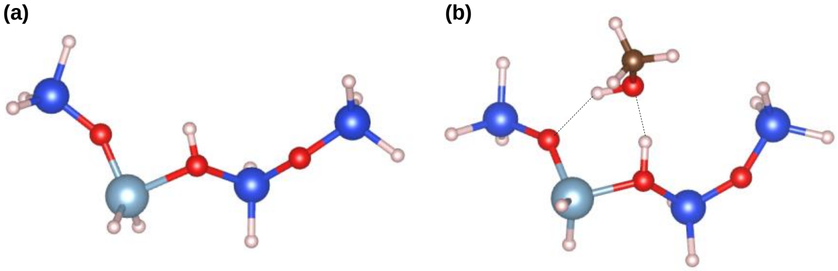

Figure 16 Optimized structures of the **(a)** 4T cluster of H-zeolite (H-Z) and **(b)** the cluster with methanol adsorbed (CH_3OH-H-Z), which are included in both the associative and dissociative pathways.

Table 11 Bond angle and length within the 4T cluster of H-Z

Bond angle or length	
∠Si2O2(H)Al	124.9 °
∠Si1O1Al	151.2 °
∠Si2O3Si3	148.4 °
Si1–O1	1.628 Å
Al–O1	1.741 Å
Al–O2	1.996 Å
Si2–O2	1.694 Å
Si2–O3	1.621 Å
Si3–O3	1.654 Å

Table 12 Comparison of bond lengths when the methanol was adsorbed to the H-zeolite (adsorbed) and not (isolated)

Bond	Bond length [Å]
C–O (isolated)	1.420
C–O (adsorbed)	1.432
O–H (isolated)	0.967
O–H (adsorbed)	1.022

5.4.1.1 Dissociative Pathway

The dissociative pathway for DME synthesis from methanol is composed of R2–R6. R3, R4, and R6 were the adsorption or desorption reactions, while R2 and R5 had the transition states of the reactions. Unlike the associative pathway in which another methanol molecule adsorbed to CH_3OH-H-Z, CH_3OH-H-Z reacted directly to form CH_3-Z and a water molecule via R2 and R3. In this reaction, a methanol molecule was split into $–CH_3$ and –OH by the breakage of a C–O bond, and then $–CH_3$ adsorbed to O-1 to form CH_3-Z, while –OH reacted with H of the Brønsted acid site to form a water molecule. This procedure is illustrated in Figure 17. The reaction energy and activation barrier of the forward reaction of R2 were 0.107 and 2.876 eV, respectively, indicating that the reaction is endothermic.

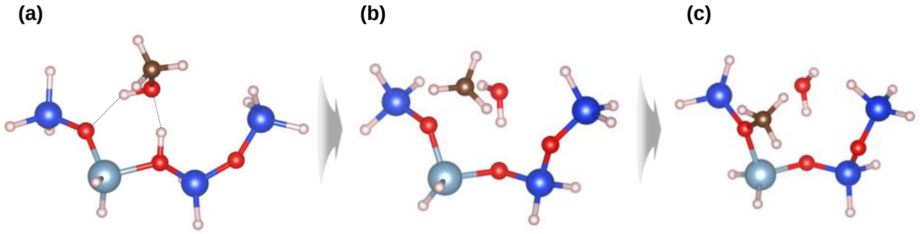

Figure 17 Reaction procedure of R2 and R3: **(a)** initial state (CH_3OH-H-Z), **(b)** transition state, and **(c)** final state (H_2O (g) and CH_3-Z).

After the formation of CH_3-Z, another methanol molecule adsorbed, as shown in Figure 18. The H atom of methanol formed a bond with O-2 with a bond length of 1.837 Å. Through the adsorption of methanol (R4), the bonding force of CH_3 to Z was weakened (bond length changed from 1.450 to 1.454 Å), making CH_3 more reactive. Also, the bond length of the O–H bond of the methanol was increased to 0.974 Å after adsorption. As in the associative pathway, the adsorption energy of the second methanol by R4 was lower than that of the first methanol (ΔE (R4) = -0.467 eV).

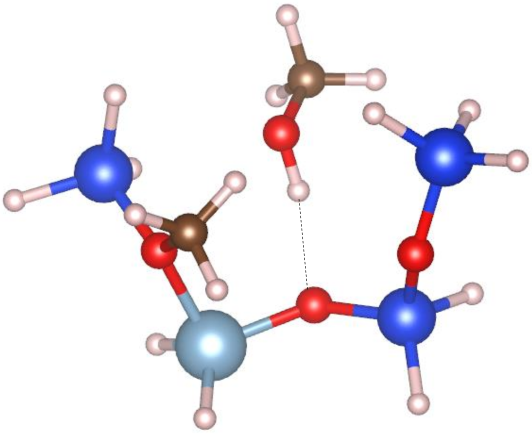

Figure 18 Methanol adsorption to CH_3-Z.

The CH_3OH-CH_3-Z complex further reacted to form DME by R5 via the procedures shown in Figure 19. The CH_3 group, which had been adsorbed to Z, desorbed to bind with the O of the second methanol molecule, and then the H of the OH group of the second methanol was released and adsorbed to Z, followed by the production of a H-Z cluster and a DME molecule (R6). The reaction energy and activation barrier of the forward reaction of R5 were -0.244 and 2.669 eV, respectively, indicating an exothermic reaction.

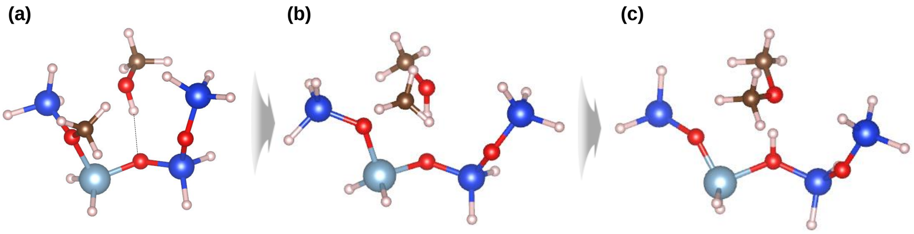

Figure 19 Reaction procedure of R5 and R6: **(a)** initial state (CH_3OH-CH_3-Z), **(b)** transition state, and **(c)** final state (CH_3OCH_3 and H-Z).

5.4.1.2 Associative Pathway

Among the reactions R7–R9 in Table 9, which constituted the associative pathway, R7 and R9 were related to adsorption/desorption, while only R8 was considered to have the transition state. The optimized structure of CH_3OH-CH_3OH-H-Z, which was formed by adsorption of the second methanol molecule to CH_3OH-H-Z (R7), is shown in Figure 20, where two methanol molecules are labeled as MeOH-1 (left) and MeOH-2 (right) for the first and the second adsorptions, respectively. MeOH-1 was more strongly bound to the catalyst than MeOH-2, as verified by the adsorption energies of ΔE (R1) = -0.751 eV and ΔE (R7) = -0.243 eV. In addition, because the C–O bond of MeOH-1 was longer (1.436 Å) than that of MeOH-2 (1.422 Å), it is plausible that the C–O bond of MeOH-1 would be broken when the DME formation reaction occurs. Figure 21 shows the evolutionary change of the structure when two methanol molecules reacted to form DME and water. As expected and shown in Figure 21 (b), MeOH-1's C–O bond was broken to form DME, and the reaction energy and activation barrier of the forward reaction of R8 were -0.261 and 2.509 eV, respectively, indicating an exothermic reaction.

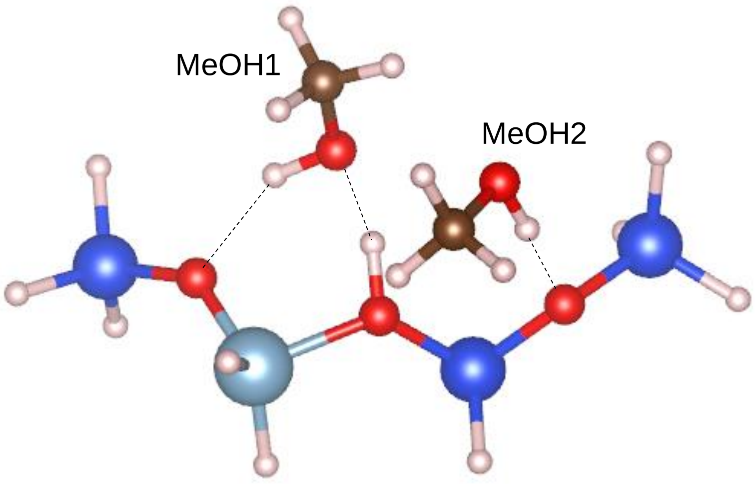

Figure 20 Optimized structure of H-Z when two methanol molecules were adsorbed.

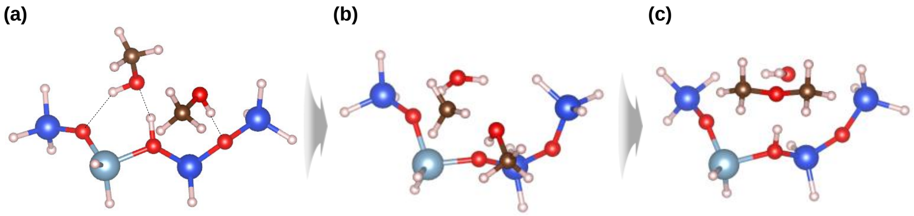

Figure 21 Evolutionary change of the structure: **(a)** initial state (CH_3OH-CH_3OH-H-Z), **(b)** transition state, and **(c)** final state (CH_3OCH_3-H_2O-H-Z).

The energy levels of the reaction intermediates in reference to the MP2 calculations are illustrated for both pathways in Figure 22, where the changes of bonds and structures along the reaction procedures are observed and discussed. From these results, it can be seen that two activation barriers of the dissociative pathway were higher than the one activation barrier of the associative pathway, indicating that the associative pathway might be dominant in DME synthesis from methanol.

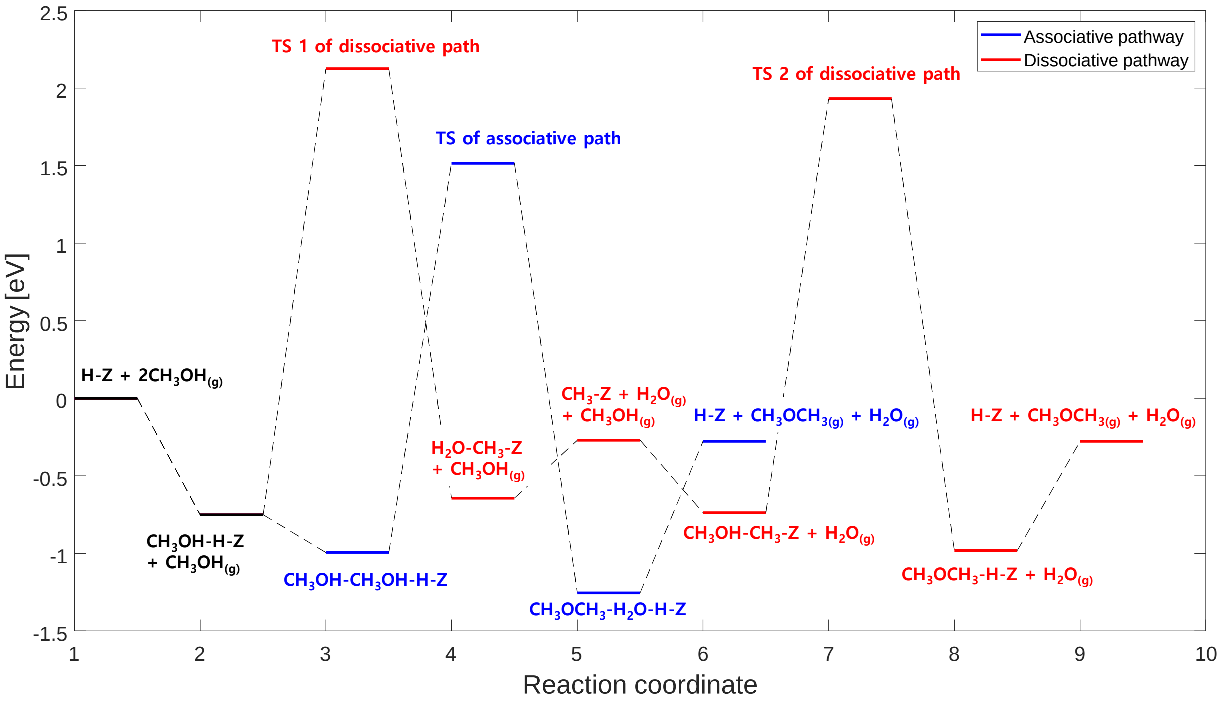

Figure 22 Energy levels of two reaction pathways for DME synthesis: Black line represents common steps in the associative and dissociative pathways, while blue and red lines represent distinctive steps for the associative and dissociative pathways, respectively.

5.4.2 Microkinetic Model

To develop a reliable microkinetic model, the estimation of pre-exponential factors was conducted by fitting the experimental data, and comparison between the data and simulated results with the estimated parameters is provided in Figure 23, where the calculated molar flow rates of DME and methanol at the reactor outlet show good agreement with the experimental data. The average errors were 14.6 and 21.8 % for DME and methanol, respectively. Details about the estimation method can be seen in Section 5.3.2, and Table 13 lists the estimated parameters.

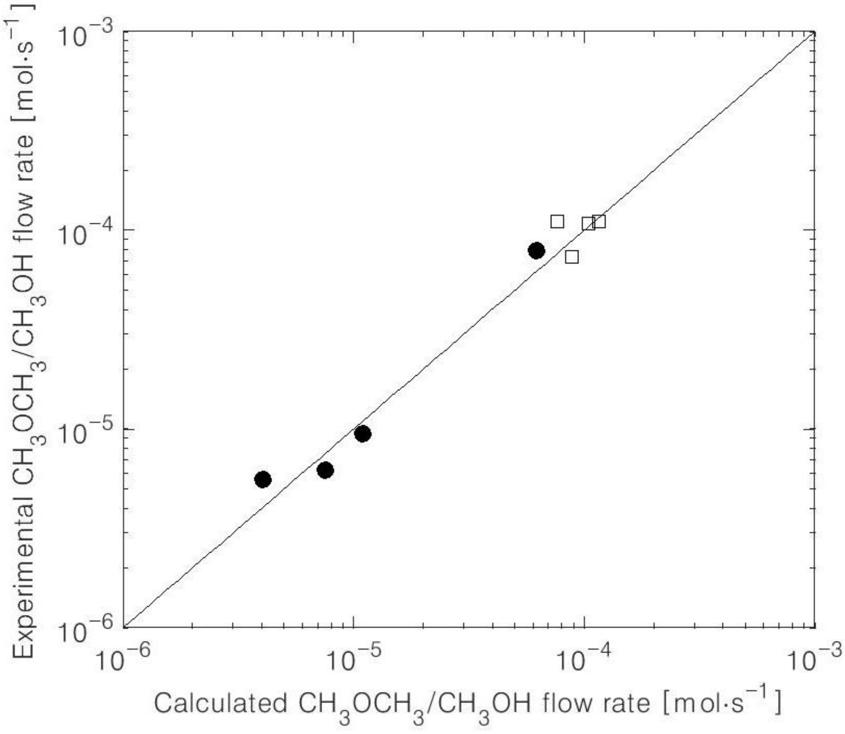

Figure 23 Experimental and calculated CH_3OCH_3/CH_3OH molar flow rates at the reactor outlet (□ CH_3OCH_3, ● CH_3OH).

Table 13 Estimated values of pre-exponential factors

Rxn no.	A_f [$Pa^{-1}s^{-1}$ or s^{-1}]	A_b [$Pa^{-1}s^{-1}$ or s^{-1}]
R1	2.09E+02	7.61E+17
R2	7.83E+14	4.17E+13
R3	2.75E+17	–
R4	1.76E+05	2.77E+15
R5	9.57E+11	3.66E+16
R6	2.29E+18	2.27E+03
R7	5.19E+01	3.17E+17
R8	6.35E+15	1.30E+16
R9	8.32E+14	–

5.4.2.1 Dominant Pathway and Rate-Determining Step

Based on the microkinetic model developed in the present work, the reaction rates of each elementary step were compared to find the dominant one between the associative and dissociative pathways. In particular, the desorption rates of DME (R6 for dissociative and R9 for associative pathways), which directly affected the DME production rate, were compared at P = 17 bar and T = 450, 475, and 500 K. As shown in Table 14, R6 was significantly faster than R9, indicating that DME was predominantly synthesized through the dissociative pathway. This result is in agreement with results from a lumped kinetic model reported in the literature [111]. Although the results based on the MP2 calculations suggest dominancy of the associative pathway, the microkinetic model analysis resulted in conflicting results. The microkinetic model considers the effects of temperature, pressure, and site fraction on the reaction system, while the MP2 calculations only evaluate the change of energy without considering those features. In other words, energy barriers alone are insufficient to determine the detailed characteristics of the reaction kinetics, such as relative reaction rates and RDSs. In addition, because H-Z was more abundant than CH_3OH-H-Z over the catalyst, methanol would be more easily adsorbed to H-Z than CH_3OH-H-Z, leading to dominancy of the dissociative pathway over the associative one. The low site fraction of CH_3OH-CH_3OH-H-Z also supports this explanation (the site fraction will be discussed in the next section).

Table 14 Desorption rates of DME for R6 and R9 at the reactor outlet at *T* = 450, 475, and 500 K

Temperature [K]	Desorption rate of DME [s^{-1}]	
	R6	R9
450	3.40E+09	5.23E-26
475	3.47E+09	1.92E-22
500	3.72E+09	1.00E-23

Among the elementary steps in the dissociative pathway, the forward directions of R2 (CH_3OH-H-Z → H_2O-CH_3-Z) and R5 (CH_3OH-CH_3-Z → CH_3OCH_3-H-Z) were much slower than the other reactions; the activation barriers of R2 and R5 were 2.876 and 2.669 eV, respectively (see Table 10). Therefore, those two reactions could significantly affect the overall DME production rate. In addition, as can be seen from the relative reaction rates of the forward reactions included in the dissociative pathway in Figure 24 on a log scale, R3 was slower than the other adsorption and desorption reactions because of the low site fraction of H_2O-CH_3-Z, which was attributed to the low reaction rate of R2. Because the reaction rate of R2 was faster than that of R5 by more than two orders of magnitude, R5 could be considered as an RDS of the synthesis reaction from methanol to DME. The literature also suggests the DME formation step (R5) as an RDS rather than the water elimination step (R2) [111]. However, despite the relatively slower rate of R5 than that of R2, the degrees of both reactions are slow compared to the other reactions, and it can thus be concluded that R2 might be an RDS alongside R5.

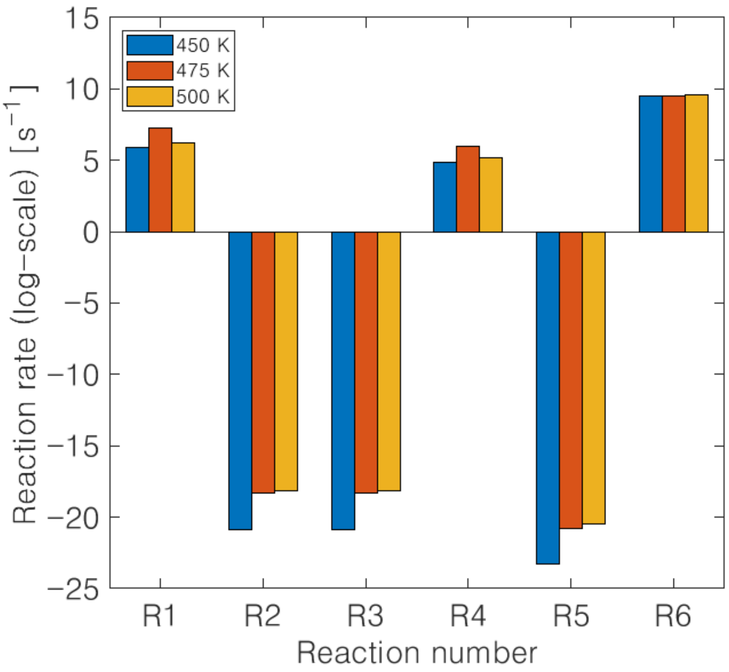

Figure 24 Relative forward reaction rates for the dissociative pathway (R1–R6) on a log scale at T = 450, 475, and 500 K.

5.4.2.2 Site Fractions

Because temperature is an important factor affecting the reaction rates and pathways, the developed microkinetic model was employed to analyze the effects of temperature on the site fractions. Although the model could evaluate the effects of other operating conditions, such as pressure and feed composition, only temperature was considered because the experimental data used in the estimation considered temperature variation only.

As shown in Figure 25 (a), the most abundant site was H-Z, and the next most were CH_3OH-H-Z, CH_3-Z, CH_3OH-CH_3-Z, and CH_3OCH_3-H-Z, which were all involved in the dissociative pathway. The others had site fractions under 10^{-6}, as shown in Figure 25 (b), describing the change of site fractions of the intermediates in associative and dissociative pathways at the reactor outlet with respect to temperature from 473.15 to 573.15 K. It is worth noting that the site fractions along the reactor axis showed the same trend as those in the reactor outlet. As shown in Figure 25 (a), as temperature increased, the site fractions of CH_3OH-H-Z and CH_3OCH_3-H-Z decreased significantly, while the site fraction of CH_3OH-CH_3-Z only slightly decreased. Meanwhile, the site fractions of H_2O-CH_3-Z (Figure 25 (b)) and CH_3-Z (Figure 25 (a)) increased. Referring to those trends, it appears that the adsorption of methanol and desorption of DME are more significantly influenced by temperature than the other steps. Therefore, the water elimination step (R2) in the dissociative pathway, which is one of the RDSs, may become less important than R5 as the operating temperature increases. In addition, by referring to the much lower site fraction of H_2O-CH_3-Z, it could be concluded that H_2O rapidly desorbed immediately after R2 in which H_2O-CH_3-Z was formed from CH_3OH-H-Z. As mentioned earlier, the site fraction of H-Z was much higher than that of CH_3OH-H-Z (Figure 25 (a)), causing a methanol molecule to adsorb to H-Z rather than CH_3OH-H-Z. Also, the site fractions of reaction intermediates included in the associative pathway, such as CH_3OH-CH_3-H-Z and CH_3OCH_3-H_2O-H-Z, were much lower than those of the intermediates included in the dissociative pathway, leading to dominancy of the dissociative pathway. That is, the high site fractions of the reaction intermediates included in the dissociative pathway resulted in the high reaction rates of the dissociation and the dominance of the dissociative pathway. In conclusion, the conflicting results obtained from the MP2 calculations and the microkinetic model could be explained by the abundancy of intermediates in the dissociative pathway over the catalytic sites, which could only be considered in the microkinetic model.

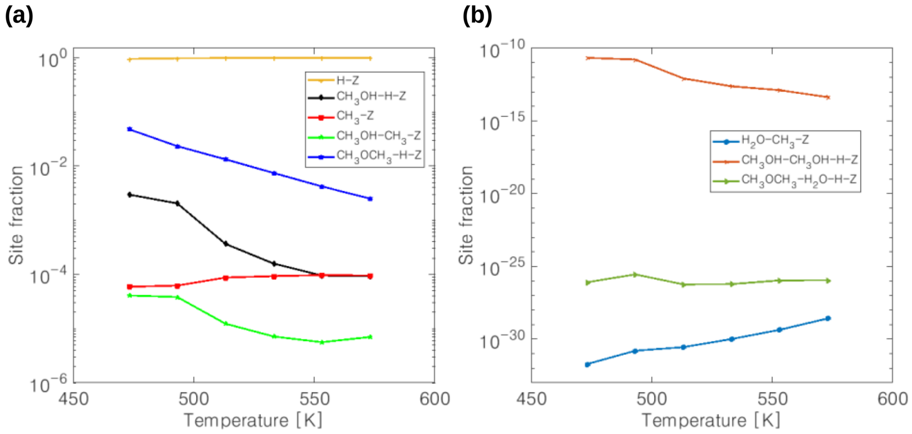

Figure 25 Effects of temperature on the site fractions on a log scale for the intermediates whose values were **(a)** > 10^{-6} and **(b)** < 10^{-6}.

Chapter 6 Machine Learning-based Surrogate Model of Microkinetics for the Water-Gas Shift Reaction

6.1 Background

It has been desired to achieve the coupling of the detailed kinetics and CFD simulations of catalytic reactors because it is a multiscale technique that integrates the quantum to the reactor level giving fundamental knowledge of catalysis to realistic reactor modeling [150, 151]. Coupling the microkinetics with CFD simulations has the advantage of calculating site fractions of surface intermediates, rates of elementary step reactions and concentrations of various byproducts in CFD environments, which cannot be obtained by conventional kinetic models. Therefore, it is possible to investigate the mutual interaction between transport phenomena including mass, momentum and energy transport, and detailed reaction kinetics. Moreover, by modeling a solid catalyst packed in a reactor, the distribution of the adsorbed intermediates in the pore of the catalyst would be known, which can offer the specific information, for example, disclosing causes of conversion, yield or selectivity loss. Despite being aware of this importance, it is so challenging that linking modeling techniques with distinctly different time and length scales. In addition, in case of the microkinetics, the model is so complex, non-linear and stiff that it is difficult to solve together with CFD simulations. Nevertheless, to overcome these problems, efforts to map the catalytic reaction rates and the concentrations of gas and surface species before or during CFD simulations have been made to implant detailed chemical kinetics into continuum mechanics for chemical reactor modeling by many researchers [152-158].

To map detailed kinetics exactly without reducing the details, methodologies for tabulating and interpolating pre-computed data derived from detailed kinetics are required. In general, data calculated from detailed kinetics such as the microkinetics inevitably have high dimensions, and suitable techniques for a surrogate model for data with these characteristics is machine learning techniques because these are not based on linear regression. For this reason, in this chapter, a microkintic model for the WGS reaction was developed firstly by fitting the pre-exponential factors to the experimental data in the same ways as the previous chapters, and then machine learning-based surrogate models were developed by using the pre-computed datasets derived from the microkinetic model for the WGS reaction. Two machine learning methods which were the ensemble learning method, the ExtraTrees algorithm, and the artificial neural network (ANN) were used and the results from them were compared. The two methods were chosen since an ANN has been known to be very good at regression, and the ExtraTrees algorithm can measure the feature importance which is a primary interest in microkinetic studies.

The pre-computed data were the steady-state solutions of the microkinetic model. Therefore, for coupling the microkinetics with the CFD simulation, pseudo steady-state approximation for the chemical reactions was required. Fortunately, in typical catalytic reactor systems, the time scales of a microkinetic model (nanosecond to millisecond) are generally much shorter than those of transport phenomena (millisecond to kilosecond), making the assumption reasonable. Still, in some specific cases such as the presence of microscopic flows, dimensionless numbers like the Damköhler numbers (Da) must be calculated to determine whether the assumption is valid. Da is defined as a ratio of reaction rate to flow rate, so that pseudo steady-state approximation is valid when Da << 1.

6.2 Reaction Mechanism

The elementary steps for WGS reaction were referred to Gokhale et al.'s work where the two competitive mechanisms, the redox and the carboxyl mechanisms, were involved [50]. Moreever, they considered the pathway forming a formate (HCOO) species. The elementary steps and their activation energies from Gokhale's group were summarized in Table 15.

Table 15 The elementary steps for WGS reaction and their activation energies from Gokhale et al.'s work [50]†

No.	Reaction	E_f [eV]	E_b [eV]
R1	$CO + * \leftrightarrow CO*$	0	0.51
R2	$H_2 + 2* \leftrightarrow 2H*$	0.54	1.07
R3	$H_2O + * \leftrightarrow H_2O*$	0	0.18
R4	$CO_2 + * \leftrightarrow CO_2*$	0	0.09
R5	$H_2O* + * \leftrightarrow OH* + H*$	1.36	1.35
R6	$OH* + * \leftrightarrow O* + H*$	1.76	1.28
R7	$2OH* \leftrightarrow H_2O* + O*$	0.60	0.00
R8	$CO* + O* \leftrightarrow CO_2* + *$	0.82	1.69
R9	$CO* + OH* \leftrightarrow$ *cis*-COOH* + *	0.61	0.59
R10	*cis*-COOH* ↔ *trans*-COOH*	0.52	0.75
R11	*trans*-COOH* + * ↔ $CO_2* + H*$	1.41	1.80
R12	*trans*-COOH* + OH* ↔ $CO_2* + H_2O*$	0.42	0.82
R13	$CO_2* + H* \leftrightarrow HCOO* + *$	1.02	0.74
R14	$HCOO* + * \leftrightarrow HCOO**$	0.10	0.55
R15	$CO_2* + H_2O* + * \leftrightarrow HCOO** + OH*$	1.69	1.83
R16	$CO_2* + OH* + * \leftrightarrow HCOO** + O*$	2.02	1.75

†Symbol * represents vacant sites and HCOO** refers to bidentate species, while E_f and E_b denote the forward and backward activation energies, respectively.

They also included *cis*-COOH to *trans*-COOH isomerization after the formation of the first carboxyl species, and the activation energies were calculated using DACAPO DFT code [159, 160].

6.3 Methods

6.3.1 Microkinetic Model

Like in the previous chapters, the pre-exponential factors were estimated by fitting Koryabkina et al's experimental data [161]. Among the various experimental sets they conducted, the data of the commercial 40 % CuO–ZnO–Al_2O_3 catalyst sample from United Catalysts were used because it described the details of the experimental conditions and results including total flow rate, total pressure, temperature, gas composition, and turnover rate (TOR). The experiment was conducted in a CSTR at 190 °C temperature, 1 atm total pressure, total inlet flow rate 118 ml min^{-1}, 0.2 g of catalyst, and copper surface area of 9.6 m^2 g^{-1}.

The microkinetic model was developed on the basis of the experiments, and the site balances consisting of the system of ODEs were solved by a stiff ODE solver, ode15s, in MATLAB with the backward differentiation formula (BDF) algorithm. Also, parameter estimation was conducted through the genetic algorithm with the aim of minimizing errors in turnover rate (TOR) valules of calculations and experiments.

For obtaing the pre-computed datasets, operating conditions such as temperature, pressure and compositions of gaseous species were varied, and site fractions, molar flow rate of gaseous species, and elementary reaction rates were calculated under those conditions by using the developed microkinetic model. The operating conditions were summarized in Table 16. In Table 16, compositions of gaseous species were referred to Koryabkina's work [161], and remaining composition is for inert gas Ar. The combination of these operating conditions resulted in a total of 9,633 datasets.

Table 16 Varied range of operating conditions for making the pre-computed datasets

Operating condition	Range
Temperature [°C]	180–240
Pressure [atm]	1–20
Composition of	
CO	0.038–0.197
CO_2	0.070–0.173
H_2	0.203–0.504
H_2O	0.081–0.379

6.3.2 Surrogate Model

A Random Forest is an ensemble learning method used for classification or regression. It is one of the best machine learning algorithms, learning an ensemble of decision trees via bagging or pasting method. Its algorithm is simple and convenient, but it performs high accuracy even with relatively small training datasets and can overcome overfitting. Moreover, although a Random Forest algorithm is a black box model as other high-performance machine learning techniques, it can measure easily the feature importance. The more important features are, the closer to the root of the tree rather than the leaves the features appear. ExtraTrees (extremely randomized trees) algorithm, which randomizes decision trees extremely, is an improved version of Random Forests by using random thresholds for each feature and selecting the best splitting rather than finding the best possible thresholds at every node [162]. ExtraTrees is much faster to train than Random Forests and more effective in dealing with high-dimensional data owing to its less variance than regular Random Forests.

ANNs, which mimic the human neural system to learn the relationship between the given data and solutions, are one the most popular and effective machine learning methods being used. Although the concept of a perceptron, which is the working unit of an ANN, was first introduced in 1958, the development progress of ANNs had come to a halt until the early 2000s, due to the problem of overfitting and the vanishing gradient problem. Overfitting is a common problem found in regression algorithms. When a complex function is used to fit a set of data points, the resulting regression function tends to “overly fit” the given data set, thus showing low accuracy when new data points are applied. The performance of an ANN naturally improves when the number of nodes in each layer, and the number of layers increase, due to the increasing number of parameters used to fit the data points, but it becomes vulnerable to overfitting. Another big problem of ANNs is the vanishing gradient problem, but we do not need to dive deeper into that problem.

Owing to the development of novel activation functions (regularized linear units (ReLU), softmax activation function, etc.) and the increase in computational power made available by the development of general purpose graphical processing units (GPGPU), ANNs have made astonishing progress in the past 10 years, affecting various fields of study. By appropriately selecting a set of feature inputs and the structure of the ANN, an ANN is able to effectively learn the complex relationships between the input-output dataset. In this section, both ExtraTrees algorithm and ANN were used for regressing the microkinetic model, and the results from them were compared and analyzed.

6.3.2.1 ExtraTrees

Three surrogate models were developed using the ExtraTrees algorithm: (1) Temperature, pressure, and gas compositions as inputs, and site fractions, molar flow rate of gaseous species and elementary reaction rates as outputs, which can be used as a surrogate model of a microkinetic model for CFD simulations; (2) Elementary reaction rate as an input, and TOR as an output for investigating the relative importance of each reaction to TOR; (3) Site fraction as an input, and TOR as an output for investigating the relative importance of a site fraction of each surface intermediate to TOR.

Bagging is short for bootstrap aggregating (also called bootstrapping), which is a random sampling method performed with replacement. By using bootstrapping, the correlation between trees and the variance are reduced [163]. Therefore, bootstrap sampling was used when building trees in this study. In case of using bootrapping, out-of-bag (oob) samples are available. When using bootstrapping, some traning datasets may not be sampled at all, and these are called the oob samples. ExtreTrees use the oob samples as validation sets so that separate validation or cross-validaion is not necessary. Splitting datasets into the training and the test sets was conducted with the ratio of 3:1, respectively.

6.3.2.2 Artificial Neural Network

An ANN was designed to effectively accommodate the features of a chemical reaction, using the temperature, pressure, and composition values as inputs to predict site fractions, molar flow rate, and reaction rates of each elementary step. A properly trained ANN could significantly reduce the computation time for the calculation of site fractions and reaction rates while providing high accuracy for the reaction rate values.

When using ANNs for regression, the most important step is the selection of features that can effectively be used to predict the output data. In the case considered in this study, although temperature, pressure, and the composition of the individual components have been used to calculate the site fractions and reaction rates, using values in their current form may not provide sufficient results. In this study, the output variables were derived from the reaction rate equation. Although equations of first principles were not directly incorporated into the ANN design, extracting features based on its format could enhance the performance of the ANN. Consider a typical reaction rate equation:

$$r_{\mathrm{f}} = k[A]^{n}[B]^{m} \tag{6.1}$$

$$k = Ae^{-\frac{E_{\mathrm{a}}}{RT}} \tag{6.2}$$

where r_{f} is the reaction rate, k is the reaction constant consisting of the Arrhenius equation and the activation energy, and the $[A]$ and $[B]$ are the activity values of the components A and B.

To enhance the training performance and to ensure that no gradient vansishing occurs due to difference in order of magnitude among the data variables, the log-scale data of each of the input and output variables were used for ANN training. Observing the regression performance of different data preprocessing, it was concluded that normalizing the negative reciprocal form of temperature variable ($-1/T$) that is the form in the Arrhenius equation only and using the rest of data in log forms was the best option.

The neural network was designed using two hidden layers, with 10 nodes for the first hidden layer and 46 nodes for the second hidden layer, and the sigmoid activation function was used. The implemented neural network structure was visualized in Figure 26.

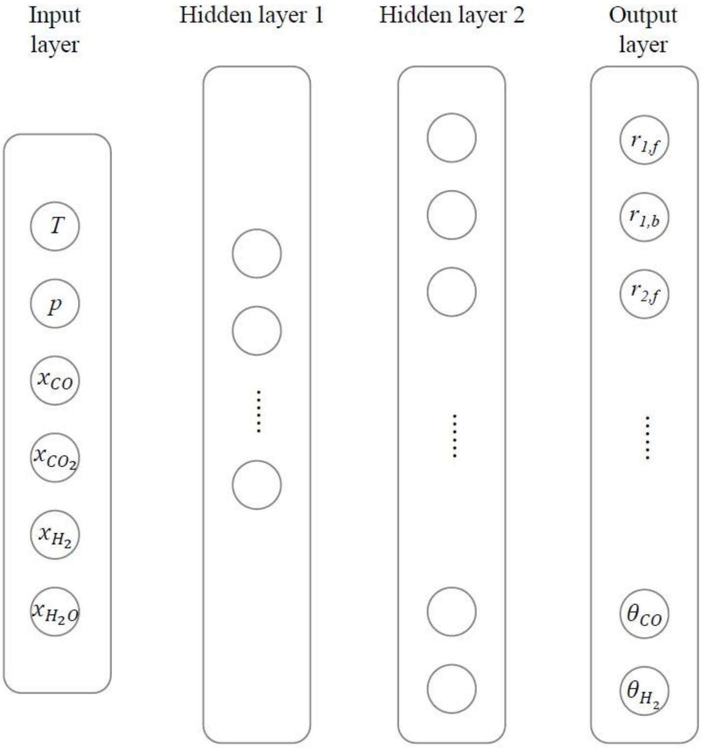

Figure 26 The implemented ANN structure.

There were 6 input variables and 46 output variables, where temperature values were input as $(-1/T)$, and the rest of the input and the output variables were input as log forms. The datatset was split so that the training data consisted of 70 % of the entire data, and the validation and test data consisted of 15 % of the whole data set, respectively.

6.4 Application Results and Discussion

6.4.1 Microkinetic Model

In order to construct a reliable microkinetic model for WGS reaction, the pre-exponential factors were fitted to the experimental data, and the parity plot was shown in Figure 27, and the estimated values were described in Table 17. As in the previous chapters, the pre-exponential factors of the adsorption reactions (the forward reactions of R1–R4) were estimated on the basis of the value 10^1, while those of the other reactions, the desorption and the surface reactions, were based on the value 10^{13}.

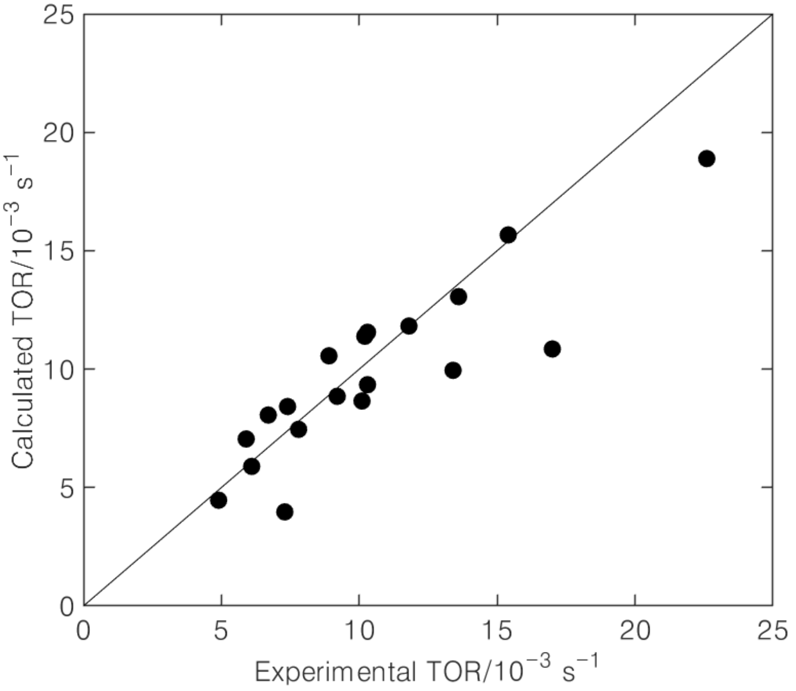

Figure 27 Parity plot of the experimental and the calculated turnover rates.

Table 17 Estimated values of the pre-exponential factors for WGS reaction

Rxn no.	A_f [$Pa^{-1}s^{-1}$ or s^{-1}]	A_b [$Pa^{-1}s^{-1}$ or s^{-1}]
R1	2.03E+00	8.20E+14
R2	1.02E+01	7.70E+11
R3	1.20E+04	8.27E+10
R4	2.11E+01	3.90E+12
R5	4.76E+14	3.80E+14
R6	2.88E+10	6.45E+15
R7	1.62E+16	8.54E+10
R8	9.98E+15	1.49E+15
R9	1.35E+12	7.08E+14
R10	1.29E+13	5.60E+15
R11	2.64E+15	3.56E+10
R12	1.75E+11	5.62E+14
R13	6.64E+10	5.30E+14
R14	7.79E+15	1.10E+12
R15	5.29E+14	8.97E+15
R16	1.84E+15	6.07E+11

6.4.2 Surrogate Model

6.4.2.1 ExtraTrees

For training through ExtraTrees, the number of decision trees in the forest should be decided because this parameter significantly affects the performance of a surrogate model. Therefore, the average errors were measured by increasing the number of decision trees for the three types of surrogate models developed in this chapter. The result of the first model that might be a surrogate model of the microkinetic model was described in Figure 28. As shown in the Figure, the errors both on the test and the training sets were decreasing as the number of decision trees increased. Considering both the accuracy and the computational cost, it seemed optimal to use about 300 trees by which the model could have about 2.7 % error.

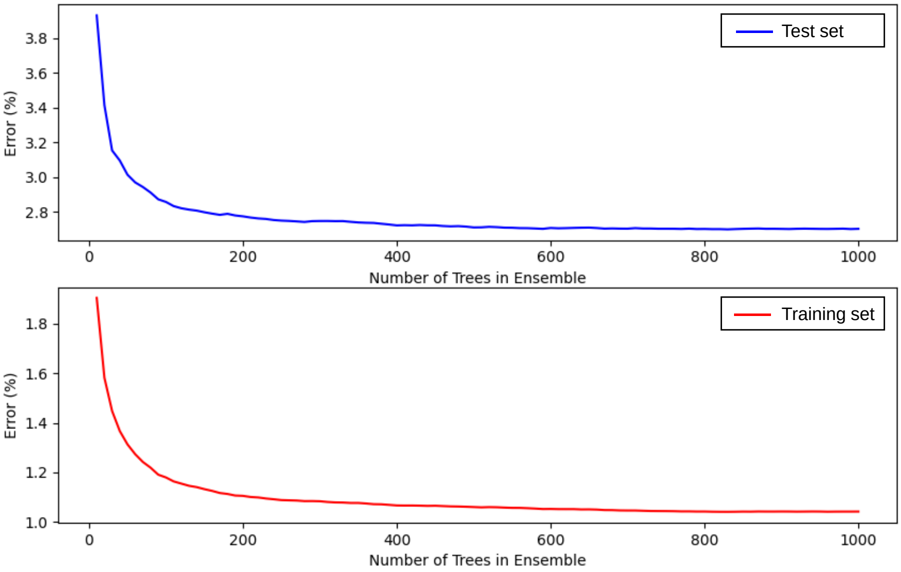

Figure 28 Changes of errors as increasing the number of decision trees in ensemble for the test (upper; blue line) and the training sets (lower; red line).

As mentioned above, ExtraTrees could provide the relative importances of input features to outputs. In microkinetic studies, elucidating the factors that affect the overall reaction is the main purpose. Therefore, the relative importances of each elementary reaction and intermediate covering catalyst surfaces are invaluable information to catalysis researches. In this study, the relative importances of the elementary steps and the surface intermediates to the TOR, a representative of the overall reaction, and were described in Figure 29. Referring to Figure 29 (a) and (b), top 5 most affecting reactions were r_{b12} ($CO_2^* + H_2O^* \rightarrow$ *trans*-$COOH^* + OH^*$), r_{f8} ($CO^* + O^* \rightarrow CO_2^* + {}^*$), r_{b16} ($CO_2^* + OH^* \rightarrow HCOO^{**} + O^*$), r_{b15} ($HCOO^{**} + OH^* \rightarrow CO_2^* + H_2O^*$), and r_{b10} (*trans*-$COOH^* \rightarrow$ *cis*-$COOH^*$), while the surface intermediates were $HCOO^*$, $HCOO^{**}$, O^*, H^*, and OH^* within the operating range referred to Table 16. Considering these results, we can see easily which reaction is more dominant and important than the competitive reaction through the ExtraTrees algorithm.

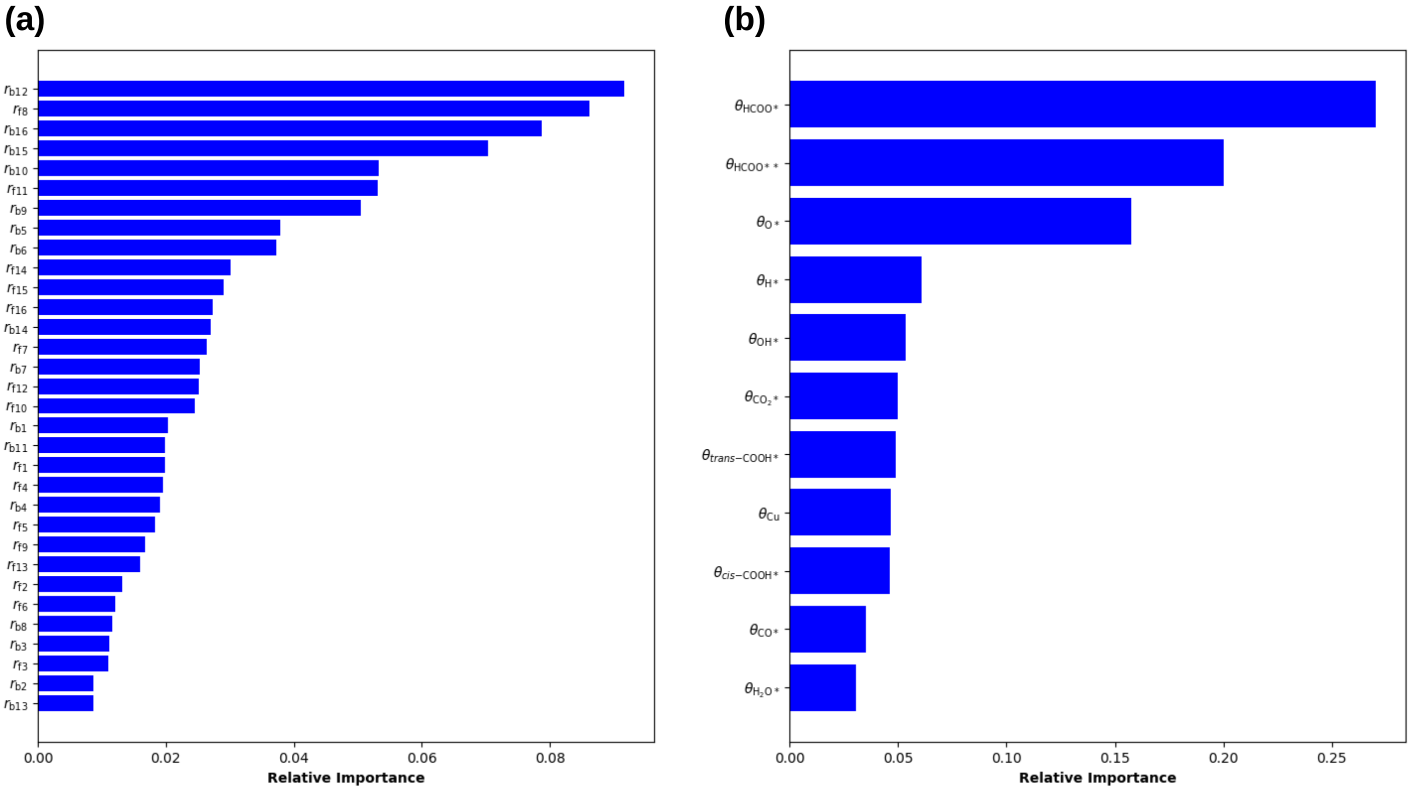

Figure 29 Relative importances of **(a)** the elementary reaction rates and **(b)** the surface intermetiates to the TOR.

6.4.2.2 Artificial Neural Network

The results described in Figure 30 showed that the designed ANN shows good performanace regarding the validation and test datasets. The overall training process converged quickly so only 200 iterations of backpropagation calculations were applied. The mean squared error (MSE) values are in the order of 10^{-4}, and the error values are distributed around zero with a small standard deviation, showing the stability of the trained ANN. The MSE values are in the same order for the training, validation and test datasets, which means that the ANN model has not been overfitted, and can be applied to various operating conditions and gas compositions. The accuracy of the reaction rate estimation shows an average of 0.01 %, which will have minimal errors when applying the estimated results to other usages, for example for CFD simulations.

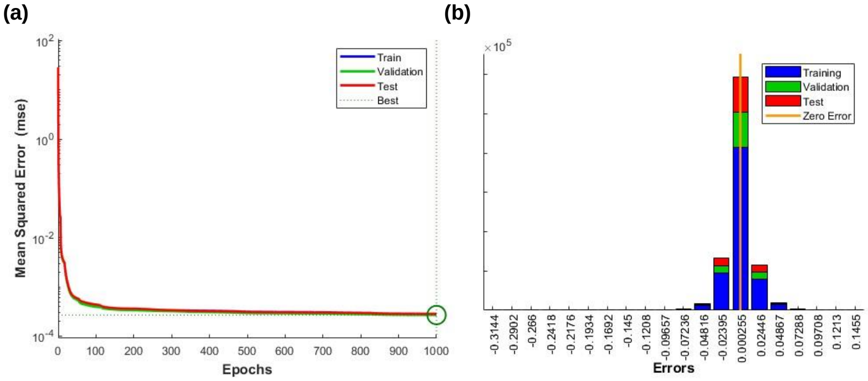

Figure 30 Performance of regression by the ANN; **(a)** Mean squared error between the predictions by the ANN and the microkinetic model; **(b)** The error distribution.

Chapter 7 Concluding Remarks

7.1 Summary of Contributions

Practical and theoretical approaches for lumped- and micro-kinetic modeling with parameter estimation were presented in this thesis. Also, by using the first-principles calculation, information about the structures, the energies and the reactivities of chemicals adsorbed on catalytic surfaces were be given. All the developed microkinetic models retained the reliability through parameter estimation to fit the experimental results with the genetic algorithm which is the commonly used global optimization algorithm. By estimating the kinetic parameters using the genetic algorithm, the computational load was able to be mitigated without calculating vibrational frequencies through the DFT, which has been a drawback in most of the previous microkinetic modeling works, and the reliability was increased in that the model was based on experimental data. Ultimately, analysis using the developed models gave the insight in what the important reactions and pathways are, and what the efficient operating conditions are. Lastly, surrogate models of microkinetic models based on machine learning techniques were presented for subsequent applications to higher-scale reaction engineering such as CFD and process simulations. Moreover, important features to the relevant overall reaction could be suggested by the ExtraTrees algorithm. To sum up, the main contributions of each chapter were summarized below.

Chapter 3 provided a lumped kinetic model for the direct synthesis of DME from syngas over a hybrid CZA/FER catalyst, highlighting the differences between lumped- and micro-kinetic models. Reaction rates with estimated kinetic parameters determined by fitting the experimental data evidently showed that the model is capable of describing the experimental behavior. The estimated parameters of the hybrid catalyst were compared with the reported values of conventional catalysts to evaluate the effects of the hybridization of the CZA and FER catalysts on the catalytic behavior. The activation energies of the methanol synthesis from syngas were high, whereas those of the DME synthesis from methanol were lower than the value calculated by applying computational chemistry to the conventional zeolite catalyst. It may seem that the diffusion resistance plausibly plays an important role, due to the core-shell structure of the hybrid catalyst. The methanol synthesis step may have more control over the rate than the methanol dehydration step, and a temperature between 200 and 220 °C was determined for thermal energy efficiency.

In Chapter 4, a practical microkinetic modeling approach for methanol synthesis from syngas over a Cu-based catalyst was described by considering 28 possible elementary-step reactions for CO hydrogenation, CO_2 hydrogenation, and the water-gas shift reaction. A combination of the DFT and the semi-empirical UBI-QEP method was used to determine the reaction and activation energies, and the pre-exponential factors were estimated. The proposed method was shown to be efficient because computationally intense procedures, such as the calculation of vibrational frequencies, as well as partition functions of translational, rotational, and vibrational motions, are no longer required. In order to reduce the stiffness of the microkinetic model, partial equilibrium ratios were calculated. The estimated parameters on the basis of the experimental data increased the reliability of the reaction pathways proposed by the microkinetic model. As a results of the modeling, the most dominant pathways of CO and CO_2 hydrogentaions, and the RDS, the surface reaction of H_3CO* and H*, were elucidated.

Chapter 5 proposed a microkinetic model of DME synthesis from methanol over H-zeolite catalyst. For considering the London dispersion forces, the energy calculations were based on the MP2 instead of the DFT with a 4T cluster model for the H-zeolite, and the transition states of the reactions were found. After modeling the microkinetics through parameter estimation, the dissociative pathway was suggested as a dominant pathway, and the DME formation reaction of the dissociative pathway was found to be the RDS.

In Chapter 6, machine learning techniques were applied for alternating a microkinetic model of the water-gas shift reaction. In order to transfer the microkinetic information into the higher-scale simulations such as CFD and process simulations, a surrogate model is necessary because a microkinetic model is so complex and difficult to solve that direct combination with other simulation tools is challenging. ExtraTrees and an artificial neural network (ANN) were used for regressing the mirokinetic data derived through the developed model. Operating conditions such as temperature, pressure and gas compositions were the input variables, while gas molar flow rates, site fractions of the surface intermediates and elementary reaction rates were the output variables. the developed surrogate models could predict the results of the microkinetic model with the same operating conditions. As a result, the ANN showed better performance when it comes to regression, while the important reactions and surface intermediates were elucidated through the ExtraTrees algorithm.

7.2 Future Work

Future works on the microkinetics would be likely to be able to proceed in two directions: (1) Developing multiscale modeling platforms of catalytic reaction engineering from the quantum to the process scales, and (2) Applying several techniques to the microkinetics for digging up correlations between elementary reactions or surface intermediates more obviously by simplifying the microkinetics, for example, the dimension reduction or for a rigorous microkinetic modeling itself.

As described in Chapter 6, a microkinetic model could be mapped into a simpler surrogate model by machine learning methods. These surrogate models are more suitable to be used for CFD or process simulations owing to their cost-effectiveness, facilitating the linkage within multiscale modeling. If it is possible to analyze the first-principles based microkinetics even in CFD and process simulations, the multiscale model would make the synergetic effects on improving chemical processes. However, it should be kept in mind that there might be several limitations. As explained in Chapter 6, in specific situations where the time scales of transport phenomena are not much longer than those of elementary reactions, the steady-state assumption on the reaction kinetics is not valid. Furthermore, machine learning techniques are basically interpolative methods and very good at interpolation, but poor at extrapolation. Thus, for utilizing the machine learning-based surrogate model in the desired range of operating conditions, additional datasets would be needed to extend the model.

Apart from this, the microkinetic study itself can be conducted. At present, a microkinetic model is too stiff to solve easily and vulnerable to diverge during calculations, and reasonable methods to resolve these problems can be studied. Also, more various analysis using a microkinetic model is possible if analytical techniques are applied for simplifying and visualizing the microkinetics, which would make progess in exploration of reaction mechanisms. By breaking the limitations, more rigorous microkinetic models would be developed, and there will be more information available from the microkinetics.

Appendix

Supporting Information

System of Differential Equations for the Site Balances in Chapter 4

$$\frac{d\theta_{\mathrm{H_2O}}}{dt} = r_{\mathrm{f4}} + r_{\mathrm{b10}} + r_{\mathrm{b11}} + r_{\mathrm{f13}} + r_{\mathrm{b25}} + r_{\mathrm{f28}} - r_{\mathrm{b4}} - r_{\mathrm{f10}} - r_{\mathrm{f11}} - r_{\mathrm{b13}} - r_{\mathrm{f25}} - r_{\mathrm{b28}} \tag{S1}$$

$$\frac{d\theta_{\mathrm{CH_3OH}}}{dt} = r_{\mathrm{f6}} + r_{\mathrm{f20}} + r_{\mathrm{f27}} - r_{\mathrm{b6}} - r_{\mathrm{b20}} - r_{\mathrm{b27}} \tag{S2}$$

$$\frac{d\theta_{\mathrm{O}}}{dt} = r_{\mathrm{b7}} + r_{\mathrm{f12}} + r_{\mathrm{f13}} + r_{\mathrm{f17}} + r_{\mathrm{f22}} + r_{\mathrm{b24}} - r_{\mathrm{f7}} - r_{\mathrm{b12}} - r_{\mathrm{b13}} - r_{\mathrm{b17}} - r_{\mathrm{b22}} - r_{\mathrm{f24}} \tag{S3}$$

$$\frac{d\theta_{\mathrm{OH}}}{dt} = r_{\mathrm{b8}} + r_{\mathrm{f10}} + r_{\mathrm{f11}} + r_{\mathrm{b12}} + 2r_{\mathrm{b13}} + r_{\mathrm{f18}} + r_{\mathrm{b24}} + r_{\mathrm{f25}} - r_{\mathrm{f8}} - r_{\mathrm{b10}} - r_{\mathrm{b11}} - r_{\mathrm{f12}} - 2r_{\mathrm{f13}} - r_{\mathrm{b18}} - r_{\mathrm{f24}} - r_{\mathrm{b25}} \tag{S4}$$

$$\frac{d\theta_{\mathrm{HCO}}}{dt} = r_{\mathrm{f21}} + r_{\mathrm{f22}} + r_{\mathrm{b23}} + r_{\mathrm{f24}} + r_{\mathrm{f25}} + r_{\mathrm{f26}} + r_{\mathrm{b27}} - r_{\mathrm{b21}} - r_{\mathrm{b22}} - r_{\mathrm{f23}} - r_{\mathrm{b24}} - r_{\mathrm{b25}} - r_{\mathrm{b26}} - r_{\mathrm{f27}} \tag{S5}$$

$$\frac{d\theta_{\mathrm{HCOO}}}{dt} = r_{\mathrm{f14}} + r_{\mathrm{b15}} + r_{\mathrm{b22}} - r_{\mathrm{b14}} - r_{\mathrm{f15}} - r_{\mathrm{f22}} \tag{S6}$$

$$\frac{d\theta_{\mathrm{H_2CO_2}}}{dt} = r_{\mathrm{f15}} + r_{\mathrm{b16}} + r_{\mathrm{b17}} - r_{\mathrm{b15}} - r_{\mathrm{f16}} - r_{\mathrm{f17}} \tag{S7}$$

$$\frac{d\theta_{\mathrm{COOH}}}{dt} = r_{\mathrm{f8}} + r_{\mathrm{b9}} + r_{\mathrm{b10}} - r_{\mathrm{b8}} - r_{\mathrm{f9}} - r_{\mathrm{f10}} \tag{S8}$$

$$\frac{d\theta_{\mathrm{CH_2O}}}{dt} = r_{\mathrm{f5}} + r_{\mathrm{f17}} + r_{\mathrm{f18}} + r_{\mathrm{b19}} + r_{\mathrm{f23}} + r_{\mathrm{f26}} + r_{\mathrm{f28}} - r_{\mathrm{b5}} - r_{\mathrm{b17}} - r_{\mathrm{b18}} - r_{\mathrm{f19}} - r_{\mathrm{b23}} - r_{\mathrm{b26}} - r_{\mathrm{b28}} \tag{S9}$$

$$\frac{d\theta_{\mathrm{CH_3O}}}{dt} = r_{\mathrm{f19}} + r_{\mathrm{b20}} + r_{\mathrm{b26}} + r_{\mathrm{b27}} - r_{\mathrm{b19}} - r_{\mathrm{f20}} - r_{\mathrm{f26}} - r_{\mathrm{f27}} \tag{S10}$$

$$\frac{d\theta_{\mathrm{CH_3O_2}}}{dt} = r_{\mathrm{f16}} + r_{\mathrm{b18}} + r_{\mathrm{b28}} - r_{\mathrm{b16}} - r_{\mathrm{f18}} - r_{\mathrm{f28}} \tag{S11}$$

System of Differential Equations for the Site Balances in Chapter 5

$$\frac{d\theta_{\mathrm{CH_3OH{-}H{-}Z}}}{dt} = r_{\mathrm{f1}} + r_{\mathrm{b2}} + r_{\mathrm{b7}} - r_{\mathrm{b1}} - r_{\mathrm{f2}} - r_{\mathrm{f7}} \quad \text{(S12)}$$

$$\frac{d\theta_{\mathrm{H_2O{-}CH_3{-}Z}}}{dt} = r_{\mathrm{f2}} - r_{\mathrm{b2}} - r_{\mathrm{f3}} \quad \text{(S13)}$$

$$\frac{d\theta_{\mathrm{CH_3{-}Z}}}{dt} = r_{\mathrm{f3}} + r_{\mathrm{b4}} - r_{\mathrm{f4}} \quad \text{(S14)}$$

$$\frac{d\theta_{\mathrm{CH_3OH{-}CH_3{-}Z}}}{dt} = r_{\mathrm{f4}} + r_{\mathrm{b5}} - r_{\mathrm{b4}} - r_{\mathrm{f5}} \quad \text{(S15)}$$

$$\frac{d\theta_{\mathrm{CH_3OCH_3{-}H{-}Z}}}{dt} = r_{\mathrm{f5}} + r_{\mathrm{b6}} - r_{\mathrm{b5}} - r_{\mathrm{f6}} \quad \text{(S16)}$$

$$\frac{d\theta_{\mathrm{CH_3OH{-}CH_3OH{-}H{-}Z}}}{dt} = r_{\mathrm{f7}} + r_{\mathrm{b8}} - r_{\mathrm{b7}} - r_{\mathrm{f8}} \quad \text{(S17)}$$

$$\frac{d\theta_{\mathrm{CH_3OCH_3{-}H_2O{-}H{-}Z}}}{dt} = r_{\mathrm{f8}} - r_{\mathrm{b8}} - r_{\mathrm{f9}} \quad \text{(S18)}$$

Bibliography

1. Motagamwala, A.H., M.R. Ball, and J.A. Dumesic, *Microkinetic Analysis and Scaling Relations for Catalyst Design.* Annual Review of Chemical and Biomolecular Engineering, 2018. **9**(1): p. 413-450.
2. Previtali, D., et al., *Methanol synthesis: a distributed production concept based on biogas plants.* Chemical Engineering Transactions, 2018. **65**: p. 409-414.
3. Jiang, X., et al., *Recent Advances in Carbon Dioxide Hydrogenation to Methanol via Heterogeneous Catalysis.* Chemical Reviews, 2020. **120**(15): p. 7984-8034.
4. Park, J., et al., *Trends and Outlook of Computational Chemistry and Microkinetic Modeling for Catalytic Synthesis of Methanol and DME.* Catalysts, 2020. **10**(6).
5. Park, J., et al., *Kinetic modeling for direct synthesis of dimethyl ether from syngas over a hybrid Cu/ZnO/Al2O3/ferrierite catalyst.* Catalysis Today, 2020.
6. Park, J., et al., *Practical Microkinetic Modeling Approach for Methanol Synthesis from Syngas over a Cu-Based Catalyst.* Industrial & Engineering Chemistry Research, 2019. **58**(20): p. 8663-8673.
7. Park, J., et al., *Microkinetic modeling of DME synthesis from methanol over H-zeolite catalyst: Associative vs. dissociative pathways.* Catalysis Today, 2020.
8. Bush, S.F., P. Dyer, and C.A.J. Young, *The experimental and computational determination of complex chemical kinetics mechanisms.* Proceedings of the Royal Society of London. A. Mathematical and Physical Sciences, 1976. **351**(1664): p. 33-53.
9. Hickman, D.A. and L.D. Schmidt, *Steps in CH4 oxidation on Pt and Rh surfaces: High-temperature reactor simulations.* AIChE Journal, 1993. **39**(7): p. 1164-1177.
10. Oh, S.H., et al., *Comparative kinetic studies of CO O2 and CO NO reactions over single crystal and supported rhodium catalysts.* Journal of Catalysis, 1986. **100**(2): p. 360-376.
11. Dumesic, J.A., et al., *The microkinetics of heterogeneous catalysis.* 1993: Wiley-Vch.
12. Raimondeau, S. and D.G. Vlachos, *Recent developments on multiscale, hierarchical modeling of chemical reactors.* Chemical Engineering Journal, 2002. **90**(1): p. 3-23.
13. Salciccioli, M., et al., *A review of multiscale modeling of metal-catalyzed reactions: Mechanism development for complexity and*

emergent behavior. Chemical Engineering Science, 2011. **66**(19): p. 4319-4355.

14. Bronsted, J., *Acid and Basic Catalysis.* Chemical Reviews, 1928. **5**(3): p. 231-338.
15. Evans, M. and M. Polanyi, *Further considerations on the thermodynamics of chemical equilibria and reaction rates.* Transactions of the Faraday Society, 1936. **32**: p. 1333-1360.
16. Shustorovich, E. and H. Sellers, *The UBI-QEP method: A practical theoretical approach to understanding chemistry on transition metal surfaces.* Surface Science Reports, 1998. **31**(1): p. 1-119.
17. Maestri, M. and K. Reuter, *Semiempirical Rate Constants for Complex Chemical Kinetics: First-Principles Assessment and Rational Refinement.* Angewandte Chemie International Edition, 2011. **50**(5): p. 1194-1197.
18. Nørskov, J.K., et al., *Density functional theory in surface chemistry and catalysis.* Proceedings of the National Academy of Sciences, 2011. **108**(3): p. 937.
19. Van Speybroeck, V., et al., *First principle chemical kinetics in zeolites: the methanol-to-olefin process as a case study.* Chemical Society Reviews, 2014. **43**(21): p. 7326-7357.
20. Campbell, C.T., *Future directions and industrial perspectives micro- and macro-kinetics: their relationship in heterogeneous catalysis.* Topics in Catalysis, 1994. **1**(3-4): p. 353-366.
21. Greeley, J. and M. Mavrikakis, *A first-principles study of surface and subsurface H on and in Ni(111): diffusional properties and coverage-dependent behavior.* Surface Science, 2003. **540**(2): p. 215-229.
22. Kresse, G. and J. Furthmüller, *Efficiency of ab-initio total energy calculations for metals and semiconductors using a plane-wave basis set.* Computational Materials Science, 1996. **6**(1): p. 15-50.
23. Williams, M.L., *CRC Handbook of Chemistry and Physics, 76th edition.* Occupational and Environmental Medicine, 1996. **53**(7): p. 504-504.
24. Herrera, C., et al., *Dimethyl ether synthesis via methanol dehydration over Ta-supported catalysts.* Applied Catalysis A: General, 2019. **582**: p. 117088.
25. Ng, K.L., D. Chadwick, and B.A. Toseland, *Kinetics and modelling of dimethyl ether synthesis from synthesis gas.* Chemical Engineering Science, 1999. **54**(15): p. 3587-3592.
26. Peng, X.D., et al., *Single-Step Syngas-to-Dimethyl Ether Processes for Optimal Productivity, Minimal Emissions, and Natural Gas-Derived Syngas.* Industrial & Engineering Chemistry Research, 1999. **38**(11): p. 4381-4388.

27. Klier, K., et al., *Catalytic synthesis of methanol from COH2: IV. The effects of carbon dioxide.* Journal of Catalysis, 1982. **74**(2): p. 343-360.
28. Coteron, A. and A.N. Hayhurst, *Kinetics of the synthesis of methanol from CO + H2 and CO + CO2 + H2 over copper-based amorphous catalysts.* Chemical Engineering Science, 1994. **49**(2): p. 209-221.
29. Chinchen, G.C., et al., *Mechanism of methanol synthesis from CO2/CO/H2 mixtures over copper/zinc oxide/alumina catalysts: use of14C-labelled reactants.* Applied Catalysis, 1987. **30**(2): p. 333-338.
30. Bussche, K.M.V. and G.F. Froment, *A Steady-State Kinetic Model for Methanol Synthesis and the Water Gas Shift Reaction on a Commercial Cu/ZnO/Al2O3Catalyst.* Journal of Catalysis, 1996. **161**(1): p. 1-10.
31. Peter, M., et al., *Detailed kinetic modeling of methanol synthesis over a ternary copper catalyst.* Chemical Engineering Journal, 2012. **203**: p. 480-491.
32. Graaf, G.H., E.J. Stamhuis, and A.A.C.M. Beenackers, *Kinetics of low-pressure methanol synthesis.* Chemical Engineering Science, 1988. **43**(12): p. 3185-3195.
33. Park, N., et al., *Kinetic modeling of methanol synthesis over commercial catalysts based on three-site adsorption.* Fuel Processing Technology, 2014. **125**: p. 139-147.
34. Grabow, L.C. and M. Mavrikakis, *Mechanism of Methanol Synthesis on Cu through CO2 and CO Hydrogenation.* ACS Catalysis, 2011. **1**(4): p. 365-384.
35. Bercic, G. and J. Levec, *Catalytic dehydration of methanol to dimethyl ether. Kinetic investigation and reactor simulation.* Industrial & engineering chemistry research, 1993. **32**(11): p. 2478-2484.
36. Hadipour, A. and M. Sohrabi, *Kinetic parameters and dynamic modeling of a reactor for direct conversion of synthesis gas to dimethyl ether.* Journal of Industrial and Engineering Chemistry, 2007. **13**(4): p. 558-565.
37. Aguayo, A.T., et al., *Kinetic Modeling of Dimethyl Ether Synthesis in a Single Step on a CuO−ZnO−Al2O3/γ-Al2O3 Catalyst.* Industrial & Engineering Chemistry Research, 2007. **46**(17): p. 5522-5530.
38. An, X., et al., *Dimethyl Ether Synthesis from CO2 Hydrogenation on a CuO−ZnO−Al2O3−ZrO2/HZSM-5 Bifunctional Catalyst.* Industrial & Engineering Chemistry Research, 2008. **47**(17): p. 6547-6554.
39. Vakili, R., et al., *Direct dimethyl ether (DME) synthesis through a thermally coupled heat exchanger reactor.* Applied Energy, 2011. **88**(4): p. 1211-1223.
40. Lim, H.-W., et al., *Modeling of the Kinetics for Methanol Synthesis using Cu/ZnO/Al2O3/ZrO2 Catalyst: Influence of Carbon Dioxide during Hydrogenation.* Industrial & Engineering Chemistry Research, 2009. **48**(23): p. 10448-10455.

41. Graaf, G.H., et al., *Chemical equilibria in methanol synthesis.* Chemical Engineering Science, 1986. **41**(11): p. 2883-2890.
42. Smith, J., et al., *Introduction to Chemical Engineering Thermodynamics.* 2017.
43. Fogler, H.S., *Essentials of chemical reaction engineering.* 2011.
44. Fuller, E.N., P.D. Schettler, and J.C. Giddings, *New method for prediction of binary gas-phase diffusion coefficients.* Industrial & Engineering Chemistry, 1966. **58**(5): p. 18-27.
45. Skrzypek, J., M. Lachowska, and H. Moroz, *Kinetics of methanol synthesis over commercial copper/zinc oxide/alumina catalysts.* Chemical Engineering Science, 1991. **46**(11): p. 2809-2813.
46. Seidel, C., et al., *Kinetic modeling of methanol synthesis from renewable resources.* Chemical Engineering Science, 2018. **175**: p. 130-138.
47. Villa, P., et al., *Synthesis of alcohols from carbon oxides and hydrogen. 1. Kinetics of the low-pressure methanol synthesis.* Industrial & engineering chemistry process design and development, 1985. **24**(1): p. 12-19.
48. Graaf, G.H., et al., *Intra-particle diffusion limitations in low-pressure methanol synthesis.* Chemical Engineering Science, 1990. **45**(4): p. 773-783.
49. Baetzold, R.C. and G.A. Somorjai, *Preexponential factors in surface reactions.* Journal of Catalysis, 1976. **45**(1): p. 94-105.
50. Gokhale, A.A., J.A. Dumesic, and M. Mavrikakis, *On the Mechanism of Low-Temperature Water Gas Shift Reaction on Copper.* Journal of the American Chemical Society, 2008. **130**(4): p. 1402-1414.
51. Ovesen, C.V., et al., *A kinetic model of the water gas shift reaction.* Journal of Catalysis, 1992. **134**(2): p. 445-468.
52. Askgaard, T.S., et al., *A Kinetic Model of Methanol Synthesis.* Journal of Catalysis, 1995. **156**(2): p. 229-242.
53. Park, N., et al., *Modeling and analysis of a methanol synthesis process using a mixed reforming reactor: Perspective on methanol production and CO2 utilization.* Fuel, 2014. **129**: p. 163-172.
54. Portha, J.-F., et al., *Kinetics of Methanol Synthesis from Carbon Dioxide Hydrogenation over Copper–Zinc Oxide Catalysts.* Industrial & Engineering Chemistry Research, 2017. **56**(45): p. 13133-13145.
55. Chinchen, G.C., K.C. Waugh, and D.A. Whan, *The activity and state of the copper surface in methanol synthesis catalysts.* Applied Catalysis, 1986. **25**(1): p. 101-107.
56. Ovesen, C.V., et al., *Kinetic Implications of Dynamical Changes in Catalyst Morphology during Methanol Synthesis over Cu/ZnO Catalysts.* Journal of Catalysis, 1997. **168**(2): p. 133-142.

57. Rasmussen, P., et al., *Methanol synthesis on Cu (100) from a binary gas mixture of CO 2 and H 2.* Catalysis Letters, 1994. **26**(3): p. 373-381.
58. Rasmussen, P.B., M. Kazuta, and I. Chorkendorff, *Synthesis of methanol from a mixture of H2 and CO2 on Cu(100).* Surface Science, 1994. **318**(3): p. 267-280.
59. Kresse, G. and J. Furthmüller, *Efficient iterative schemes for ab initio total-energy calculations using a plane-wave basis set.* Physical Review B, 1996. **54**(16): p. 11169-11186.
60. Kresse, G. and J. Hafner, *Ab initio molecular dynamics for liquid metals.* Physical Review B, 1993. **47**(1): p. 558-561.
61. Luo, M.F., G.R. Hu, and M.H. Lee, *Surface structures of atomic hydrogen adsorbed on Cu(111) surface studied by density-functional-theory calculations.* Surface Science, 2007. **601**(6): p. 1461-1466.
62. d'Alnoncourt, R.N., et al., *The influence of strongly reducing conditions on strong metal–support interactions in Cu/ZnO catalysts used for methanol synthesis.* Physical Chemistry Chemical Physics, 2006. **8**(13): p. 1525-1538.
63. Fujita, S.-i., et al., *Preparation of a coprecipitated Cu/ZnO catalyst for the methanol synthesis from CO2 — effects of the calcination and reduction conditions on the catalytic performance.* Applied Catalysis A: General, 2001. **207**(1): p. 121-128.
64. Behrens, M., et al., *The Active Site of Methanol Synthesis over Cu/ZnO/Al<sub>2</sub>O<sub>3</sub> Industrial Catalysts.* Science, 2012. **336**(6083): p. 893.
65. Waugh, K.C., *Methanol Synthesis.* Catalysis Today, 1992. **15**(1): p. 51-75.
66. Hansen, P.L., et al., *Atom-Resolved Imaging of Dynamic Shape Changes in Supported Copper Nanocrystals.* Science, 2002. **295**(5562): p. 2053.
67. Yoshihara, J., et al., *Methanol synthesis and reverse water-gas shift kinetics over clean polycrystalline copper.* Catalysis Letters, 1995. **31**(4): p. 313-324.
68. Ferrin, P. and M. Mavrikakis, *Structure Sensitivity of Methanol Electrooxidation on Transition Metals.* Journal of the American Chemical Society, 2009. **131**(40): p. 14381-14389.
69. Ferrin, P., et al., *Reactivity descriptors for direct methanol fuel cell anode catalysts.* Surface Science, 2008. **602**(21): p. 3424-3431.
70. Agrell, J., et al., *Production of hydrogen from methanol over Cu/ZnO catalysts promoted by ZrO2 and Al2O3.* Journal of Catalysis, 2003. **219**(2): p. 389-403.
71. Okamoto, Y., et al., *Surface characterization of copper (II) oxide-zinc oxide methanol-synthesis catalysts by X-ray photoelectron*

spectroscopy. 1. Precursor and calcined catalysts. The Journal of Physical Chemistry, 1983. **87**(19): p. 3740-3747.

72. Sholl, D. and J.A. Steckel, *Density functional theory: a practical introduction*. 2011: John Wiley & Sons.

73. Graaf, G.H., *The synthesis of methanol in gas-solid and gas-slurry reactors*. 1988, Univ.

74. Caldwell, L., *Gas-solid mass transfer in a spinning catalyst basket reactor.* Applied Catalysis, 1982. **4**(1): p. 13-18.

75. Muhler, M., et al., *Temperature-programmed desorption of H2 as a tool to determine metal surface areas of Cu catalysts.* Catalysis Letters, 1992. **14**(3): p. 241-249.

76. Campbell, C.T. and K.A. Daube, *A surface science investigation of the water-gas shift reaction on Cu(111).* Journal of Catalysis, 1987. **104**(1): p. 109-119.

77. Campbell, C.T., B.E. Koel, and K.A. Daube, *Surface science studies of the water–gas shift reaction on a model Cu(111) catalyst.* Journal of Vacuum Science & Technology A, 1987. **5**(4): p. 810-813.

78. Chinchen, G.C., et al., *Promotion of methanol synthesis and the water-gas shift reactions by adsorbed oxygen on supported copper catalysts.* Journal of the Chemical Society, Faraday Transactions 1: Physical Chemistry in Condensed Phases, 1987. **83**(7): p. 2193-2212.

79. Edwards, J.F. and G.L. Schrader, *Infrared spectroscopy of copper/zinc oxide catalysts for the water-gas shift reaction and methanol synthesis.* The Journal of Physical Chemistry, 1984. **88**(23): p. 5620-5624.

80. van Herwijnen, T. and W.A. de Jong, *Kinetics and mechanism of the CO shift on CuZnO: 1. Kinetics of the forward and reverse CO shift reactions.* Journal of Catalysis, 1980. **63**(1): p. 83-93.

81. van Herwijnen, T., R.T. Guczalski, and W.A. de Jong, *Kinetics and mechanism of the CO shift on CuZnO: II. Kinetics of the decomposition of formic acid.* Journal of Catalysis, 1980. **63**(1): p. 94-101.

82. Fujitani, T., et al., *The kinetics and mechanism of methanol synthesis by hydrogenation of CO2 over a Zn-deposited Cu(111) surface.* Surface Science, 1997. **383**(2): p. 285-298.

83. Fujitani, T., et al., *Scanning Tunneling Microscopy Study of Formate Species Synthesized from CO2 Hydrogenation and Prepared by Adsorption of Formic Acid over Cu(111).* The Journal of Physical Chemistry B, 2000. **104**(6): p. 1235-1240.

84. Hayden, B.E., et al., *An iras study of formic acid and surface formate adsorbed on Cu(110).* Surface Science, 1983. **133**(2): p. 589-604.

85. Sotiropoulos, A., et al., *A structural study of formate on Cu(111).* Surface Science, 2000. **444**(1): p. 52-60.

86. Campbell, C.T., *Finding the Rate-Determining Step in a Mechanism: Comparing DeDonder Relations with the "Degree of Rate Control".* Journal of Catalysis, 2001. **204**(2): p. 520-524.
87. Campbell, C.T., *The Degree of Rate Control: A Powerful Tool for Catalysis Research.* ACS Catalysis, 2017. **7**(4): p. 2770-2779.
88. Cortright, R.D. and J.A. Dumesic, *Kinetics of heterogeneous catalytic reactions: Analysis of reaction schemes*, in *Advances in Catalysis*. 2001, Academic Press. p. 161-264.
89. Tagawab, T., G. Pleizier, and Y. Amenomiya, *Methanol synthesis from CO2+H2 I. characterization of catalysts by TPD.* Applied Catalysis, 1985. **18**(2): p. 285-293.
90. Zhang, L., et al., *Synthesis of Dimethyl Ether via Methanol Dehydration over Combined Al2O3-HZSM-5 Solid Acids.* Chinese Journal of Catalysis, 2010. **31**(8): p. 987-992.
91. Catizzone, E., et al., *Dimethyl ether synthesis via methanol dehydration: Effect of zeolite structure.* Applied Catalysis A: General, 2015. **502**: p. 215-220.
92. Azizi, Z., et al., *Dimethyl ether: A review of technologies and production challenges.* Chemical Engineering and Processing: Process Intensification, 2014. **82**: p. 150-172.
93. Hayer, F., et al., *Characteristics of integrated micro packed bed reactor-heat exchanger configurations in the direct synthesis of dimethyl ether.* Chemical Engineering and Processing: Process Intensification, 2013. **70**: p. 77-85.
94. Tokay, K.C., T. Dogu, and G. Dogu, *Dimethyl ether synthesis over alumina based catalysts.* Chemical Engineering Journal, 2012. **184**: p. 278-285.
95. Fleisch, T.H., A. Basu, and R.A. Sills, *Introduction and advancement of a new clean global fuel: The status of DME developments in China and beyond.* Journal of Natural Gas Science and Engineering, 2012. **9**: p. 94-107.
96. Gądek, M., R. Kubica, and E. Jędrysik, *Production of Methanol and Dimethyl ether from biomass derived syngas – a comparison of the different synthesis pathways by means of flowsheet simulation*, in *Computer Aided Chemical Engineering*, A. Kraslawski and I. Turunen, Editors. 2013, Elsevier. p. 55-60.
97. Zhang, L., et al., *Dehydration of methanol to dimethyl ether over γ-Al2O3 catalyst: Intrinsic kinetics and effectiveness factor.* The Canadian Journal of Chemical Engineering, 2013. **91**(9): p. 1538-1546.
98. Qin, Z.-z., et al., *Experimental and theoretical study of the intrinsic kinetics for dimethyl ether synthesis from CO2 over Cu–Fe–Zr/HZSM-5.* AIChE Journal, 2015. **61**(5): p. 1613-1627.

99. Su, T., et al., *Intrinsic Kinetics of Dimethyl Ether Synthesis from Plasma Activation of CO2 Hydrogenation over Cu–Fe–Ce/HZSM-5.* ChemPhysChem, 2017. **18**(3): p. 299-309.
100. Liu, D., et al., *Catalytic dehydration of methanol to dimethyl ether over modified γ-Al2O3 catalyst.* Fuel, 2011. **90**(5): p. 1738-1742.
101. Yaripour, F., et al., *Catalytic dehydration of methanol to dimethyl ether (DME) over solid-acid catalysts.* Catalysis Communications, 2005. **6**(2): p. 147-152.
102. Boon, J., et al., *Reversible deactivation of γ-alumina by steam in the gas-phase dehydration of methanol to dimethyl ether.* Catalysis Communications, 2019. **119**: p. 22-27.
103. Bercic, G. and J. Levec, *Intrinsic and global reaction rate of methanol dehydration over. gamma.-alumina pellets.* Industrial & engineering chemistry research, 1992. **31**(4): p. 1035-1040.
104. Ali, M.A., B. Brisdon, and W.J. Thomas, *Synthesis, characterization and catalytic activity of ZSM-5 zeolites having variable silicon-to-aluminum ratios.* Applied Catalysis A: General, 2003. **252**(1): p. 149-162.
105. Rownaghi, A.A., et al., *Selective dehydration of methanol to dimethyl ether on ZSM-5 nanocrystals.* Applied Catalysis B: Environmental, 2012. **119-120**: p. 56-61.
106. Chiang, C.-L. and K.-S. Lin, *Preparation and characterization of CuOAl2O3 catalyst for dimethyl ether production via methanol dehydration.* International Journal of Hydrogen Energy, 2017. **42**(37): p. 23526-23538.
107. Bonura, G., et al., *DME production by CO2 hydrogenation: Key factors affecting the behaviour of CuZnZr/ferrierite catalysts.* Catalysis Today, 2017. **281**: p. 337-344.
108. Chen, H.-J., C.-W. Fan, and C.-S. Yu, *Analysis, synthesis, and design of a one-step dimethyl ether production via a thermodynamic approach.* Applied Energy, 2013. **101**: p. 449-456.
109. Hosseini, S., M. Taghizadeh, and A. Eliassi, *Optimization of hydrothermal synthesis of H-ZSM-5 zeolite for dehydration of methanol to dimethyl ether using full factorial design.* Journal of Natural Gas Chemistry, 2012. **21**(3): p. 344-351.
110. Brogaard, R.Y., P.G. Moses, and J.K. Nørskov, *Modeling van der Waals Interactions in Zeolites with Periodic DFT: Physisorption of n-Alkanes in ZSM-22.* Catalysis Letters, 2012. **142**(9): p. 1057-1060.
111. Moses, P.G. and J.K. Nørskov, *Methanol to Dimethyl Ether over ZSM-22: A Periodic Density Functional Theory Study.* ACS Catalysis, 2013. **3**(4): p. 735-745.
112. Wang, C.-M., et al., *Methanol to Olefin Conversion on HSAPO-34 Zeolite from Periodic Density Functional Theory Calculations: A*

Complete Cycle of Side Chain Hydrocarbon Pool Mechanism. The Journal of Physical Chemistry C, 2009. **113**(11): p. 4584-4591.

113. Kachurovskaya, N.A., et al., *Cluster Model DFT Study of the Intermediates of Benzene to Phenol Oxidation by N2O on FeZSM-5 Zeolites.* Catalysis Letters, 2003. **86**(1): p. 25-31.
114. Ryder, J.A., A.K. Chakraborty, and A.T. Bell, *Density Functional Theory Study of Proton Mobility in Zeolites: Proton Migration and Hydrogen Exchange in ZSM-5.* The Journal of Physical Chemistry B, 2000. **104**(30): p. 6998-7011.
115. Blaszkowski, S.R. and R.A. van Santen, *Theoretical Study of the Mechanism of Surface Methoxy and Dimethyl Ether Formation from Methanol Catalyzed by Zeolitic Protons.* The Journal of Physical Chemistry B, 1997. **101**(13): p. 2292-2305.
116. Fujino, T., et al., *FT-IR and Quantum Chemical Studies of the Interaction between Dimethyl Ether and HZSM-5 Zeolite.* The Journal of Physical Chemistry, 1996. **100**(28): p. 11649-11653.
117. Van Speybroeck, V., et al., *First Principle Kinetic Studies of Zeolite-Catalyzed Methylation Reactions.* Journal of the American Chemical Society, 2011. **133**(4): p. 888-899.
118. Zhao, Y. and D.G. Truhlar, *Benchmark Data for Interactions in Zeolite Model Complexes and Their Use for Assessment and Validation of Electronic Structure Methods.* The Journal of Physical Chemistry C, 2008. **112**(17): p. 6860-6868.
119. Figueras, F., et al., *Dehydration of methanol and tert-butyl alcohol on silica-alumina.* Transactions of the Faraday Society, 1971. **67**: p. 1155-1163.
120. Kubelková, L., J. Nováková, and K. Nedomová, *Reactivity of surface species on zeolites in methanol conversion.* Journal of Catalysis, 1990. **124**(2): p. 441-450.
121. Blaszkowski, S.R. and R.A. van Santen, *The Mechanism of Dimethyl Ether Formation from Methanol Catalyzed by Zeolitic Protons.* Journal of the American Chemical Society, 1996. **118**(21): p. 5152-5153.
122. Jones, A.J. and E. Iglesia, *Kinetic, spectroscopic, and theoretical assessment of associative and dissociative methanol dehydration routes in zeolites.* Angewandte Chemie, 2014. **126**(45): p. 12373-12377.
123. Gao, X.-Y., et al., *DME synthesis from methanol over hydrated γ-Al2O3(110) surface in slurry bed using continuum and atomistic models.* Journal of Theoretical and Computational Chemistry, 2017. **16**(04): p. 1750029.
124. Tavan, Y., et al., *From laboratory experiments to simulation studies of methanol dehydration to produce dimethyl ether—Part I: Reaction kinetic study.* Chemical Engineering and Processing: Process Intensification, 2013. **73**: p. 144-150.

125. Lu, W.-Z., L.-H. Teng, and W.-D. Xiao, *Simulation and experiment study of dimethyl ether synthesis from syngas in a fluidized-bed reactor.* Chemical Engineering Science, 2004. **59**(22): p. 5455-5464.
126. Mollavali, M., et al., *Intrinsic Kinetics Study of Dimethyl Ether Synthesis from Methanol on γ-Al2O3 Catalysts.* Industrial & Engineering Chemistry Research, 2008. **47**(9): p. 3265-3273.
127. Hassanpour, S., F. Yaripour, and M. Taghizadeh, *Performance of modified H-ZSM-5 zeolite for dehydration of methanol to dimethyl ether.* Fuel Processing Technology, 2010. **91**(10): p. 1212-1221.
128. Tuma, C. and J. Sauer, *Treating dispersion effects in extended systems by hybrid MP2: DFT calculations—protonation of isobutene in zeolite ferrierite.* Physical Chemistry Chemical Physics, 2006. **8**(34): p. 3955-3965.
129. Wesolowski, T.A., et al., *Comparative Study of Benzene···X (X = O2, N2, CO) Complexes Using Density Functional Theory: The Importance of an Accurate Exchange−Correlation Energy Density at High Reduced Density Gradients.* The Journal of Physical Chemistry A, 1997. **101**(42): p. 7818-7825.
130. Hytha, M., et al., *Thermodynamics of Catalytic Formation of Dimethyl Ether from Methanol in Acidic Zeolites.* Chemistry – A European Journal, 2001. **7**(12): p. 2521-2527.
131. John, M., et al., *First-Principles Kinetic Study on the Effect of the Zeolite Framework on 1-Butanol Dehydration.* ACS Catalysis, 2016. **6**(7): p. 4081-4094.
132. Nachtigall, P., et al., *Computational and FTIR spectroscopic studies on carbon monoxide and dinitrogen adsorption on a high-silica H-FER zeolite.* Physical Chemistry Chemical Physics, 2009. **11**(5): p. 791-802.
133. Nieminen, V., et al., *Stabilities of C3–C5 alkoxide species inside H-FER zeolite: a hybrid QM/MM study.* Journal of Catalysis, 2005. **231**(2): p. 393-404.
134. Plessow, P.N. and F. Studt, *Unraveling the Mechanism of the Initiation Reaction of the Methanol to Olefins Process Using ab Initio and DFT Calculations.* ACS Catalysis, 2017. **7**(11): p. 7987-7994.
135. Rozanska, X., et al., *A Periodic DFT Study of Isobutene Chemisorption in Proton-Exchanged Zeolites: Dependence of Reactivity on the Zeolite Framework Structure.* The Journal of Physical Chemistry B, 2003. **107**(6): p. 1309-1315.
136. Van Santen, R., *Quantum-chemistry of zeolite acidity.* Catalysis today, 1997. **38**(3): p. 377-390.
137. Blaszkowski, S., et al., *Density functional theory calculations of the transition states for hydrogen exchange and dehydrogenation of methane by a broensted zeolitic proton.* The Journal of Physical Chemistry, 1994. **98**(49): p. 12938-12944.

138. Blaszkowski, S.R., M.A.C. Nascimento, and R.A. van Santen, *Activation of C−H and C−C Bonds by an Acidic Zeolite: A Density Functional Study.* The Journal of Physical Chemistry, 1996. **100**(9): p. 3463-3472.
139. Frash, M.V. and R.A. van Santen, *Quantum-chemical modeling of the hydrocarbon transformations in acid zeolite catalysts.* Topics in Catalysis, 1999. **9**(3): p. 191-205.
140. Zheng, X. and P. Blowers, *An ab initio study of ethane conversion reactions on zeolites using the complete basis set composite energy method.* Journal of Molecular Catalysis A: Chemical, 2005. **229**(1): p. 77-85.
141. Frisch, M., et al., *309 Barone, V.; Petersson, G.; Nakatsuji, H., Gaussian 16.* Revision A, 2016. **3**: p. 310.
142. Krishnan, R., et al., *Self-consistent molecular orbital methods. XX. A basis set for correlated wave functions.* The Journal of Chemical Physics, 1980. **72**(1): p. 650-654.
143. McLean, A.D. and G.S. Chandler, *Contracted Gaussian basis sets for molecular calculations. I. Second row atoms, Z=11–18.* The Journal of Chemical Physics, 1980. **72**(10): p. 5639-5648.
144. Mitchell, M., *An introduction to genetic algorithms*. 1998: MIT press.
145. Gale, J.D., C.R.A. Catlow, and J.R. Carruthers, *An ab initio study of methanol adsorption in zeolites.* Chemical Physics Letters, 1993. **216**(1): p. 155-161.
146. Haase, F. and J. Sauer, *Interaction of methanol with Broensted acid sites of zeolite catalysts: an ab initio study.* Journal of the American Chemical Society, 1995. **117**(13): p. 3780-3789.
147. Hunger, M. and T. Horvath, *Adsorption of Methanol on Brønsted Acid Sites in Zeolite H-ZSM-5 Investigated by Multinuclear Solid-State NMR Spectroscopy.* Journal of the American Chemical Society, 1996. **118**(49): p. 12302-12308.
148. Shah, R., J.D. Gale, and M.C. Payne, *Methanol Adsorption in ZeolitesA First-Principles Study.* The Journal of Physical Chemistry, 1996. **100**(28): p. 11688-11697.
149. Shah, R., et al., *Understanding the Catalytic Behavior of Zeolites: A First-Principles Study of the Adsorption of Methanol.* Science, 1996. **271**(5254): p. 1395.
150. Dudukovic, M.P., *Frontiers in Reactor Engineering.* Science, 2009. **325**(5941): p. 698.
151. Maestri, M., *Escaping the trap of complication and complexity in multiscale microkinetic modelling of heterogeneous catalytic processes.* Chemical Communications, 2017. **53**(74): p. 10244-10254.
152. Bracconi, M. and M. Maestri, *Training set design for machine learning techniques applied to the approximation of computationally intensive*

first-principles kinetic models. Chemical Engineering Journal, 2020. **400**: p. 125469.

153. Bruix, A., et al., *First-principles-based multiscale modelling of heterogeneous catalysis.* Nature Catalysis, 2019. **2**(8): p. 659-670.

154. Matera, S., et al., *Progress in Accurate Chemical Kinetic Modeling, Simulations, and Parameter Estimation for Heterogeneous Catalysis.* ACS Catalysis, 2019. **9**(8): p. 6624-6647.

155. Partopour, B. and A.G. Dixon, *Computationally efficient incorporation of microkinetics into resolved-particle CFD simulations of fixed-bed reactors.* Computers & Chemical Engineering, 2016. **88**: p. 126-134.

156. Partopour, B. and A.G. Dixon, *Reduced Microkinetics Model for Computational Fluid Dynamics (CFD) Simulation of the Fixed-Bed Partial Oxidation of Ethylene.* Industrial & Engineering Chemistry Research, 2016. **55**(27): p. 7296-7306.

157. Partopour, B., R.C. Paffenroth, and A.G. Dixon, *Random Forests for mapping and analysis of microkinetics models.* Computers & Chemical Engineering, 2018. **115**: p. 286-294.

158. Sabbe, M.K., M.-F. Reyniers, and K. Reuter, *First-principles kinetic modeling in heterogeneous catalysis: an industrial perspective on best-practice, gaps and needs.* Catalysis Science & Technology, 2012. **2**(10): p. 2010-2024.

159. Greeley, J., J.K. Nørskov, and M. Mavrikakis, *ELECTRONIC STRUCTURE AND CATALYSIS ON METAL SURFACES.* Annual Review of Physical Chemistry, 2002. **53**(1): p. 319-348.

160. Hammer, B., L.B. Hansen, and J.K. Nørskov, *Improved adsorption energetics within density-functional theory using revised Perdew-Burke-Ernzerhof functionals.* Physical Review B, 1999. **59**(11): p. 7413-7421.

161. Koryabkina, N.A., et al., *Determination of kinetic parameters for the water–gas shift reaction on copper catalysts under realistic conditions for fuel cell applications.* Journal of Catalysis, 2003. **217**(1): p. 233-239.

162. Geurts, P., D. Ernst, and L. Wehenkel, *Extremely randomized trees.* Machine Learning, 2006. **63**(1): p. 3-42.

163. Hastie, T., R. Tibshirani, and J. Friedman, *The elements of statistical learning: data mining, inference, and prediction*. 2009: Springer Science & Business Media.

Abstract in Korean (국문초록)

최근에 계속해서 환경 오염 문제가 대두됨에 따라 이산화탄소를 줄이는 것에 대한 관심이 커지고 있다. 이에 따라 다양한 분야의 많은 연구자들과 산업에서도 이산화탄소의 배출을 줄이고자 노력하고 있다. 특히 화학공학자들은 온실 가스를 사용하여 유용한 케미컬을 생산할 수 있는 탄소 활용 반응 공정들을 개발해왔다. 이러한 반응들에 대해 이미 상용 공정들이 개발되어 있지만 이 반응들의 반응 메커니즘에 대해서는 여전히 논쟁이 진행 중이다. 컴퓨터 계산 성능의 발전과 더불어 반응 메커니즘 탐색에 대한 연구는 새로운 국면을 맞아 더욱 활발해지고 있다. 상당한 계산량을 요구하는 계산 화학은 반응 메커니즘 분석에 엄청난 도움이 되고 있다. 더욱이 키네틱 관점에서 메커니즘을 분석할 수 있는 마이크로키네틱 스터디는 계산 화학의 발전과 더불어 시너지 효과를 낼 수 있다. 화학 공학에서 전통적인 키네틱 모델은 주로 공정 개발에 사용되는 반면, 마이크로키네틱 모델은 이러한 장점에 더하여 근본적인 분석이 가능하다. 이러한 이유로 널리 알려진 반응들에 대해서도 마이크로키네틱을 통한 메커니즘 분석은 활발하게 이루어지고 있다. 본 학위 논문에서는 기존의 몇 가지 결점들을 개선할 수 있는 실용적인 마이크로키네틱 모델링 전략을 제안하였다. 메탄올 및 디메틸에테르(DME) 합성 관련 반응들에 대해서 밀도범함수 이론(DFT) 및 이 결과를 이용한 마이크로키네틱 모델링을 수행하고, 이를 통한 반응 메커니즘 분석 및 여러 케이스

스터디를 진행하였다. 파라미터 추정 기법을 이용하여 예측값과 실험값의 차이를 최소화 하는 방향으로 Pre-exponential 인자를 실험 데이터에 피팅하였다. 이러한 마이크로키네틱스에의 실용적인 모델링 접근법은 모델의 계산효율과 신뢰성을 개선할 수 있었다.

논문의 첫 번째 부분으로 Lumped 키네틱 모델과 마이크로키네틱 모델의 차이를 강조하기 위해, Cu/ZnO/Al_2O_3/ferrierite (CZA/FER) 하이브리드 촉매 하에서 합성가스로부터 디메틸에테르로의 직접 전환 반응에 대해 Lumped 키네틱 모델을 개발하였다. 키네틱 파라미터는 하이브리드 촉매에서의 실험 값에 피팅되도록 추정하였고, 이는 CZA 및 FER 촉매 각각에서 보고된 선행 연구에서의 값과 비교하였다. 하이브리드 촉매에서의 높은 활성화 에너지는 메탄올 합성 단계가 메탄올 탈수 단계보다 전체적인 반응 속도를 조절하는 인자라는 것을 보여주었다. 또한 개발된 키네틱 모델을 통해 200 ~ 220 ℃의 온도에서 운전하는 것이 효율적임을 알 수 있었으며, 최적의 운전 압력 및 공간 속도를 제시하였다.

두 번째 부분에서는 구리 기반 촉매 하에서 합성가스로부터 메탄올을 합성하는 반응에 대해서 마이크로키네틱 모델링을 하기 위한 실용적인 방법에 대해 묘사하였다. 일산화탄소 및 이산화탄소의 수소화 반응, Water-gas shift 반응에 대해 28 개의 단일단계반응을 고려하였다. DFT 와 반경험적인 방법론인 Unity bond index-quadratic exponential (UBI-QEP) 기법을 조합하여 흡착열 및 활성화 에너지를 도출하였다. DFT 계산을 통해 포름산염(HCOO**)이

이좌배위자(Bidentate) 형태로 흡착되는 것을 확인하였으며, UBI-QEP 계산을 위한 기상과 흡착된 중간 생성물들의 흡착에너지 및 엔탈피를 제공하였다. Pre-exponential 인자의 경우에는 전이상태이론의 Order-of-magnitude 에 기반하여 초기 값을 설정하고, 실험 데이터에 피팅하였다. 덕분에 이를 위한 진동 주파수 및 분배 함수를 계산하지 않아 계산 로드를 줄일 수 있었다. 반응기 모델에서는 마이크로키네틱 모델의 경직성을 완화하기 위해 부분평형비를 계산하였다. 상대적으로 빠른 단일단계반응을 기반으로 우세한 반응 경로를 제안하였으며, Degree of rate control 계산을 통해 H_3CO*와 H*의 표면 반응이 속도 결정 단계임을 제안하였다. 또한 운전 온도, 압력 및 Feed 의 H_2 분율이 메탄올 합성 속도에 미치는 영향을 알아보기 위해 개발된 모델을 사용하였다.

세 번째 부분에서는 계산 화학 및 마이크로키네틱 모델링을 통해, H-zeolite 촉매 하에서 메탄올 탈수 반응에 의한 디메틸에테르 합성에 대해서 반응 경로를 분석하였다. 반응 메커니즘으로는 Associative 및 Dissociative 경로에 대해서 9 개의 단일단계반응을 포함하였다. 이러한 반응 시스템에서는 분산력의 영향이 있으므로 2 차 묄러-플레셋 섭동 이론(MP2)에 기반하여 반응종들의 구조를 최적화하였다. 또한, 반응의 전이 상태를 도출하였으며 이와 최적 분자 구조의 에너지 및 활성화 에너지를 계산하였다. 이 결과에 기반하여 마이크로키네틱 모델을 개발하였고, Pre-exponential 인자는

마찬가지로 실험 데이터에 피팅하였다. 이러한 방법론은 개발된 마이크로키네틱 모델의 신뢰성을 강화하였다. 단일단계반응들의 상대적인 반응 속도를 비교하여 Dissociative 경로가 우세하게 작용함을 알 수 있었으며, 이 경로의 DME 생성 반응(CH_3OH-CH_3-Z → CH_3OCH_3-H-Z)을 속도 결정 단계로 제안하였다. 마찬가지로 이 모델을 통해 온도가 촉매 표면의 농도 분포에 미치는 영향을 분석하였다.

마지막으로, Water-gas shift 반응에 대한 마이크로키네틱 모델에 대하여 기계학습 기반의 대체 모델을 제시하였다. 마이크로키네틱 대체 모델은 마이크로키네틱스와 전산유체역학이나 공정 시뮬레이션과 같은 더 높은 차원의 반응 공학 모듈을 이어주는 다리 역할을 할 수 있다. ExtraTrees 알고리즘과 인공신경망을 이용하여 개발된 마이크로키네틱 모델로부터 얻은 데이터셋을 회귀하였다. 보간 기계학습 기법 중에서 인공신경망은 회귀 분석에서 높은 성능을 낼 수 있는 것으로 잘 알려져 있고, ExtraTrees 알고리즘은 특성 중요도를 계산 할 수 있다. 인공신경망 기반의 대체 모델은 평균 오차율 0.01%로 좋은 성능을 보여주었다. ExtraTrees 일고리즘은 특성 중요도를 측정할 수 있어, Water-gas shift 반응에서 중요한 단일단계반응과 중요한 촉매 표면의 중간생성물을 찾아낼 수 있었다.

주요어: 마이크로키네틱 모델링; 계산 화학; 파라미터 추정; 반응 메커니즘; C1 화학; 기계학습

학 번: 2015-22831